

Copyright
by
Audrey Hucks Sawyer
2011

**The Thesis Committee for Audrey Hucks Sawyer
Certifies that this is the approved version of the following thesis:**

**COMPLEXITY IN RIVER-GROUNDWATER EXCHANGE DUE TO
PERMEABILITY HETEROGENEITY, IN-STREAM FLOW
OBSTACLES, AND RIVER STAGE FLUCTUATIONS**

Committee:

M. Bayani Cardenas, Supervisor

Ginny Catania

Ben Hodges

David Mohrig

Danny Reible

**COMPLEXITY IN RIVER-GROUNDWATER EXCHANGE DUE TO
PERMEABILITY HETEROGENEITY, IN-STREAM FLOW
OBSTACLES, AND RIVER STAGE FLUCTUATIONS**

by

Audrey Hucks Sawyer, B.S.; M.S.

Dissertation

Presented to the Faculty of the Graduate School of

The University of Texas at Austin

in Partial Fulfillment

of the Requirements

for the Degree of

Doctor of Philosophy

The University of Texas at Austin

May 2011

Acknowledgements

I thank my advisor, committee members, and research group for their insights and suggestions over the course of my thesis research. In particular, Jim Buttles shared his knowledge and experience in flume studies. Many friends and family assisted me in flume and field experiments, including Wade Chaney, Kuldeep Chaudhary, Anne Dunckel, Josh Garber, Katy Gerech, Jesus Gomez Velez, Kelly Hereid, Frank Hucks, Melanie Laughlin, Michael Markowski, John Nowinski, Lani Rosenthal, Derek Sawyer, Travis Swanson, and Yao You. My husband, parents, and grandparents supported me with encouraging words and good humor when I needed it. I thank Kevin Anderson and Austin Water Utility for providing access to Hornsby Bend, as well as Bob Parmenter and Valles Caldera National Preserve for providing access to San Antonio Creek. Vincent Tidwell and Gary Kocurek provided data for cross-bedded permeability fields. This research was supported by NSF Grant EAR-0836540, the ACS Petroleum Research Fund, an AGU Horton Research Grant, and student research grants from AAPG and GSA.

Abstract

COMPLEXITY IN RIVER-GROUNDWATER EXCHANGE DUE TO PERMEABILITY HETEROGENEITY, IN-STREAM FLOW OBSTACLES, AND RIVER STAGE FLUCTUATIONS

Audrey Hucks Sawyer, Ph.D.

The University of Texas at Austin, 2011

Supervisor: M. Bayani Cardenas

River-groundwater exchange (hyporheic exchange) influences temperature, water chemistry, and ecology within rivers and alluvial aquifers. Rates and patterns of hyporheic exchange depend on riverbed permeability, pressure gradients created by current-obstacle interactions, and river stage fluctuations. I demonstrate the response of hyporheic exchange to three examples of these driving forces: fine-scale permeability structure in cross-bedded sediment, current interactions with large woody debris (LWD), and anthropogenic river stage fluctuations downstream of dams.

Using numerical simulations, I show that cross-bedded permeability structure increases hyporheic path lengths and modifies solute residence times in bedforms. The tails of residence time distributions conform to a power law in both cross-bedded and internally homogeneous riverbed sediment. Current-bedform interactions are responsible for the decade-scale tails, rather than permeability heterogeneity.

Like bedforms, wood debris interacts with currents and drives hyporheic exchange. Laboratory flume experiments and numerical simulations demonstrate that the amplitude of the pressure wave (and thus hyporheic exchange) due to a channel-spanning log increases with channel Froude number and blockage ratio (log diameter : flow depth). Upstream from LWD, downwelling water transports the river's diel thermal signal deep into the sediment. Downstream, upwelling water forms a wedge of buffered temperatures. Hyporheic exchange associated with LWD does not significantly impact diel surface water temperatures. I tested these fluid and heat flow relationships in a second-order stream in Valles Caldera National Preserve (NM). Log additions created alternating zones of upwelling and downwelling in a reach that was previously losing throughout. By clearing LWD from channels, humans have reduced hydrologic connectivity at the meter-scale and contributed to degradation of benthic and hyporheic habitats.

Dams also significantly alter hydrologic connectivity in modern rivers. Continuous water table measurements show that 15 km downstream of the Longhorn dam (Austin, Texas), river stage fluctuations of almost 1 m induce a large, unsteady hyporheic exchange zone within the bank. Dam-induced hyporheic exchange may impact thermal and geochemical budgets for regulated rivers. Together, these three case studies broaden our understanding of complex drivers of hyporheic exchange in small, natural streams as well as large, regulated rivers.

Table of Contents

List of Tables	xi
List of Figures	xii
Chapter 1: <i>Introduction</i>	1
1.1. Motivation.....	1
1.2. Thesis Organization	2
Chapter 2: Hyporheic Flow and Residence Time Distributions in Heterogeneous Cross-Bedded Sediment.....	6
2.1. Abstract.....	6
2.2. Introduction.....	6
2.3. Methods.....	9
2.3.1. Permeability Datasets.....	9
2.3.2. Geostatistical Analysis.....	10
2.3.3. Estimating an Equivalent Homogeneous Permeability Tensor ..11	
2.3.4. Hyporheic Flow and Solute Transport Simulations.....	11
2.4. Massillon Sandstone: A Cross-bedded Sand Case Study	14
2.4.1. Lithology.....	14
2.4.2. Geostatistical Properties.....	15
2.4.3. Hyporheic Flow and Transport in Heterogeneous Medium	15
2.4.4. Hyporheic Flow and Transport in Homogeneous Medium	16
2.5. Brazos River Sediment: A Climbing Ripple Case Study.....	16
2.5.1. Lithologic Description	16
2.5.2. Geostatistical Properties.....	17
2.5.3. Hyporheic Flow and Transport in Heterogeneous Medium	17
2.5.4. Hyporheic Flow and Transport in Homogeneous Medium	18
2.6. Permeability Anisotropy Sensitivity Study.....	18
2.7. Discussion.....	20
2.8. Conclusions.....	24
2.9. Notation.....	25

Chapter 3: River-groundwater exchange due to large woody debris.....	34
3.1. Abstract.....	34
3.2. Introduction.....	34
3.3. Methods.....	36
3.3.1. Flume experiments.....	36
3.3.2. Numerical modeling.....	37
3.3.3. Sensitivity study.....	41
3.4. Results.....	42
3.4.1. Two case studies of hyporheic exchange near a channel-spanning log	42
3.4.2. Influence of scour topography	44
3.4.3. A semi-empirical model for head profile along the bed	45
3.4.4. Hyporheic exchange from LWD geometry and flow parameters.....	48
3.5. Discussion.....	48
3.6. Conclusions.....	50
Chapter 4: Thermal dynamics in hyporheic zones formed by large woody debris.....	58
4.1. Abstract.....	58
4.2. Introduction.....	59
4.3. Methods.....	61
4.3.1. Flume experiments.....	61
4.3.2. Numerical modeling.....	62
4.4. Results.....	65
4.4.1. Observed temperature dynamics.....	65
4.4.2. Modeled temperature dynamics and inferred heat exchange contributions	66
4.4.3. Role of permeability in hyporheic temperature dynamics	67
4.5. Discussion.....	68
4.6. Conclusions.....	70
Chapter 5: Effect of large woody debris additions on hyporheic exchange in a losing stream.....	80
5.1. Abstract.....	80

5.2. Introduction.....	80
5.3. Study Site	82
5.4. Methods.....	83
5.4.1. Experimental log configurations.....	83
5.4.2. Local hyporheic exchange measurements	84
5.4.4. Reach-scale transient storage experiments and simulations	86
5.5. Results.....	89
5.5.1. Local hyporheic exchange and streambed temperatures	89
5.5.2. Reach-scale transient storage.....	90
5.6. Comparison of local hyporheic exchange with reach-scale transient storage	91
5.7. Discussion.....	92
5.8. Conclusions.....	94
Chapter 6: Impact of dam operations on hyporheic exchange in the riparian zone of a regulated river	101
6.1. Abstract.....	101
6.2. Introduction.....	101
6.3. Study site.....	103
6.4. Methods.....	104
6.4.1. Monitoring	104
6.4.2. Aquifer characterization.....	105
6.4.3. Estimation of volumetric flow rate	106
6.4.4. Estimation of hyporheic zone lateral extent.....	107
6.5. Results.....	108
6.6. Discussion.....	110
6.6.1. Hyporheic Response to Dam Operations	110
6.6.2. Chemical and Thermal Implications.....	112
6.7. Conclusions and Recommendations	114
Chapter 7: Summary	122
7.1. Synthesis	122
7.2. Key findings and future work	123

Appendices.....	125
Appendix A1: Scaling analysis.....	125
Appendix A2: Manual for recirculating flume	126
A2.1. Flume-o-matic panel	126
A2.2. Navigating the software	127
A2.3. Modes 1 and 2.....	129
A2.4. Manual and automatic operation.....	129
A2.5. Viewing and Saving Data	133
A2.6. Alarms.....	134
A2.7. Example Procedures.....	135
A2.8. Maintenance	137
A2.9. Trouble-shooting.....	137
References.....	139

List of Tables

Table 2.1: Numerical simulation parameters	27
Table 2.2: Semivariogram model properties.....	27
Table 2.3: Evaluation of external versus internal forcing mechanisms	27
Table 4.1: Parameters for flume experiments	71
Table 5.1: Hydraulic and thermal parameters.....	95
Table 5.2: Hydraulic conductivity estimates	95
Table 5.3: Transient storage parameters	95
Table 6.1: Conceptual model of impact of dam operations	115

List of Figures

Figure 1.1: Conceptual model of hyporheic exchange	5
Figure 2.1: Permeability datasets	28
Figure 2.2: Simulated hyporheic exchange.....	29
Figure 2.3: Breakthrough curves.....	29
Figure 2.4: Experimental and model semivariograms	30
Figure 2.5: Simulated hyporheic exchange.....	30
Figure 2.6: Breakthrough curves.....	31
Figure 2.7: Hyporheic zones	31
Figure 2.8: Hyporheic metrics	32
Figure 2.9: Breakthrough curves for homogeneous anisotropic sediment	32
Figure 2.10: Concentration-depth profiles	33
Figure 3.1: Flume.....	52
Figure 3.2: Simulated surface water and pore water flow	52
Figure 3.3: Hyporheic exchange fills entire flume	53
Figure 3.4: Tracer experiments	53
Figure 3.5: Modeled hyporheic exchange and conservative solute transport.....	54
Figure 3.6: Measured head.....	55
Figure 3.7: Scaling relationships.....	56
Figure 3.8: Scaling relationships for pressure along bed.....	57
Figure 3.9: Dimensionless mean hyporheic flux	57
Figure 4.1: Flume.....	72
Figure 4.2: Channel-view of flume.....	72
Figure 4.3: Boundary conditions	73

Figure 4.4: Amplitude and phase response of diel temperatures	74
Figure 4.5: Examples of temperature signals.....	75
Figure 4.6: Numerically simulated amplitude and phase response.....	76
Figure 4.7: Head distribution	77
Figure 4.8: Conductive, advective, and total heat fluxes	78
Figure 4.9: Numerically simulated amplitude of diel temperatures	79
Figure 5.1: Location of experimental reach	96
Figure 5.2: Photographs of focus sub-reach	96
Figure 5.3: Vertical specific discharge estimates	97
Figure 5.4: Cross-sections of diel pore water temperature amplitudes.....	97
Figure 5.5: Time-series of diel temperatures	98
Figure 5.6: Simulated diel pore water temperature amplitudes	99
Figure 5.7: Specific conductivity time series.....	100
Figure 6.1: Location of study site	116
Figure 6.2: Map of Hornsby Bend piezometer transect.....	116
Figure 6.3: Continuous USGS stream gage record.....	117
Figure 6.4: Water table elevation profiles.....	118
Figure 6.5: River stage, temperature, and specific conductivity.....	118
Figure 6.6: Temperature time series	119
Figure 6.7: Specific conductivity time series.....	119
Figure 6.8: Grain size distributions.....	120
Figure 6.9: Volumetric flow rate between the river and riparian aquifer	120
Figure 6.10: Conceptual model.....	121
Figure A2.1: Flume-o-matic panel and power controls	126
Figure A2.2: Control panel settings	127

Figure A2.3: The Overview page.....	128
Figure A2.4: Schedule page in Mode 2	131
Figure A2.5: Schedule page in Mode 1	132
Figure A2.6: Schedule page.....	132
Figure A2.7: Create new log files.....	134
Figure A2.8: View of Controls Page 1 after alarm.....	135
Figure A2.9: Location of drainage valves.....	136

Chapter 1: Introduction

1.1. MOTIVATION

The bed and banks of rivers form an important interface between surface water and groundwater where turbulent and porous flows meet. Fluid exchange across the riverbed interface transports heat, contaminants, and biologically significant solutes such as nutrients, oxygen, and dissolved organic carbon between aquatic and terrestrial systems [Findlay, 1995]. At the landscape scale, groundwater discharge and recharge along rivers depends on regional water table gradients [Tóth, 1963; Winter, 1999]. Nested within larger patterns of discharge and recharge are smaller patterns of river-groundwater interaction (hyporheic exchange), where river water downwells into the bed, travels along short flow paths, and returns to the channel [Stanford and Ward, 1993]. Hyporheic exchange exposes river water to microbial communities within the sediment that transform river water chemistry. In some cases, hyporheic exchange can also impact the heat budgets of rivers [Arrigoni et al., 2008]. Within the riverbed, hyporheic exchange dictates patterns of pore water chemistry and temperature that regulate habitat quality for macroinvertebrates and fish embryos [Brunke and Gonser, 1997].

While numerous mechanisms drive hyporheic exchange, these mechanisms can be summarized under five categories. Consider a representative cross-sectional element of riverbed sediment (Figure 1.1). From conservation of mass:

$$\frac{1}{\rho} \frac{\partial \rho n A}{\partial t} = -\frac{\partial A q_x}{\partial x} - Q_z + S, \quad (1.1)$$

where ρ is fluid density, n is sediment porosity, A is cross-sectional area of sediment available for hyporheic exchange, q_x is longitudinal volumetric flow rate per unit area, and Q_z is the volumetric hyporheic exchange rate across the bed per length of stream (the

parameter of interest). Invoking Darcy's law for q_x and the definition of specific storage (S_s), Equation 1.1 in terms of hydraulic head (h) is:

$$Q_z = -AS_s \frac{\partial h}{\partial t} - KA \frac{\partial^2 h}{\partial x^2} - A \frac{\partial K}{\partial x} \frac{\partial h}{\partial x} - K \frac{\partial A}{\partial x} \frac{\partial h}{\partial x} + SA, \quad (1.2)$$

where K is hydraulic conductivity. Equation 1.2 assumes a constant, uniform fluid density, saturated sediment, steady area available for exchange, and no lateral exchange perpendicular to the channel. Five terms contribute to hyporheic flow (Q_z). The first term represents temporal change in head. Fluctuations in river stage impact head and drive hyporheic flow. The second term represents spatial variation in hydraulic head gradient. The interaction of currents with riverbed morphology and in-stream flow obstacles produce undulations in hydraulic head that drive hyporheic flow. The third term represents spatial variation in hydraulic conductivity, which ranges by orders of magnitude over many length scales in riverbed sediment. The fourth term represents longitudinal change in the cross-sectional area of sediment available for exchange. Variations in depth to bedrock or alluvial valley width drive exchange. The fifth term represents a fluid source. Examples of fluid sources include plant water uptake and streambed loading due to changing river stage. In this thesis, I explore the impacts of the first, second, and third terms on hyporheic exchange.

1.2. THESIS ORGANIZATION

Each chapter has been prepared or submitted for journal publication and has its own introduction, methods, results, discussion, and references. Here, I present a general description of thesis chapters and highlight important results.

Chapter 2 examines the impact of fine-scale permeability structure on hyporheic exchange within bedforms. The permeability structure of cross-bedded sediment can

increase the depth and length-scales of hyporheic exchange and the proportion of short or long residence times. Hyporheic residence times are particularly sensitive to the permeability distribution near the sediment-water interface, though adequate predictions of hyporheic residence times and flow paths can be made using an equivalent homogeneous permeability approximation.

Chapter 3 examines the impact of wood debris on hyporheic exchange using a similar numerical modeling approach to Chapter 2. I show that hyporheic exchange rates associated with wood debris increase with sediment permeability, the fraction of channel depth blocked by wood debris, and channel Froude number. This general finding should be broadly applicable to any in-stream flow obstacle.

Chapter 4 examines how hyporheic exchange associated with wood debris drives heat flow and thermal dynamics within the hyporheic zone and channel. Meter-scale hyporheic flow paths near wood debris cause spatial variations in diel temperatures within the ecologically sensitive hyporheic zone. Thermal zonation should increase hyporheic habitat diversity and impact rates of biogeochemical reactions. Hyporheic exchange associated with wood debris does not strongly impact thermal dynamics within the surface water, regardless of the amount of wood debris. These findings are based on novel experiments using a laboratory flume with surface water temperature control. Numerical models provide additional insight into the heat budget for the hyporheic zone.

In Chapter 5, I use a field-based approach to explore changes in hyporheic exchange associated with addition and removal of wood debris, and I assess implications for hyporheic thermal dynamics and conservative solute transport. A key result of this study is that broader patterns of river water downwelling (losing conditions) spatially restrict hyporheic exchange near wood debris. However, wood debris addition may have

the greatest ecological impact in losing streams where hyporheic exchange is otherwise minimal.

Chapter 6 examines the impact of river stage fluctuations on lateral hyporheic exchange in the banks of a large river. Changes in river stage (due to storms, snowmelt, or dam releases) induce steep but ephemeral hydraulic gradients within river banks that drive rapid river-groundwater exchange in the form of bank storage and release. Where river stage fluctuates daily due to regular dam releases, lateral hyporheic exchange can extend meters into the banks, and volumetric exchange rates can approach significant fractions of total surface water discharge. The oscillatory nature of these exchange flows may have implications for biogeochemical activity and ecological disturbance within riparian aquifers.

Chapter 7 synthesizes these findings and recommends future research.

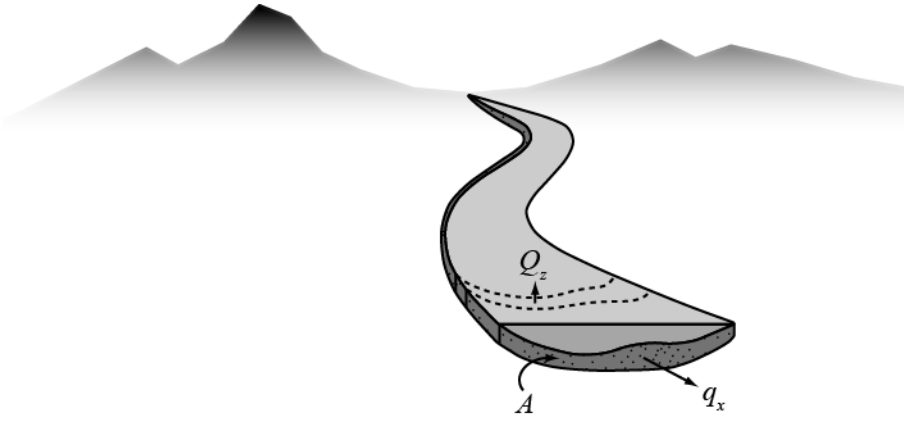


Figure 1.1: Conceptual model of hyporheic exchange (Q_z).

Chapter 2: Hyporheic Flow and Residence Time Distributions in Heterogeneous Cross-Bedded Sediment

2.1. ABSTRACT

The permeability heterogeneity of cross-bedded sediment increases path lengths of river-groundwater mixing (hyporheic exchange) in riverbeds and modifies the distribution of residence times. For two case studies, I numerically simulated fluid flow and solute transport through immobile bedforms composed of heterogeneous sediment and equivalent homogeneous sediment in order to clarify how cross-bedded permeability structures impact hyporheic exchange. The two permeability fields are from the cross-bedded Massillon Sandstone and modern climbing ripple deposits of the Brazos River (Texas). In both cases, permeability heterogeneity creates long hyporheic exchange paths but only slightly increases the depth of exchange relative to equivalent homogeneous sediment. In the Massillon example, permeability heterogeneity increases the proportion of long hyporheic residence times (> 3 days). In the Brazos example, permeability heterogeneity increases the proportion of short residence times (< 17 hours). I attribute the different responses in residence time distributions to differences in permeability patterns at the sediment-water interface. The tails of residence time distributions extend for tens of years and conform to a power law in both heterogeneous and homogeneous sediment. Current-bedform interactions are responsible for the long tails, as opposed to permeability heterogeneity.

2.2. INTRODUCTION

The riverbed is an important interface between surface water and groundwater. Fluid flow across the riverbed transports solutes and energy between aquatic and riparian ecosystems. River water infiltrates into the bed and banks, travels along short

groundwater flow paths, and returns to the channel. The resulting near-channel zone of surface water-groundwater mixing is the hyporheic zone, a critical ecological transition zone [Brunke and Gonser, 1997; Stanford and Ward, 1988]. Hyporheic flow occurs over a wide range of spatial scales (from bedform to catchment) and temporal scales (from minutes to weeks). As water flows through the hyporheic zone, time-dependent microbial reactions transform its chemical composition. The residence time of water in the hyporheic zone therefore determines the concentrations of both nutrients and contaminants within the sediment and surface water [Haggerty *et al.*, 2002].

Riverbed topography strongly influences residence times and path lengths. An undulating riverbed deflects currents, creating pressure gradients along the sediment-water interface that drive hyporheic exchange. Ripples, dunes, pools, steps, and riffles drive relatively short hyporheic flow paths [Cardenas, 2007; Elliott and Brooks, 1997b; Harvey and Bencala, 1993; Hester and Doyle, 2008; Thibodeaux and Boyle, 1987], while meanders promote longer paths [Boano *et al.*, 2006; Peterson and Sickbert, 2006]. Studies that characterize hyporheic exchange through bedforms and planforms typically assume the sediment is homogeneous for simplicity (i.e. Boano *et al.* [2006], Cardenas and Wilson [2007a], Elliot and Brooks [1997a; b], Harvey and Bencala [1993], Worman *et al.* [2006]).

Permeability heterogeneity in riverbed sediment also drives hyporheic exchange by deflecting flow downward into the sediment or upward into the channel [Vaux, 1968]. Permeability heterogeneity should therefore alter hyporheic exchange paths and residence times in bedforms and planforms, but few studies have quantified its influence. Salehin *et al.* [2004] constructed bedforms on top of a gridded, three-dimensional, lognormally correlated random permeability field in a flume and monitored hyporheic exchange through the sediment. Permeability heterogeneity reduced hyporheic exchange residence

times and penetration depths. How their results transfer to natural sedimentary deposits is uncertain. *Marion et al.* [2008] developed an analytical solution for the impact of horizontally layered permeability fields on hyporheic exchange and validated their solution with flume experiments. They showed that the proportion of short hyporheic residence times (~1 minute) increases in sediment with a highly permeable armored layer. *Cardenas et al.* [2004] numerically simulated hyporheic exchange through heterogeneous channel bend deposits. Their sensitivity analysis demonstrated that permeability heterogeneity with large variance and long correlation ranges can dominate hyporheic exchange in rivers. However, their study only considered one permeability field with large (meter-scale) correlation lengths. *Boano et al.* [2007] presented a model for solute transport and storage in rivers with heterogeneous bedform sizes and sediment permeability. They limited their analysis to fine permeability variations with a correlation length much less than the mean bedform wavelength.

The hierarchy of sedimentary units within fluvial deposits produces a hierarchy of permeability structures, from microform scale (laminations) to mesoform scale (crossbed sets) to macroform scale (point bar assemblages) [*Ritzi et al.*, 2004]. *Cardenas et al.* [2004] described how macro-scale permeability variations influence hyporheic exchange, while *Boano et al.* [2007] described the influence of micro-scale variations. To my knowledge, no study has tested the influence of meso-scale permeability variations on hyporheic exchange. This scale is relevant for two reasons. First, the depth of hyporheic exchange and the size of mesoforms both scale with bedform size. I interpret that hyporheic flow paths often encounter mesoforms such as cross beds that could influence the exchange. Unfortunately, meso-scale permeability heterogeneity is difficult if not impossible to measure in riverbeds or flumes, so previous studies have ignored its influence on hyporheic exchange. Second, evidence suggests that permeability and grain

size variations impact the ecological health and structure of hyporheic fauna and salmonid species, even at relatively small scales [*Boulton, 2007; Greig et al., 2007; Hakenkamp et al., 2002; Wagner and Bretschko, 2002*].

The goal of this study is to quantify how the permeability structure of mesoforms such as cross beds influences hyporheic exchange. For two case studies, I numerically simulate hyporheic exchange through immobile bedforms with cross-bedded permeability structures. In each case, I estimate the equivalent homogeneous permeability of the sediment and simulate hyporheic exchange in the homogeneous medium for comparison. I show that cross-bedded permeability structures do impact hyporheic exchange paths, but average exchange depths and fluxes are similar in heterogeneous and equivalent homogeneous sediment. While the permeability variations also impact the distribution of residence times, all distributions have power law tails. This important result implies that solute residence times span many orders of magnitude, regardless of permeability structure.

2.3. METHODS

2.3.1. Permeability Datasets

The Massillon Sandstone dataset consists of high-resolution, direct permeability measurements. Using a gas minipermeameter, *Tidwell and Wilson [2000; 2002]* acquired 2500 permeability measurements at intervals of 1.27 cm on a two-dimensional face of the Massillon Sandstone (Figure 2.1a). They used a minipermeameter tip seal with inner radius of 0.31 cm, which suggests the measurement support volume was on the order of a cubic centimeter. To my knowledge, this dataset represents the most detailed permeability map generated directly from cross-bedded sediment. Because diagenetic alterations have likely decreased the permeability of the Massillon Sandstone [*Tidwell*

and Wilson, 2002], I uniformly scaled the permeability field by a factor of 10. The average scaled permeability is $1.8 \times 10^{-11} \text{ m}^2$, typical of clean sand [Freeze and Cherry, 1979] (Figure 2.1a).

We also developed a second permeability field from an image of climbing ripple deposits excavated within a point bar of the Brazos River near Wallis, Texas (Figures 2.1b and 2.1c). The bimodal deposits are composed of clean sand, which appears lighter in photograph, and dark organic-rich silt, which appears darker in photograph (Figure 2.1b). Tidwell and Wilson [2002] showed that images can be used to delineate spatial permeability patterns where direct measurements are lacking, especially in rocks with sharp permeability transitions. Due to the difficulty of obtaining high-resolution permeability measurements in unlithified sediment, I assumed a relationship between image grayscale values and permeability. Specifically, I normalized grayscale values between zero and one and linearly translated them to log-permeability values between -10 and -12. As a result, the permeability of dark silt is approximately 10^{-12} m^2 , and the permeability of light sand is approximately 10^{-10} m^2 [Freeze and Cherry, 1979].

2.3.2. Geostatistical Analysis

To describe the spatial correlation of permeability, I report semivariogram models for the log-permeability data. Tidwell and Wilson [2000] computed experimental and model semivariograms for the Massillon data. For the Brazos data, I computed experimental and model semivariograms using GSLIB [Deutsch and Journel, 1998]. The experimental semivariogram, $\gamma(\underline{h})$, is half the average squared difference between two attribute values, $y(\underline{u}_i)$ and $y(\underline{u}_i + \underline{h})$, separated by lag vector \underline{h} :

$$\gamma(\underline{h}) = \frac{1}{2n(\underline{h})} \sum_{i=1}^{n(\underline{h})} (y(\underline{u}_i) - y(\underline{u}_i + \underline{h}))^2, \quad (2.1)$$

where $n(\underline{h})$ is the number of pairs [Deutsch and Journel, 1998]. The model semivariogram is composed of p semivariogram structures:

$$\gamma(\underline{h}) = \sum_{i=1}^p c_i \Gamma_i \left(\frac{\underline{h}}{\underline{a}_i} \right), \quad (2.2)$$

where each semivariogram structure (Γ_i) is defined by its shape, semivariance contribution (c_i), and range (\underline{a}_i). Mathematical forms for spherical, exponential, and hole structures are available in Deutsch and Journel [1998].

2.3.3. Estimating an Equivalent Homogeneous Permeability Tensor

For both the Massillon and Brazos permeability fields, I estimated an equivalent homogeneous permeability tensor using the method of Durlafsky [1991]. The numerical method mimics two constant-head permeameter tests in orthogonal directions. For each direction, steady flow is simulated across the heterogeneous permeability field. In the first simulation, left and right boundaries are spatially periodic in head drop, while top and bottom boundaries are spatially periodic in head. In the second simulation, the boundary conditions are rotated such that the sides have periodic head, and the top and bottom have a periodic head drop. Periodic boundary conditions ensure a symmetrical equivalent permeability tensor [Durlafsky, 1991; Renard and de Marsily, 1997]. The four components of the equivalent permeability tensor are obtained from mean flux across the two pairs of periodic boundaries in the two simulations.

2.3.4. Hyporheic Flow and Solute Transport Simulations

In simulations with heterogeneous permeability fields, I shaped the top of the domain to resemble repeating bedforms (i.e. Figure 2.2a). Two criteria guided my choice of bedform wavelength. I maximized the number of bedforms within the computational domain while maintaining a bedform wavelength on the order of the permeability correlation length. In the Massillon case study, the bedform wavelength is 20 cm (one

third of the width of the permeability field). I vertically positioned the bedform troughs within a low-permeability bounding surface. This configuration implies that the bedform train truncated the underlying cross beds. In the Brazos case study, the bedform wavelength is 10 cm, which is the approximate horizontal length scale of repeating permeability patterns. I laterally positioned the bedform troughs in less permeable zones. This configuration implies that the troughs of climbing ripples preferentially trapped finer sediment. In all simulations, the bedform height-to-wavelength ratio is 0.05, and the lee slope is 27° .

Using both heterogeneous and equivalent homogeneous permeability fields, I simulated hyporheic flow through bedforms following the method of *Cardenas and Wilson* [2007]. Turbulent flow over repeating bedforms and porous flow within the sediment are linked through the pressure distribution at the sediment-water interface (see Figure 1 of *Cardenas and Wilson* [2007]). First, two-dimensional steady-state turbulent flow over impermeable periodic bedforms is solved using the steady-state Reynolds-averaged Navier-Stokes (RANS) equations with the $k-\omega$ closure scheme. The sediment-water interface is a no-slip boundary, and the top of the water column is a symmetry boundary. Side boundaries are spatially periodic with a prescribed pressure drop representative of the channel slope. Detailed discussion of the methodology, turbulent flow behavior, and model validation are available in *Cardenas and Wilson* [2007a].

Next, two-dimensional porous flow in sediment is solved using the steady-state groundwater flow equation:

$$\nabla \cdot \left(-\frac{\underline{k}}{\mu} \nabla P \right) = 0, \quad (2.3)$$

where \underline{k} is the full permeability tensor, μ is viscosity, and P is total pressure (the sum of static, dynamic, and elevation components). The sediment-water interface is assigned the total pressure gradient from the turbulent channel flow simulation. The base of the

porous flow domain is a no-flow boundary, and the left and right sides are spatially periodic boundaries with a pressure drop representative of the channel slope.

Porous fluid flow simulations provide the velocity field for transient solute transport simulations. The advection-diffusion-dispersion equation describes solute transport in porous sediment:

$$\frac{\partial C}{\partial t} = -\nabla \cdot (\underline{v}C) + \nabla \cdot (\underline{D}\nabla C), \quad (2.4)$$

where C is concentration, t is time, and \underline{v} is seepage velocity, which has components v_x and v_z . \underline{D} is the full mechanical dispersion tensor with components:

$$D_{xx} = \alpha_L \frac{v_x^2}{|\underline{v}|} + \alpha_T \frac{v_z^2}{|\underline{v}|} + D_m', \quad (2.5a)$$

$$D_{xz} = D_{zx} = (\alpha_L - \alpha_T) \frac{v_x v_z}{|\underline{v}|}, \quad (2.5b)$$

and

$$D_{zz} = \alpha_L \frac{v_z^2}{|\underline{v}|} + \alpha_T \frac{v_x^2}{|\underline{v}|} + D_m'. \quad (2.5c)$$

α_T and α_L are transverse and longitudinal dispersivities, and D_m' is the molecular diffusion coefficient in porous media. In all simulations, the porosity is 0.30, D_m' is 5×10^{-11} m²/s, and α_T is 1/10 of α_L (Table 2.1). To represent pore-scale dispersion, α_L is approximately several grain diameters. I did not include macroscopic dispersivity in any simulation. Macroscopic dispersion accounts for the bulk effect of permeability heterogeneity on solute transport. In heterogeneous simulations, the permeability field is known, and macroscopic dispersion would “double-count” the influence of permeability heterogeneity. In homogeneous simulations, my goal was to simulate solute transport in truly homogeneous sediment for comparison with heterogeneous simulations.

Solute transport simulations mimic penetration of river water with constant conservative solute concentration (C_0) into the hyporheic zone [Cardenas *et al.*, 2008].

Initial solute concentration in the sediment is zero. Along the sediment-water interface, downwelling zones have a constant normalized concentration (C/C_0) of 1.0. Upwelling zones are convective flux boundaries. The model sides are periodic concentration boundaries, and the base is a convective flux boundary. Solute breakthrough curves are calculated as the flux-weighted normalized mean upwelling concentration (C_u/C_0). At each time step, the flux-weighted concentration is integrated over upwelling boundaries and divided by the flux-weighted concentration integrated over downwelling boundaries. The residence time distribution is the time derivative of the normalized flux-weighted breakthrough curve.

The RANS equations are solved using the finite-volume approach implemented in FLUENT [*Fluent Inc.*, 2006]. I checked for grid dependence by repeating simulations with refined meshes. The groundwater flow and solute transport equations are solved using the finite-element approach in COMSOL Multiphysics [*COMSOL AB*, 2006]. The sediment domain consists of Lagrange-quadratic triangular elements with node spacing of less than 1 mm at the top and less than 5 mm at the base. I tested for mesh dependence and positioned the basal boundary sufficiently far from the hyporheic zone to eliminate its influence on the solution.

2.4. MASSILLON SANDSTONE: A CROSS-BEDDED SAND CASE STUDY

2.4.1. Lithology

The Massillon Sandstone (Pennsylvanian age) is a moderately well sorted, medium-grained quartz sandstone. Cross-stratified sets are 16-22 cm in thickness and are bounded by subhorizontal, undulatory to planar surfaces (Figure 2.1a). Within each set, unidirectional laminae are 0.5-2.0 cm thick and have apparent dips from 10° to 22° . Evidence of diagenetic alteration includes hydrous iron oxide precipitates and quartz

overgrowths [Tidwell and Wilson, 2000; 2002]. The depositional environment has been interpreted as high-energy fluvial or tidal [Gray, 1956; Schmidley, 1987].

2.4.2. Geostatistical Properties

Permeability values range by 1.2 orders of magnitude, and the geometric mean permeability is $1.8 \times 10^{-11} \text{ m}^2$. The semivariogram of the log-permeability field exhibits three nested structures: a small-scale structure associated with low-angle laminae, a large-scale structure associated with cross bed sets, and a periodic “hole” structure associated with the repetition of less permeable bounding surfaces (see Figure 7 of Tidwell and Wilson [2000]) (Table 2.2). The longest spatial correlation is in the direction parallel to bounding surfaces (nearly horizontal) [Tidwell and Wilson, 2000].

2.4.3. Hyporheic Flow and Transport in Heterogeneous Medium

The average hyporheic exchange depth over the three bedforms is 16.9 cm, calculated as the hyporheic exchange area divided by domain width. The average exchange depth is 84% of the bedform wavelength. The hyporheic exchange zone exhibits complex flow paths of varying length (Figure 2.2a). Shorter exchange paths enter the hyporheic zone at the stoss face of one bedform and return to the channel at an adjacent upwelling zone. These exchange paths represent approximately 89% of the total exchange area. The remaining exchange paths are significantly longer because they connect non-adjacent upwelling and downwelling zones on different bedforms. The average hyporheic exchange flux across the sediment-water interface is $7.12 \times 10^{-8} \text{ m/s}$. The characteristic hyporheic residence time, calculated as the average hyporheic depth divided by the average exchange flux, is 27.4 days.

2.4.4. Hyporheic Flow and Transport in Homogeneous Medium

The Massillon Sandstone has an equivalent anisotropy ratio (k_{max}/k_{min}) of 1.09, with a maximum permeability (k_{max}) of $2.07 \times 10^{-11} \text{ m}^2$ that dips 1.3° downstream. The maximum permeability direction is parallel to subhorizontal bounding surfaces (Figure 2.1). The average hyporheic exchange depth across the three bedforms is 15.0 cm, which is slightly less than the exchange depth in the heterogeneous medium (Figure 2.2). Unlike in heterogeneous sediment, hyporheic flow paths only connect adjacent upwelling and downwelling zones (Figure 2.2b). The average hyporheic exchange flux across the sediment-water interface is $8.92 \times 10^{-8} \text{ m/s}$, which is greater than the exchange flux in heterogeneous sediment. The characteristic hyporheic residence time is 19.8 days, which is less than in heterogeneous sediment.

Figure 2.3 compares the conservative solute breakthrough curves and residence time distributions for heterogeneous and homogeneous sediment. The breakthrough curve initially climbs faster in homogeneous sediment. C_u/C_0 reaches 50% after 36 hours in homogeneous sediment and after 50 hours in heterogeneous sediment. Accordingly, the homogeneous sediment has a greater frequency of residence times less than $3 \times 10^5 \text{ s}$ (3 days), while the heterogeneous sediment has a greater frequency of residence times greater than $3 \times 10^5 \text{ s}$. Both residence time distributions have power-law tails that end at a maximum residence time of approximately 30 years ($\sim 10^9$ seconds).

2.5. BRAZOS RIVER SEDIMENT: A CLIMBING RIPPLE CASE STUDY

2.5.1. Lithologic Description

The Brazos River sediment is ripple-laminated and bimodal in composition. The modes are fine sand and organic-rich silt. Over the entire exposure (approximately one meter in thickness), the angle of ripple climb steepens from 15° near the base to 40° near

the top (Figure 2.1b). The transport dynamics associated with ripple formation and migration typically create local grain size patterns. Often, the finest sediment is located on ripple stoss faces, while the coarsest sediment is located on lee faces [Allen, 1971]. However, the inverse can also occur, where suspended silts become trapped and deposited in recirculation zones behind ripple crests. In this case, the coarsest sediment is preserved on ripple stoss faces updip of eddy reattachment points, while fine sediment is deposited on lee faces and in ripple swales. In the Brazos River sediment, I interpret the darker silt as the preserved ripple swales and the lighter sand as the preserved upper stoss faces.

2.5.2. Geostatistical Properties

The geometric mean permeability of the Brazos dataset is $1.2 \times 10^{-11} \text{ m}^2$. The experimental semivariogram of log-permeabilities exhibits four nested structures (Figure 2.4, Table 2.2). Alignment of sand and silt lenses gives rise to a periodic “hole” structure with a range of 5 cm perpendicular to the direction of climb (Figure 2.4b). The other structures include a small-scale spherical structure with a range of 4 cm and a large-scale spherical structure with a range of 14 cm (Figure 2.4a). The experimental semivariogram exhibits zonal anisotropy at the large scale, with a greater variance contribution parallel to ripple climb (Table 2.2).

2.5.3. Hyporheic Flow and Transport in Heterogeneous Medium

The average hyporheic exchange depth within heterogeneous sediment is 9.9 cm (99% of the bedform wavelength). Like the Massillon Sandstone, the Brazos sediment contains deep flow paths that connect non-adjacent bedforms (Figure 2.5a). The shallow exchange zones, which connect adjacent downwelling and upwelling regions, represent approximately 63% of the total exchange area. The average hyporheic exchange flux

across the sediment-water interface is 7.87×10^{-8} m/s. The characteristic hyporheic residence time is 14.5 days.

2.5.4. Hyporheic Flow and Transport in Homogeneous Medium

The Brazos sediment has an equivalent anisotropy ratio of 1.66, with a maximum permeability of 1.53×10^{-11} m² that dips 29.2° upstream. The direction of maximum permeability is parallel to the angle of climb (Figure 2.1c). The average hyporheic exchange depth across the three bedforms is 8.0 cm, which is less than the exchange depth in the heterogeneous medium. Hyporheic exchange paths only connect adjacent downwelling and upwelling zones (Figure 2.5b). The average hyporheic exchange flux across the sediment-water interface is 6.40×10^{-8} m/s, which is less than the flux in heterogeneous sediment. The characteristic hyporheic residence time is 14.4 days, almost equal to that in heterogeneous sediment.

Solute breakthrough is initially faster in heterogeneous than homogeneous sediment (Figure 2.6a). C_w/C_0 reaches 50% after 11 hours in heterogeneous sediment and after 23 hours in homogeneous sediment. Accordingly, the heterogeneous sediment has a greater proportion of short residence times ($< 5 \times 10^4$ seconds, or 17 hours) than homogeneous sediment (Figure 2.6b). The heterogeneous sediment also has a smaller proportion of intermediate residence times between 5×10^4 seconds (17 hours) and 1×10^6 seconds (2 weeks). Again, the tails of both residence time distributions follow a power law until the maximum residence time, approximately 10^9 seconds (30 years).

2.6. PERMEABILITY ANISOTROPY SENSITIVITY STUDY

To assess the sensitivity of hyporheic exchange to permeability anisotropy, I also conducted simulations in homogeneous sediment for a range of anisotropic permeability tensors. A given permeability anisotropy tensor can represent cross-bedded sediment

with preferential flow parallel to bounding surfaces, slip faces, or angle of bedform climb. For all simulations, the bedform wavelength is 1 m (Table 2.1), and k_{min} is 10^{-10} m², corresponding to very coarse sand [Freeze and Cherry, 1979].

Hyporheic exchange depth varies in response to both the anisotropy ratio (k_{max}/k_{min}) and orientation of k_{max} (Figures 2.7 and 2.8). As k_{max}/k_{min} increases, the hyporheic exchange zone deepens if k_{max} is near vertical. In contrast, if k_{max} is near horizontal, the hyporheic exchange zone becomes more compressed with increasing k_{max}/k_{min} . Notably, the hyporheic exchange depth is sensitive to the dip magnitude of k_{max} but insensitive to its upstream or downstream orientation. For example, the hyporheic exchange depths are similar whether the dip of k_{max} is -45° (upstream) or $+45^\circ$ (downstream) (Figures 2.7 and 2.8a).

The mean hyporheic flux is relatively insensitive to the orientation of the permeability tensor (Figure 2.8b). Hyporheic flux increases with k_{max}/k_{min} , regardless of k_{max} direction. The characteristic hyporheic residence time varies with both k_{max}/k_{min} and the orientation of k_{max} (Figure 2.8c). If k_{max} is nearly horizontal, the characteristic hyporheic residence time decreases with increasing k_{max}/k_{min} —hyporheic flow paths become increasingly shallow and fast. If k_{max} is nearly vertical, the characteristic hyporheic residence time remains constant with increasing k_{max}/k_{min} —deeper flow paths are offset by faster flux rates (compare Figures 2.8a and 2.8b for k_{max} dip of 90°).

The k_{max} direction impacts the solute breakthrough behavior and shape of the residence time distribution (Figure 2.9). A horizontal k_{max} favors short residence times more than a vertical k_{max} —the breakthrough curve initially climbs faster if the dip of k_{max} is small (Figure 2.9a). At late time, the breakthrough curve climbs faster if the dip of k_{max} is large. Accordingly, the residence time distribution has a broader tail for vertical k_{max}

directions (Figure 2.9b). The tails of the residence time distributions all follow a power law for tens of years.

2.7. DISCUSSION

In both case studies, permeability heterogeneity impacts hyporheic flow paths. In heterogeneous sediment, the flow paths are slightly deeper, and long paths connect non-adjacent bedforms. Hyporheic flow paths in homogeneous sediment with periodic bedforms only connect adjacent downwelling and upwelling zones. *Woessner* [2000] also presented a case where permeability heterogeneity induced deeper, longer flow paths (see Figure 6 in *Woessner* [2000]). However, some heterogeneous permeability fields may restrict the depth of hyporheic exchange rather than increase it. For example, *Salehin et al.* [2004] found that heterogeneity limited the depth of hyporheic mixing and also decreased residence times. The effective anisotropy of their permeability fields favored lateral flow. My simulations of hyporheic exchange in anisotropic homogeneous sediment also demonstrate that when the preferential flow direction is horizontal, exchange depths and residence times tend to decrease. A general observation is that permeability heterogeneity increases the complexity of hyporheic exchange paths but may increase or decrease the depth of mixing, depending on the permeability structure.

In spite of the differences between hyporheic flow paths in heterogeneous and equivalent homogeneous sediment, simulations using the homogeneous equivalent permeability tensor predict hyporheic metrics in heterogeneous sediment fairly well. The homogeneous simulation under-predicted the hyporheic zone depth by 10% for the Massillon Sandstone and by 24% for the Brazos sediment. With respect to the hyporheic flux across the sediment-water interface, the homogeneous simulation overestimated flux by 20% for the Massillon Sandstone and underestimated the flux by 23% for the Brazos sediment.

The implication is that current-bedform interactions primarily control hyporheic metrics in my two case studies. *Cardenas et al.* [2004] presented a dimensionless number for quantifying the relative influence of bedform-current interactions (external forcing) and permeability heterogeneity (internal forcing) on hyporheic exchange:

$$N = \frac{S\sigma_{\ln k}^2 l_z \lambda}{4Ad_{HZ}}. \quad (2.6)$$

S is the hydraulic gradient in the channel, A is the amplitude of the pressure field associated with bedform-current interactions, λ is the bedform wavelength, d_{HZ} is the depth of the hyporheic zone in equivalent homogeneous sediment, $\sigma_{\ln k}^2$ is the variance of the natural-log permeability field, and l_z is the vertical correlation length of the permeability field. Large values of N indicate that permeability heterogeneity primarily drives hyporheic exchange, while small values indicate that bedform-current interactions are the primary driver. I calculated N for the Massillon and Brazos cases (Table 2.3). For the vertical correlation length (l_z), I assumed half the vertical wavelength of the semivariogram hole structure (Table 2.2).

In both cases, N is small, suggesting that hyporheic exchange is dominated by bedform-current interactions. For permeability heterogeneity to dominate hyporheic exchange, the permeability correlation length or the variance would need to be much larger, all other factors held constant. If the two case studies examined here are representative of typical correlation lengths and variances for cross bed mesoforms, then meso-scale permeability structure has a limited influence on hyporheic exchange through bedforms. However, larger-scale permeability variations across multiple depositional units such as scroll bars, trough sets, and mud drapes could strongly control hyporheic exchange.

For my two case studies, solute distributions within the sediment were also relatively insensitive to permeability heterogeneity. Figure 2.10 illustrates vertical

concentration profiles at six time intervals for both the heterogeneous Brazos sediment and its homogeneous equivalent sediment. The penetration depths are similar for all times (also compare C/C_0 contours in Figures 2.2 and 2.5). Near the sediment-water interface, bedform-current interactions predominantly control hyporheic exchange. The pressure gradients are greatest, and the path lengths are short compared with the length scale of permeability heterogeneity. Therefore, solute penetration is relatively insensitive to permeability heterogeneity. Deeper in the hyporheic zone, pressure gradients are small, and longer flow paths sample more of the permeability range. Permeability heterogeneity could potentially impact solute transport, but seepage velocities decay logarithmically with depth, so diffusion and pore-scale dispersion effectively redistribute solute along flow paths. Therefore, permeability heterogeneity also has a weak influence on solute penetration at depth.

Permeability heterogeneity does impact the distribution of residence times, though all distributions have power-law tails. Permeability heterogeneity can increase or decrease the proportion of short or long residence times. In the Massillon Sandstone, permeability heterogeneity increases the proportion of longer residence times (greater than 3 days). In the Brazos sediment, permeability heterogeneity increases the proportion of shorter residence times (less than 17 hours). Notably, a different choice in the homogeneous equivalent permeability tensor could improve agreement between heterogeneous and homogeneous residence time distributions at early times or late times, but not both. Because permeability heterogeneity alters the shape of the residence time distribution, no single equivalent permeability tensor can accurately reproduce residence times in heterogeneous sediment.

The permeability distribution near the sediment-water interface appears to strongly influence the residence time behavior. The Massillon Sandstone has a low-

permeability bounding surface near the sediment-water interface. On average, the low-permeability surface tends to increase solute residence times. However, the shallowest hyporheic paths near the crests of bedforms pass unimpeded through moderate permeabilities. As a result, the initial solute arrival times at upwelling zones are similar in both the heterogeneous and equivalent homogeneous sediment, but heterogeneity delays solute arrival at later times. Unlike the Massillon Sandstone, the Brazos sediment manifests the full range of permeability near the sediment-water interface. High and low permeability zones alternate along the bedform train. In the rightmost bedform, two transitions between upwelling and downwelling occur in a highly permeable zone (Figure 2.5a). As a result, solute arrives much earlier at upwelling zones in heterogeneous sediment than in homogeneous sediment. At later times however, the breakthrough curve for heterogeneous sediment climbs slowly because deeper hyporheic flow paths inevitably encounter lower permeability regions that delay the travel time. A key conclusion is that subtleties in permeability heterogeneity near the sediment-water interface can lead to measurable differences in solute residence times.

Our numerical experiments have limitations. First, this study considers only two examples of cross-bedded permeability fields. I propose that these cases are nonetheless representative of a wide (yet limited) range of mesoform permeability structures (refer to *Weber* [1982], *Scheibe and Freyberg* [1995], and *Huysmans et al.* [2008] for other examples). Second, I represent three-dimensional bedforms and permeability structures using two-dimensional cross-sections. Bedforms tend to exhibit the greatest topographic variation in the streamwise direction, and hydrodynamic grainsize sorting processes should similarly produce strong permeability variations in the streamwise direction. I therefore believe the two-dimensional simulations capture the primary behavior of hyporheic flow, though three-dimensional simulations would increase the complexity of

flow paths. Third, the domain of my numerical simulations is periodic but only spans three bedforms, which limits the potential length of all hyporheic flow paths to approximately three bedform wavelengths. I suggest, however, that hyporheic flow paths between non-adjacent bedforms weakly influence solute transport and storage for two reasons. First, solute flux along these paths represents a very small portion of the total solute flux through the hyporheic zone. Second, diffusion and pore-scale dispersion strongly influence solute transport along these flow paths.

Our two case studies illustrate how cross-bedded permeability structures impact hyporheic exchange and solute transport. Regardless of permeability structure, all flux-weighted residence time distributions follow a power-law relationship for tens of years. The key implication is that hyporheic residence times can vary over many orders of magnitude, even in rivers with uniform bedform wavelengths and relatively homogeneous sediment. Permeability heterogeneity may modify the details of the residence time distribution but does not alter the form of the power-law tail.

2.8. CONCLUSIONS

We have demonstrated in two cases that the permeability structure of cross-bedded sediment can produce long hyporheic exchange paths but only slightly modifies the average exchange depth beneath bedforms. The primary forcing mechanism is bedform-current interactions. Additionally, conservative solute distributions within the hyporheic zone are relatively insensitive to the permeability heterogeneity of cross-bedded sediment. Therefore, approximating cross-bedded sediment as homogeneous and anisotropic (or even isotropic) is reasonable, if the goal is to understand or describe first-order patterns in hyporheic exchange fluxes and solute distributions within riverbeds. However, this study in no way refutes the impact of large-scale permeability

heterogeneity on hyporheic exchange (where correlation lengths greatly exceed the bedform wavelength).

Cross-bedded permeability structures do impact the distribution of hyporheic residence times. Permeability heterogeneity can increase the proportion of short or long residence times. The shape of the residence time distribution appears to be most sensitive to permeability patterns near the sediment-water interface. However, the tails of the residence time distributions follow a power law, regardless of permeability structure. Persistent solute retention in riverbeds does not require large variations in sediment permeability or bedform wavelength.

2.9. NOTATION

a	semivariogram range, [L]
A	amplitude of dynamic pressure wave, [$M L^{-1} T^{-2}$]
c	semivariogram sill contribution, []
C	concentration, [$M L^{-3}$]
C_u	mean flux-weighted concentration at upwelling zones, [$M L^{-3}$]
C_0	reference concentration in surface water, [$M L^{-3}$]
\underline{D}	dispersion tensor, [$L^2 T^{-1}$]
d_{HZ}	depth of hyporheic exchange zone, [L]
D_m'	molecular diffusion coefficient in porous media, [$L^2 T^{-1}$]
\underline{h}	vector lag, [L]
\underline{k}	permeability tensor, [L^2]
l_z	vertical correlation length of permeability field, [L]
N	measure of hyporheic exchange forcing mechanisms, []
P	pressure, [$M L^{-1} T^{-2}$]
Pe	Peclet number, []
S	channel hydraulic gradient, []
t	time, [T]
\underline{v}	seepage velocity, [$L T^{-1}$]
x	longitudinal coordinate, [L]
$y(\underline{u})$	sample attribute value at location \underline{u} , []
z	vertical coordinate, [L]
α_L	longitudinal dispersivity, [L]
α_T	transverse dispersivity, [L]
Γ	semivariogram structure, []
γ	semivariogram, []
λ	bedform wavelength, [L]

μ dynamic viscosity, [M L⁻¹ T⁻¹]
 σ_{lnk}^2 variance of natural-log permeability field, []

	<i>Massillon Sandstone</i>	<i>Brazos Sediment</i>	<i>Homogeneous Anisotropic Sediment</i>
Mean hydraulic gradient, S [mm/m]	.194	.149	.095
Mean channel velocity [m/s]	0.10	0.10	0.10
Reynolds number []	20,000	20,000	50,000
Bedform wavelength, λ [m]	0.2	0.1	1.0
Bedform height [m]	0.01	0.005	0.05
Porosity []	0.3	0.3	0.3
Dynamic viscosity, μ [Pa s]	0.001	0.001	0.001
Longitudinal dispersivity, α_L [mm]	1	1	5
Transverse dispersivity, α_T [mm]	0.1	0.1	0.5
Molecular diffusion coefficient, D_m' [m ² /s]	5×10^{-11}	5×10^{-11}	5×10^{-11}

TABLE 2.1: NUMERICAL SIMULATION PARAMETERS.

	c []	<i>Structure</i>	a_{maj} [m] / <i>Dip</i> [°]	a_{min} [m]
<i>Massillon Sandstone</i>	.011	exponential	.04	.04
	.043	exponential	.348 / 0	.195
	.012	hole	∞ / 0	.18
<i>Brazos Sediment</i>	.012	spherical	.04	.04
	.007	spherical	.14	.14
	.013	spherical	∞ / 59	.14
	.024	hole ¹	∞ / -31	.050

TABLE 2.2: SEMIVARIOGRAM MODEL PROPERTIES for Massillon and Brazos permeability data. Downstream dips are positive. For Brazos Sediment, I used a damped hole effect structure with a decay parameter of 1.6×10^6 . The decay parameter represents the distance over which the sinusoidal variance contribution decays by 95%.

	S [mm/m]	λ [m]	A [mm]	σ_{hk}^2 []	l_z [m]	D_{HZ} [m]	N []
<i>Massillon Sandstone</i>	.194	0.20	.493	.148	.090	.153	.0017
<i>Brazos sediment</i>	.149	0.10	.317	.937	.021	.080	.0029

TABLE 2.3: EVALUATION OF EXTERNAL VERSUS INTERNAL FORCING MECHANISMS for hyperheic exchange through Massillon Sandstone and Brazos sediment.

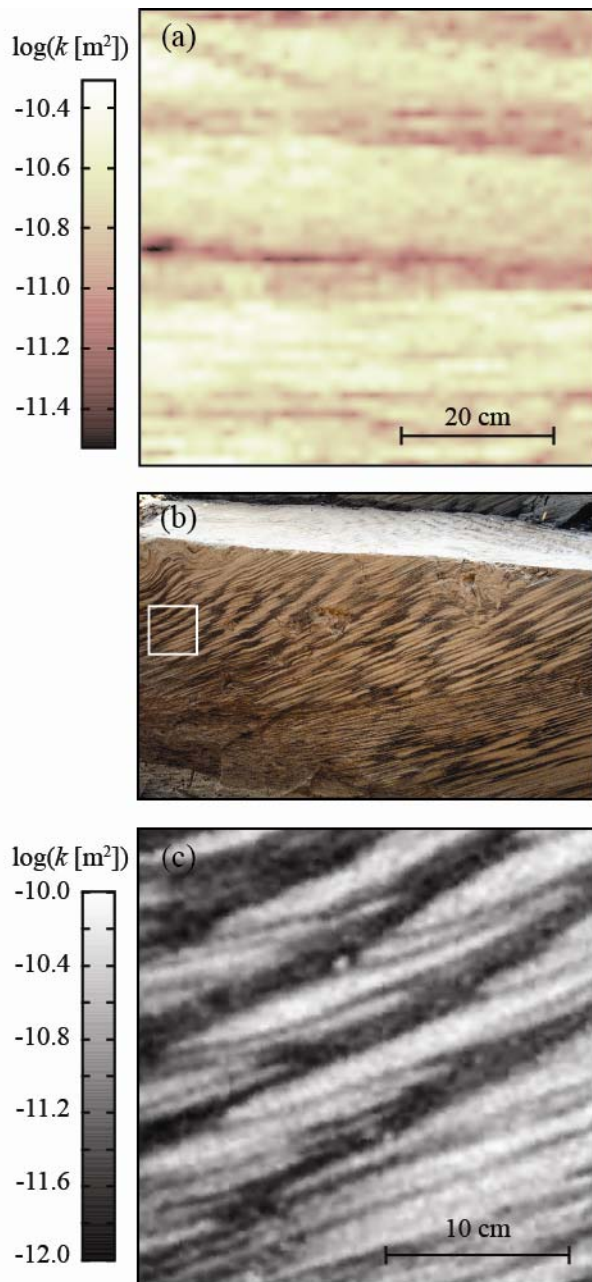


Figure 2.1: Permeability datasets. (a) Direct permeability measurements by *Tidwell and Wilson* [2000; 2002] on the cross-bedded Massillon Sandstone. (b) Photograph of modern climbing ripple deposits excavated from a point bar of the Brazos River, Texas, courtesy of Gary Kocurek (University of Texas-Austin). White box delineates region used in image analysis. (c) Permeability field from image analysis. Less permeable zones are associated with dark organic-rich silt. More permeable zones are associated with clean fine sand.

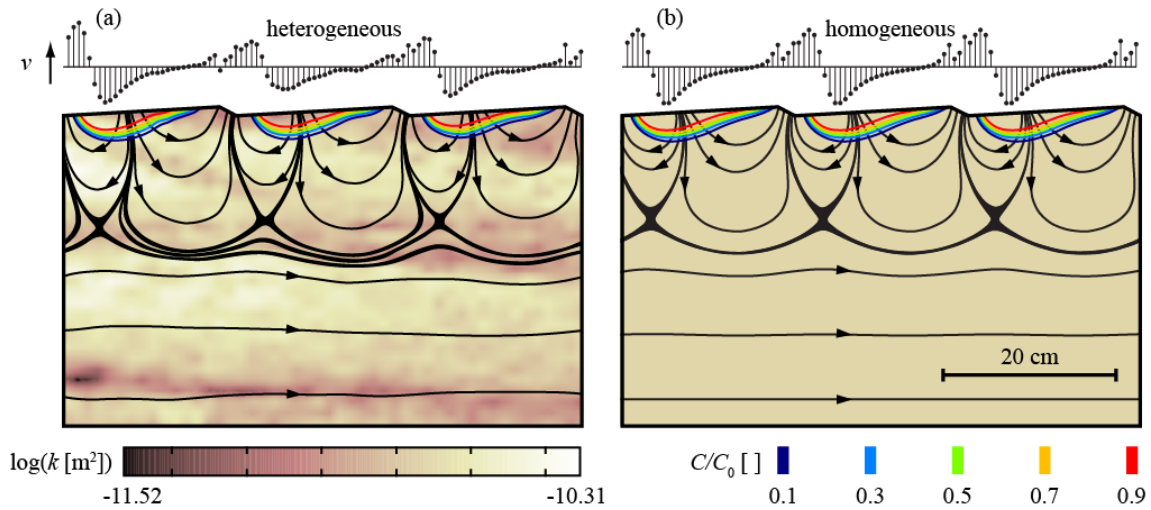


Figure 2.2: Simulated hyporheic exchange in (a) heterogeneous Massillon Sandstone and (b) equivalent homogeneous sediment. Flow in the channel is left to right. Streamlines are shown in black. Normalized seepage velocity across the sediment-water interface is plotted above the bedforms. The hyporheic zone is slightly deeper in heterogeneous sediment. Color contours indicate normalized solute concentrations (C/C_0) 12 hours after introduction of a conservative solute to the surface water.

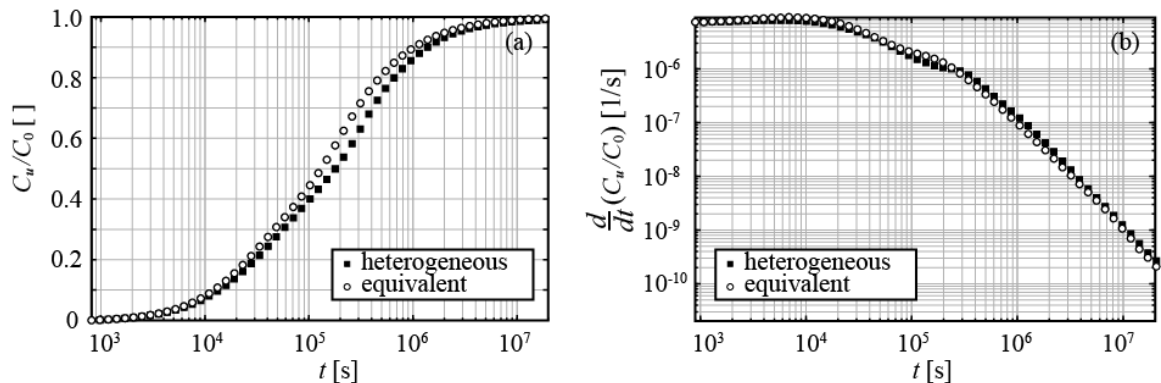


Figure 2.3: Breakthrough curves (a) for the heterogeneous Massillon Sandstone (black squares) and its homogeneous equivalent sediment (white circles). The breakthrough curve initially climbs faster in homogeneous sediment. Residence time distributions (b) for heterogeneous and homogeneous sediment. Both distributions have power-law tails with exponents of -1.92.

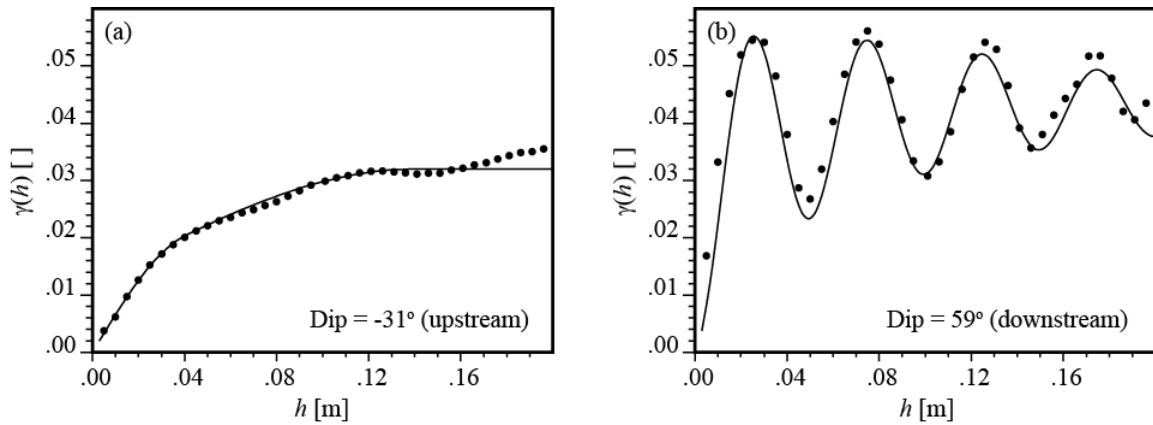


Figure 2.4: Experimental and model semivariograms for Brazos log-permeability values: (a) parallel to ripple climb and (b) perpendicular to climb. The semivariogram oscillates in the 59° dip direction due to the alternation of sand and silt bands.

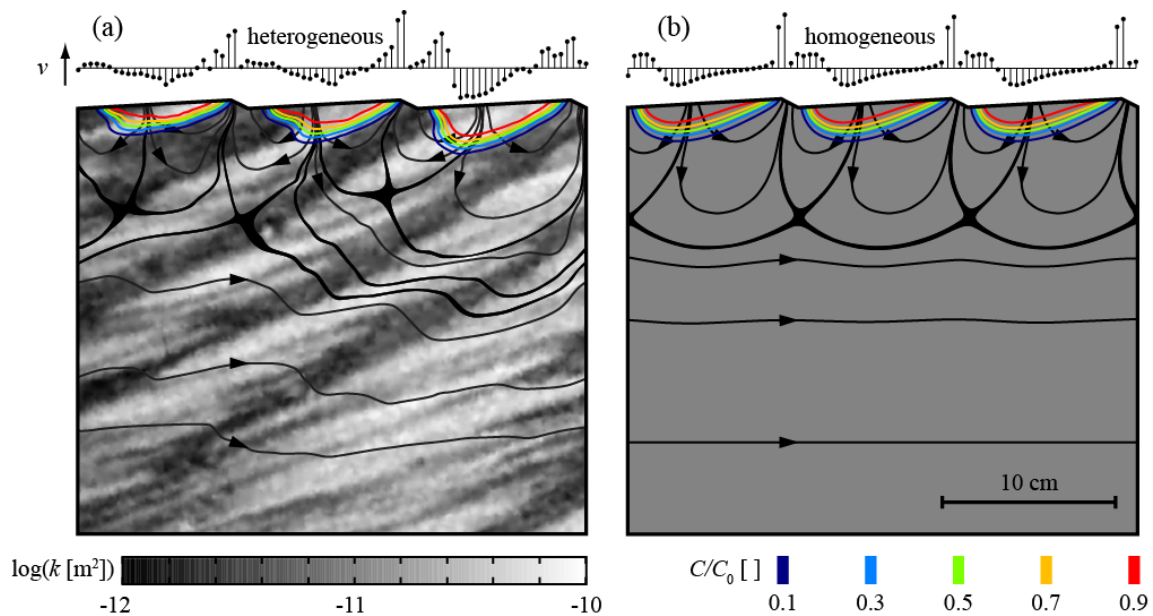


Figure 2.5: Simulated hyporheic exchange in (a) heterogeneous Brazos sediment and (b) equivalent homogeneous sediment. Flow in the channel is left to right. Streamlines are shown in black. Normalized seepage velocity across the sediment-water interface is plotted above the bedforms. The hyporheic zone is deeper in heterogeneous sediment. Color contours indicate normalized solute concentrations (C/C_0) 12 hours after introduction of a conservative solute to the surface water.

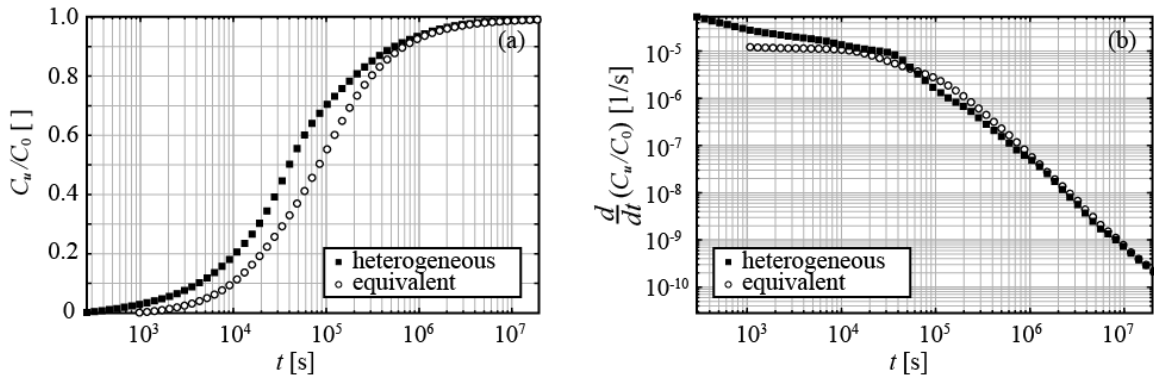


Figure 2.6: Breakthrough curves (a) for the heterogeneous Brazos sediment (black squares) and its homogeneous equivalent sediment (white circles). The breakthrough curve initially climbs faster in heterogeneous sediment. The residence time distribution in heterogeneous sediment strongly emphasizes short residence times (b). Power-law tails have exponents of -1.73 and -1.80 in heterogeneous and equivalent homogeneous sediment, respectively.

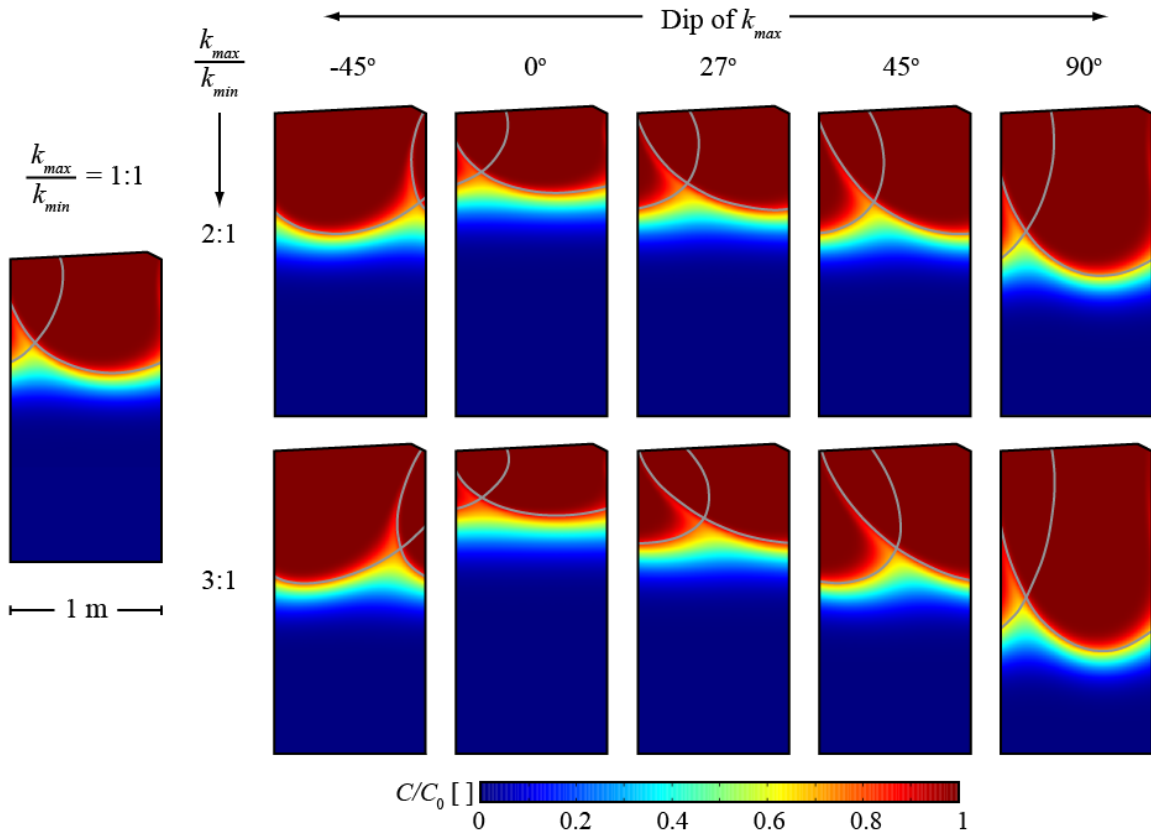


Figure 2.7: Hyporheic zones, delineated by gray streamlines, for various permeability anisotropy ratios (k_{max}/k_{min}) and directions of k_{max} . The hyporheic exchange zone is compressed for horizontal k_{max} orientations and elongated for vertical k_{max} orientations.

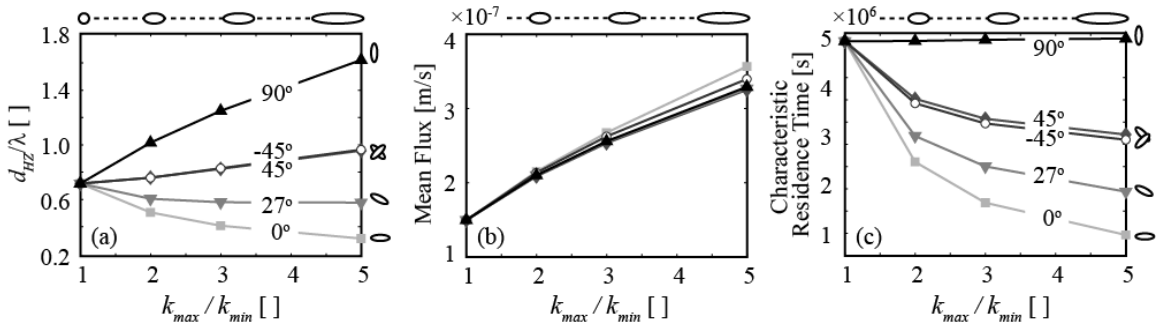


Figure 2.8: Hyporheic metrics. (a) Normalized hyporheic exchange depth as a function of k_{max}/k_{min} and dip of k_{max} . Ellipses graphically illustrate the permeability anisotropy tensors. (b) Mean hyporheic flux magnitude across the sediment-water interface as a function of k_{max}/k_{min} and dip of k_{max} . The rate of hyporheic exchange is insensitive to the orientation of k_{max} . (c) Characteristic residence time (exchange depth divided by mean hyporheic flux) as a function of k_{max}/k_{min} and dip of k_{max} . The characteristic residence time is most sensitive to k_{max}/k_{min} when k_{max} is horizontal.

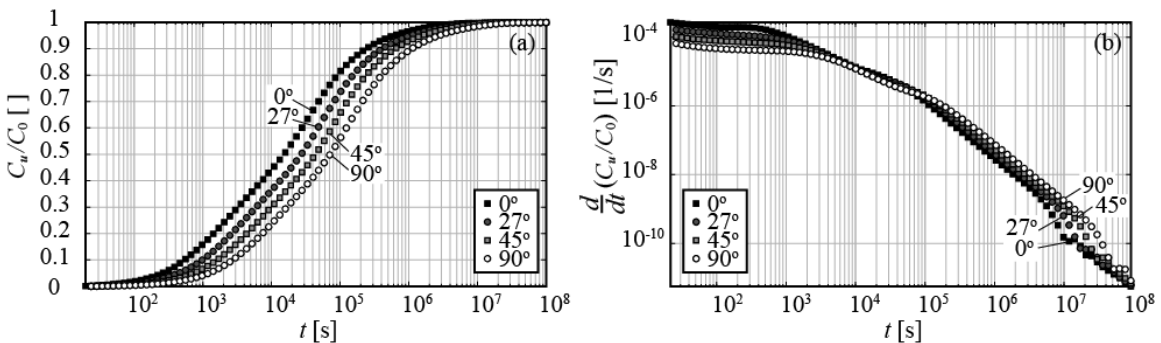


Figure 2.9: Breakthrough curves for homogeneous anisotropic sediment with various k_{max} directions (a). k_{max}/k_{min} is 3.0 in each case. Solute breakthrough is initially slower when k_{max} is vertical and hyporheic exchange is deep. Residence time distributions (b) for the four scenarios. The residence time distribution has a broader tail when k_{max} is vertical.

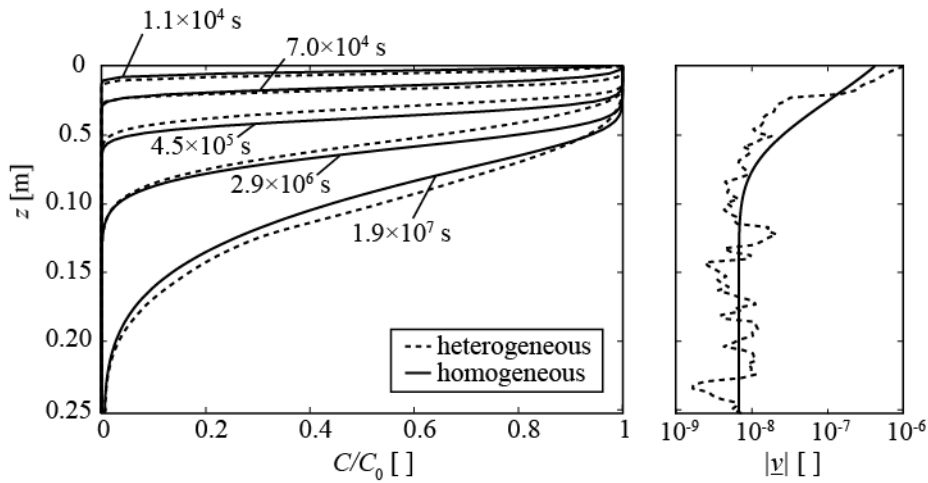


Figure 2.10: Concentration-depth profiles in heterogeneous Brazos sediment (dashed lines) and equivalent homogeneous sediment (solid lines) after introduction of conservative solute to the surface water. Concentration profiles are taken from a vertical line that bisects the central bedform (Figure 5). Solute penetration fronts are similar for both heterogeneous and homogeneous sediment. Because seepage velocity decays logarithmically with depth (right), advection does not strongly influence the deep, late-time penetration of solute into the sediment.

Chapter 3: River-groundwater exchange due to large woody debris

3.1. ABSTRACT

The flow of river water around large woody debris (LWD) creates pressure gradients along the riverbed that drive a large zone of river-groundwater mixing, or hyporheic exchange. Flume experiments and numerical simulations show that river water downwells into the riverbed upstream of a channel-spanning log and upwells downstream. Exchange rates are greatest near the log and decay exponentially with distance upstream and downstream. I developed equations for bed pressure profiles and hyporheic exchange rates in the vicinity of a channel-spanning log that can be used to evaluate the impact of LWD removal or re-introduction on hyporheic mixing. The magnitude of pressure disturbance along the bed (and thus hyporheic exchange) increases with the fraction of channel depth blocked by the log and channel Froude number. Exchange rates are relatively insensitive to vertical location of LWD in the channel. At natural densities, LWD in lowland streams drives reach-averaged hyporheic exchange rates similar to a ripple-covered bed. However, the length scales and residence times of hyporheic exchange due to LWD are greater. By removing LWD from streams, humans have altered patterns and rates of hyporheic exchange, which influence habitat distribution and quality for invertebrates and fish.

3.2. INTRODUCTION

Large woody debris (LWD) is a key component of natural streams that controls the flow of water [*Gippel, 1995; Shields and Gippel, 1995; Wilcox, 2006; Wilcox and Wohl, 2006*], sediment [*Montgomery et al., 1996*], organic carbon [*Bilby, 1981; Bilby and Likens, 1980*], and nutrients [*Ensign and Doyle, 2005; Webster, 2000*]. LWD also

promotes complex channel morphology, which improves habitat for invertebrates and fish [Abbe and Montgomery, 1996; Angermeier and Karr, 1984; Wallace et al., 1995; Wright and Flecker, 2004]. LWD density has declined in many of the world's rivers due to historic channel clearing and riparian logging practices. Clearing removes existing LWD, while riparian logging depletes future sources of LWD [Montgomery and Piégay, 2003; Shields et al., 2006]. As a result, LWD reintroduction has become an increasingly common tool for restoring rivers to their natural states [Braudrick and Grant, 2000; Gippel, 1995].

One anticipated benefit of LWD reintroduction is an increase in hydrologic connectivity between rivers and surrounding aquifers, primarily through hyporheic exchange. Hyporheic exchange within shallow river sediment transports heat and biologically important solutes between river and terrestrial ecosystems [Boulton, 2007; Brunke and Gonser, 1997; Stanford and Ward, 1988]. By increasing connectivity between rivers and groundwater, LWD may buffer aquatic habitats against nutrient loading [Boulton, 2007] and thermal degradation due to climate change, heat pollution, and land use change [Poole and Berman, 2001].

While several field and laboratory studies have suggested that LWD enhances hyporheic exchange, no study has characterized the general hyporheic response to LWD and determined its controlling factors. Lautz et al. [2006] showed in a small meadow stream that debris dams and tight meanders promoted hyporheic flow paths with similar length scales and travel times. Lautz and Fanelli [2008] identified zonations in vertical fluid flow and biogeochemical processes in a riverbed upstream and downstream of a log dam restoration structure. Mutz et al. [2007] conducted a hydraulic tracer study in a low-energy sand bed flume and showed that hyporheic flux doubled after the addition of model wood debris. Wondzell et al. [2009] monitored changes in hyporheic exchange

following LWD removal in a small, low-gradient stream and found that hyporheic exchange initially declined but recovered several years later as alternating bars developed.

Here, I quantify hyporheic exchange induced by LWD for the specific case of submerged, channel-spanning logs. I first present detailed descriptions of hyporheic exchange based on measurements and simulations for two flume experiments that span subcritical and supercritical flow conditions. Next, I examine the influence of scour morphology near LWD on hyporheic mixing. Finally, I develop empirical relationships for bed pressure profiles and hyporheic exchange near channel-spanning logs based on expanded flume measurements and simulations. These relationships can be used to assess the impact of LWD removal or addition on hydrologic connections between rivers and their adjacent aquifers.

3.3. METHODS

3.3.1. Flume experiments

The tilting, recirculating flume has a test section 5.0 m long, 0.30 m wide, and 0.70 m deep (Figure 3.1). The sediment section contains well-sorted quartz-feldspar granules ($d_{10} = 1.9$ mm, $d_{50} = 2.4$ mm, $d_{90} = 3.0$ mm), with an approximate porosity of 0.40. To represent a channel-spanning log, a 4.0-inch PVC pipe (outer diameter of 11.4 cm) was cut to flume width and mounted 4 cm above the bed. Channel slope was 0.12° (0.002 m/m), appropriate for a forested lowland stream. Two experiments were conducted: in Trial 1, flow was subcritical, mean channel velocity was 14 cm/s, and flow depth was 20 cm; in Trial 2, flow was supercritical near the log (but incoming flow was subcritical), mean channel velocity was 12.5 cm/s, and flow depth was 17 cm.

Respective blockage ratios (fraction of channel flow depth blocked by log) were 0.58 and 0.67. In Trial 2, grains beneath the log were near the threshold for mobilization.

We collected three datasets to characterize hyporheic exchange within the experimental section. Time-averaged pressures were measured along the sediment-water interface at eight locations using Validyne DP15 transducers (observed accuracy of ± 0.260 mm water). Flow paths in sediment were also mapped from dye injection. Finally, conservative solute tracer tests were performed by injecting calcium chloride (CaCl_2) solution into the surface water over approximately one recirculation period and monitoring surface water electrical conductivity as a proxy for salt concentration. Because the flume is a closed system and the tracer is conservative, decline in salt concentration over time indicates exchange between labeled surface water and unlabeled pore water. For both tracer tests, initial concentrations were approximately equal and small (< 1 ppt), limiting the effect of density on exchange [Boano *et al.*, 2009].

To explore the impact of scour topography on hyporheic exchange, I approximately doubled the flow rate after Trial 2 to induce scour. The topography approached a steady state within several hours. I mapped the resulting bed profile and included it in a subset of numerical simulations.

3.3.2. Numerical modeling

Coupled channel and hyporheic flow was simulated following the computational fluid dynamics (CFD) approach of *Cardenas and Wilson* [2007a]: turbulent flow in the channel was linked to porous media flow in the sediment through the pressure distribution at the sediment-water interface (see Figure 2 of *Cardenas and Wilson* [2007a]). Here, I include a free surface in turbulent flow simulations, since the water surface deforms near channel-spanning logs. In contrast, *Cardenas and Wilson* [2007a] represented the free surface as a slip (symmetry) boundary.

We solve for two-dimensional, unsteady, turbulent, multi-phase flow of water and overlying air in the channel using the Reynolds-averaged Navier-Stokes (RANS) equations with the k - ω closure scheme [Wilcox, 1998] (Figure 3.2). Liang and Cheng [2005] demonstrated the superior performance of the k - ω turbulence closure scheme for flow around a cylinder near a plane boundary. For an incompressible flow:

$$\frac{\partial \rho U_i}{\partial x_i} = 0, \text{ and} \quad (3.1)$$

$$\rho \frac{\partial U_i}{\partial t} + \frac{\partial \rho U_i U_j}{\partial x_j} = -\frac{\partial P}{\partial x_i} + \frac{\partial}{\partial x_j} (2\mu S_{ij} - \overline{\rho u'_j u'_i}), \quad (3.2)$$

where ρ and μ are fluid density and dynamic viscosity, t is time, U_i and u'_i are time-averaged and instantaneous velocity components in x_i directions, and P is time-averaged pressure. S_{ij} is the mean strain-rate tensor:

$$S_{ij} = \frac{1}{2} \left(\frac{\partial U_i}{\partial x_j} + \frac{\partial U_j}{\partial x_i} \right). \quad (3.3a)$$

Reynolds stresses are related to turbulent kinetic energy (k) and specific dissipation rate (ω) by:

$$\tau_{ij} = -\overline{u'_j u'_i} = 2S_{ij} \nu_t - \frac{2}{3} \delta_{ij} k, \quad (3.3b)$$

where δ_{ij} is the Kronecker delta, and ν_t is the kinematic eddy viscosity (equivalent to k/ω). The transport equations for k and ω are:

$$\rho \frac{\partial k}{\partial t} + \frac{\partial (\rho U_j k)}{\partial x_j} = \rho \tau_{ij} \frac{\partial U_i}{\partial x_j} - \beta^* \rho \omega k + \frac{\partial}{\partial x_j} \left[(\mu + \mu_t \sigma_k) \frac{\partial k}{\partial x_j} \right], \text{ and} \quad (3.4)$$

$$\rho \frac{\partial \omega}{\partial t} + \frac{\partial (\rho U_j \omega)}{\partial x_j} = \alpha \frac{\rho \omega}{k} \tau_{ij} \frac{\partial U_i}{\partial x_j} - \beta \rho \omega^2 + \frac{\partial}{\partial x_j} \left[(\mu + \mu_t \sigma_\omega) \frac{\partial \omega}{\partial x_j} \right]. \quad (3.5)$$

β^* is given by:

$$\beta^* = \beta_0^* f_{\beta^*}, \text{ where} \quad (3.6a)$$

$$f_{\beta^*} = \frac{1 + 680 \chi_k^2}{1 + 400 \chi_k^2} \text{ for } \chi_k > 0 \text{ and } 1 \text{ for } \chi_k \leq 0. \quad (3.6b)$$

χ_k is defined as:

$$\chi_k = \frac{1}{\omega^3} \frac{\partial k}{\partial x_j} \frac{\partial \omega}{\partial x_j}. \quad (3.6c)$$

Closure coefficients are the standard values: $\alpha = 13/25$, $\beta = 9/125$, $\beta_0^* = 9/100$, and $\sigma_k = \sigma_\omega = 0.5$. Note that unlike in *Cardenas and Wilson [2007]*, I solve for the unsteady flow field using the unsteady RANS (URANS) approach, which improves numerical stability for two-phase flow. I then time-average the pressure at the sediment-water interface.

The sediment-water interface and log were assigned no-slip boundaries with roughness heights of 3 mm (d_{90}) and 0.010 mm (roughness height for PVC), respectively. The upstream boundary was assigned a fully developed turbulent velocity profile, and the downstream boundary was assigned a hydrostatic pressure profile. Air boundaries were constant pressure outlets. Simulations were run until mean pressure stabilized along the bed.

Two-dimensional porous flow in sediment was solved using the steady-state groundwater flow equation:

$$\frac{\partial}{\partial x_i} \left(-\frac{k\rho g}{\mu} \frac{\partial P}{\partial x_i} \right) = 0, \quad (3.7)$$

where P is pressure, k is sediment permeability, μ is fluid viscosity, and ρ is fluid density. Darcy velocity or groundwater flux, q , equals the term in brackets. Pressure at the sediment-water interface was specified from turbulent open-channel flow simulation. The base and sides of the porous flow domain (flume walls) were assigned no-flow boundaries. In all simulations, the sediment was homogeneous and isotropic.

Tracer experiments were simulated and analyzed following *Ren and Packman [2004]*. To determine the residence time distribution, I solved for transient solute transport in the flume using the advection-diffusion-dispersion equation:

$$\frac{\partial C}{\partial t} = -\frac{\partial v_i C}{\partial x_i} + \frac{\partial}{\partial x_i} \left(D_{ij} \frac{\partial C}{\partial x_i} \right), \quad (3.8)$$

where C is concentration, t is time, and v is seepage velocity (specific discharge divided by porosity) from pore water flow simulations. D_{ij} is the mechanical dispersion tensor:

$$D_{ij} = \alpha_T |v| \delta_{ij} + (\alpha_L - \alpha_T) \frac{v_j v_i}{|v|} + D_m' \delta_{ij}, \quad (3.9)$$

where α_T and α_L are transverse and longitudinal dispersivities and D_m' is the molecular diffusion coefficient in porous media. In simulations of Trials 1 and 2, the porosity was 0.40, and the permeability was $8.5 \times 10^{-9} \text{ m}^2$. D_m' was $5 \times 10^{-11} \text{ m}^2/\text{s}$, α_L was 1 cm (several grain diameters), and α_T was 1/10 of α_L . At the top boundary (sediment-water interface), downwelling zones were assigned constant normalized concentration (C/C_0) of 1.0, and upwelling zones were specified as convective flux boundaries. Flume walls were assigned zero-flux boundaries. Initial solute concentration in the sediment was zero.

URANS equations were solved using the finite-volume approach implemented in FLUENT [*Fluent Inc.*, 2006] with a fully implicit second-order upwind solution scheme. Multiphase flow was treated with the volume of fluid approach [*Hirt and Nichols*, 1981]. The domain consisted of more than 120,000 cells, and simulations were checked for grid and boundary dependence. Finer grid spacing was used near the air-water interface, log surface, and channel bottom. The location of the upstream and downstream boundaries slightly affected the magnitude of head drop over the cylinder (within $\pm 0.5 \text{ mm}$, similar to the error of pressure transducers) but had negligible impact on the downstream head recovery. Groundwater flow and solute transport equations were solved using the finite-element approach in COMSOL Multiphysics [*COMSOL AB*, 2006]. The sediment domain consisted of more than 18,000 triangular elements with node spacing of less than 1 cm at the top and less than 2 cm at the base. Simulations were tested for mesh dependence.

3.3.3. Sensitivity study

We developed an approximate relationship for pressure along the bed due to flow around a channel-spanning log using an expanded set of 27 flume experiments and 50 CFD simulations. From dimensional analysis, controlling variables are the channel Froude number (Fr) with mean channel depth (d) as the length scale, gap ratio (G , the ratio of log height above the bed to channel depth), and blockage ratio (B , the ratio of log diameter D to channel depth) (Figure 3.1). Flume experiments and CFD simulations together span a range of blockage ratios from 0.33 to 0.67, gap ratios from 0.086 to 0.56, and Froude numbers from 0.026 to 0.23. Flume experiments were performed using three diameters of PVC pipe (8.89, 11.43, and 14.13 cm). Due to the large size of the flume, I did not scale experiments, which precluded larger Froude numbers.

Equations were fitted to pressure along the bed from CFD simulations using a nonlinear least squares method. Measured pressures from flume experiments were only analyzed for magnitudes of pressure drop and recovery near LWD (spatial resolution was insufficient to fit all parameters describing the pressure profile). Fitted parameters were then correlated with Fr , B , and G to link pressure along the bed with LWD configuration and channel hydraulics.

To assess the impact of Fr , B , and G on mean hyporheic flow rates, I simulated hyporheic flow over a 10-m section of stream centered on a single log. Pressure along the bed was constrained from the piecewise function in 66 cases (with no slope adjustment for stream gradient) and CFD simulations in 12 cases, for comparison. Mean flux across the bed was computed as the integral of absolute Darcy flux into the bed divided by total streambed length.

3.4. RESULTS

3.4.1. Two case studies of hyporheic exchange near a channel-spanning log

In Trials 1 and 2, surface water accelerates around the log—maximum velocities approach 40 cm/s and 50 cm/s, respectively (Figure 3.2). The free surface deforms towards the log, and a series of standing waves form in Trial 2 (Figure 3.2). Numerical simulations show vortex shedding for Trial 1, whereas shedding is suppressed for Trial 2. Both trials were conducted near the threshold for vortex suppression identified by *Bearman and Zdravkovich* [1978] in wind tunnel experiments (gap:diameter ratio ~ 0.3).

Head along the bed generally mimics the free surface elevation but lacks wavelengths much less than the flow depth (Figure 3.2). The maximum head drop is 7 mm in Trial 1 and 10 mm in Trial 2. The minimum occurs beneath the log's downstream edge, as in *Bearman and Zdravkovich* [1978]. Head gradually recovers with distance downstream and approaches a value 4 mm and 6 mm less than upstream head in Trials 1 and 2, respectively (Figure 3.2). Simulated and measured head values are in good agreement.

Head gradients along the bed cause water to downwell upstream of the log and upwell downstream. Fastest fluxes occur beneath the log and decay rapidly with distance upstream and downstream (Figure 3.2). The spatial extent of hyporheic exchange is limited only by the flume walls (Figure 3.3). In simulations for Trial 1, the maximum downwelling rate is 3.1 mm/s and occurs less than 1 cm upstream of the log's leading edge. The maximum upwelling rate is 5.7 mm/s and occurs 5 mm downstream of the log center. The average flow rate across the sediment-water interface is 1.2×10^{-4} m/s. In Trial 2, simulated fluxes are greater: the maximum downwelling rate is 4.6 mm/s and occurs less than 5 mm upstream of the log's leading edge. The maximum upwelling rate is 8.3 mm/s and occurs 5 mm downstream of the log center (Figure 3.3). The average

flow rate across the sediment-water interface is 1.8×10^{-4} m/s (50% greater than Trial 1). I also compare pore water flow fields using the flushing intensity, q_f , after *Zlotnik et al.* [2011]. The flushing intensity is the horizontally-averaged Darcy flux (q) calculated at incremental depths. Flushing intensity is greatest near the sediment-water interface and declines exponentially with depth (Figure 3.3).

In general, individual flow paths from simulations agree with observations (Figure 3.2). In simulations for Trial 1, upwelling flow paths converge strongly near the log, curving back upstream in some cases. A small, shallow hyporheic exchange cell overlies upstream-deflected flow paths. If this zone existed in the flume, it probably occurred farther downstream, since upwelling dye streaks near the log did not curve strongly upstream (Figure 3.2). In models, the existence or location of this shallow secondary cell is sensitive to pressure gradients downstream of the log. Because the size of this cell and exchange rates within it are small, the cell should not significantly impact solute or heat transport within the sediment. In Trial 2, simulated flow paths closely match dye streaks (Figure 3.2). No secondary hyporheic exchange cell occurs, presumably because pressure recovery along the bed is more gradual.

Simulated particle travel times are 80% faster than dye travel times, on average. In Trial 1, starting at the upper right injection port and moving clockwise, approximate travel times for each dye path are 15 s, 510 s, 240 s, and 30 s (± 15 s). Simulated times are 19 s, 258 s, 133 s, and 16 s. In Trial 2, approximate travel times for each dye path were 30 s, 360 s, 180 s, and 15 s (± 15 s), compared with simulated times of 14 s, 159 s, 98 s, and 11 s. One source of error may be the model permeability, determined from fitting models with tracer data. Permeability estimated from a constant head test on a column of repacked flume sediment was ~ 2.5 times less than the permeability from tracer tests. Actual permeability probably lies between these two estimates. Another potential

source of error is the flume wall, which may have slowed the flow of pore water and dye. The good agreement between measured and simulated pressure along the bed suggests that the pressure boundary condition is not a significant source of error.

While dye injections reveal travel times for individual flow paths, a tracer test samples the integrated effect of all hyporheic flow paths. In Trial 1, tracer concentration in surface water approaches a constant value after approximately 30 hours, indicating nearly complete mixing between surface water and pore water (Figure 3.4). Measured concentrations agree well with simulated concentrations, which are based on the residence time distribution from the porous flow model. The longest residence times are on the order of one day. In Trial 2, surface water concentration declines more rapidly and approaches a constant value after approximately 20 hours. Simulated concentrations agree well with measured concentrations at early times but decline more slowly at late times, suggesting that the simulated residence time distribution over-emphasizes longer residence times. Slight scouring occurred over the course of the tracer experiment, which may partly explain discrepancies between simulated and measured concentrations.

3.4.2. Influence of scour topography

The flow of river water around LWD preferentially erodes and deposits sediment. This scour morphology also drives hyporheic exchange. Here, I compare hyporheic exchange under three scenarios: LWD with plane bed, LWD with scoured bed, and scoured bed without LWD. These three simulations could represent the evolution of hyporheic exchange near a channel-spanning log after initial tree fall, scour development, and log removal or decomposition. Bed topography consists of a scoured zone with maximum depth of 2.6 cm and bar form with height of 5.6 cm located approximately 60 cm downstream of the log.

Scour topography locally increases flow depth and decreases blockage ratio. As a result, the total head drop across the log decreases (Figure 3.5). As in the planar bed case, head recovers approximately 1 meter downstream, but a local head maxima occurs on the upper stoss face of the bar, and a local minima occurs at the base of the lee face. Large-scale hyporheic exchange patterns are similar to the plane bed case, but smaller exchange cells are superimposed near the bar. These small exchange cells slightly increase hyporheic flushing rates within the top few centimeters of sediment, but flushing rates at depth are smaller for the scoured bed because of the reduction in total head drop, which drives longer flow paths. River water generally downwells in three locations: upstream of the log, near the crest of the bar form, and downstream of the bar form. Maximum upwelling occurs immediately downstream of the log and at the base of the bar's lee face.

In the absence of LWD, scour topography produces a much smaller head drop. Undulations in head along the bed cause water to downwell into the trough and stoss face and upwell immediately downstream of the lee face. Total flux across the bed and hyporheic flushing at all depths are greatly reduced. An important implication is that although scour morphology measurably impacts hyporheic exchange, LWD creates the predominant head drop that drives most of the exchange. Additionally, hyporheic exchange is not linearly additive—fluxes due to LWD and scoured bed are less than the sum of individual fluxes. The non-linear behavior is due to the non-linearity of turbulent flow that produces head gradients along the bed.

3.4.3. A semi-empirical model for head profile along the bed

Head measurements from flume experiments all include a large drop of magnitude h_1 along the bed beneath the log (Figure 3.6). Head partially recovers by magnitude h_2 downstream. In Appendix A1, I heuristically show that the maximum head

drop (h_1) should scale with blockage ratio and channel Froude number. Height of the log above the bed (or gap ratio) should not impact the head drop. Here, I support this argument with pressure measurements and additional CFD simulations. I then develop a simple equation for head along the bed due to flow around a channel-spanning log.

Measured and simulated head drop normalized by d increases with Fr and B but shows no dependence on G (Figure 3.7a-c). Since h_1/d is related to both Fr and B via power-laws (Figures 3.7a and 3.7b), its dependence on both parameters can be combined into one power-law. Regression leads to the relationship (Figure 3.7d):

$$\frac{h_1}{d} = 18.5Fr^{2.1}B^{2.8}. \quad (3.10)$$

Head recovery (h_2) scales similarly with Fr and B (Figure 3.7e):

$$\frac{h_2}{d} = 10.5Fr^{2.1}B^{2.8}. \quad (3.11)$$

Log-normal distributions were chosen to represent the rising and falling limbs of the bed pressure profile. These functions match the observed asymmetry in pressure drop and recovery and require only two parameters (first and second moments, Figure 3.6). Note, however, that log-normal distributions are used here with no statistical meaning; they are simply convenient. In total, five parameters were fitted for each pressure profile, in addition to the magnitudes of pressure drop and recovery: location of the pressure minimum with respect to log center (x_0), expectation and spread of the falling limb (μ_1 and σ_1), and expectation and spread of the rising limb (μ_2 and σ_2).

Based on individual correlations, B and G control x_0 and the moments of pressure drop and recovery, normalized by log diameter (Figure 3.8). Specifically, the pressure minimum shifts further downstream as B decreases and G increases (Figure 3.8a):

$$\frac{x_0}{D} = 0.26B^{-2.2}G^{1.1}. \quad (3.12)$$

Similarly, the first and second moments for the pressure drop decrease with B and increase with G (Figure 3.8b-c):

$$\frac{\mu_1}{D} = 0.34B^{-2.2}G^{1.1} + 0.27, \text{ and} \quad (3.13)$$

$$\frac{\sigma_1}{D} = 0.20B^{-2.2}G^{1.1} + 0.16. \quad (3.14)$$

The first and second moments of pressure recovery are best correlated with G (Figure 3.8d-e):

$$\frac{\mu_2}{D} = 29G^2 - 17G + 3.8, \text{ and} \quad (3.15)$$

$$\frac{\sigma_2}{D} = 55G^2 - 34G + 5.8. \quad (3.16)$$

The correlations are relatively weak, however, suggesting complex behavior in the pressure recovery downstream of LWD. In natural settings, scour topography will further complicate the pressure recovery (Figure 3.5).

Finally, head h along the bed can be approximated as:

$$x < x_0 : h(x) = \frac{h_1}{2} \left[1 + \operatorname{erf} \left(\frac{\ln(x_0 - x) - k_1}{\sqrt{2s_1^2}} \right) \right], \text{ and} \quad (3.17a)$$

$$x > x_0 : h(x) = \frac{h_2}{2} \left[1 + \operatorname{erf} \left(\frac{\ln(x - x_0) - k_2}{\sqrt{2s_2^2}} \right) \right], \quad (3.17b)$$

where:

$$k = \ln \left(\frac{\mu^2}{\sqrt{\sigma^2 + \mu^2}} \right), \text{ and} \quad (3.17c)$$

$$s = \sqrt{\ln \left[\left(\frac{\sigma}{\mu} \right)^2 + 1 \right]}. \quad (3.17d)$$

Equations 3.10-3.17 constrain head along the bed for simulating hyporheic exchange and solute or heat transport near LWD, eliminating the need for tedious CFD simulations in

many cases. These equations do not include the stream gradient, but a slope adjustment could be added to account for other sources of flow resistance.

3.4.4. Hyporheic exchange from LWD geometry and flow parameters

Hyporheic exchange rates increase with Froude number and blockage ratio:

$$q^* = 0.28Fr^{2.0} B^{2.8}, \quad (3.18)$$

where q^* is the mean flux across the sediment-water interface normalized by sediment hydraulic conductivity (Figure 3.9). An important point is that hydraulic conductivity can vary by orders of magnitude in riverbed sediment, while B and Fr have limited ranges. Sediment permeability therefore exerts the greatest control on hyporheic exchange due to LWD. Gap ratio does not significantly impact mean hyporheic exchange rate (correlation between G and q^* is statistically insignificant). Although the gap ratio can influence spatial distributions of flux across the bed, maximum downward and upward fluxes occur closest to the log (Figures 3.2 and 3.3).

3.5. DISCUSSION

Hyporheic exchange due to LWD increases with blockage ratio and Froude number. This scaling is fundamentally similar to relationships determined for planar and rippled beds, where exchange increases with the shear Reynolds number and permeability Péclet number [O'Connor and Harvey, 2008]. In this study, shear velocity was not apparent or intuitive for open-channel flow around a single log, and Froude number was a logical choice for scaling (see Appendix A1). In general, shear Reynolds number should correlate with Froude number at the reach scale.

Depending on blockage ratio and Froude number, LWD in natural densities can drive reach-averaged hyporheic exchange rates similar to rippled bed topography. As an example, hyporheic exchange rates averaged over the 5-m flume in Trial 2 are slightly

greater than rates due to bedforms under the same flow conditions (Figure 3.2). Mean flux is 1.32×10^{-4} m/s for bedforms and 1.87×10^{-4} m/s for the single log, which can be considered a reasonable approximation for the reach-averaged flux in a lowland stream with log spacing of 5 m. This spacing is well within the reported range for natural lowland streams in Central Europe (defined using log diameter > 0.10 m) [Hering *et al.*, 2000]. Notably, exchange beneath logs is much deeper than beneath ripples. Two hours after introduction of conservative tracer to surface water, the sampled hyporheic zone area is 1.9 m^2 for the log and only 0.074 m^2 for bedforms (defined by the area where $C/C_0 > 0.1$). The implication is that LWD and ripples can drive similar reach-averaged hyporheic exchange rates, but the length scales and residence times of LWD-induced hyporheic exchange are greater. Where LWD exists, it is a key driver of hyporheic mixing at the scale of meters.

My analysis is restricted to simple LWD configurations. Specifically, I did not consider partially buried logs but only suspended logs that span the entire channel at orientations normal to the flow direction. In small streams, wood is predominantly aligned across channels [Gurnell *et al.*, 2002]. In larger rivers, log orientations are more variable, but a significant proportion of logs (37% in one fourth-order river) still extend across most of the channel [Gurnell *et al.*, 2002]. I anticipate that hyporheic exchange should increase with Froude number and blockage ratio for more complex LWD morphologies.

My analysis is also restricted to shallow flows or large blockage ratios, where the free surface controls pressure along the bed. As blockage ratio decreases, the contribution of drag to the pressure field will dominate the contribution from the free surface. In this case, gap ratio (or the vertical position of LWD within the flow) will impact hyporheic exchange rates. The Reynolds number may also impact exchange rates

for small blockage ratios. Without further testing, the scaling relationships herein should only be used for similar blockage ratios and Reynolds numbers.

Another limitation of this study is the artificial flow boundary created by flume walls and included in numerical models. In natural streams, competing interactions between LWD and other geomorphic features will determine the spatial extent of the hyporheic zone. In simulations, the hyporheic zone fills the domain, regardless of boundary position or conditions, because the single channel-spanning log is the only source of exchange. Domain size also impacts mean hyporheic flux estimates (Figure 3.9, Equation 3.18). I selected a domain size for these simulations (10 m long and 2 m deep) to minimize the influence of boundary conditions on hyporheic exchange patterns while maintaining a reasonable representative elementary volume for examining the effects of a single channel-spanning log. At the upstream and downstream boundary locations, hyporheic flow rates are orders of magnitude lower than in the vicinity of the log, so these boundaries do not significantly affect exchange near the log. However, because domain-averaged exchange rates are dependent on domain size, Equation 3.18 cannot be used to predict average hyporheic exchange rates in reaches with LWD. Instead, Equations 3.10-3.17 can be used to predict head along the bed and to simulate hyporheic flow. In this case, the effect of multiple log interactions on pressure along the bed should be small for spacings less than 10 diameters [Ranga Raju *et al.*, 1983].

3.6. CONCLUSIONS

LWD drives significant hyporheic mixing at the meter-scale characterized by downwelling upstream and upwelling downstream. Exchange rates are fastest near LWD and decay exponentially with depth and distance upstream or downstream. Exchange increases with blockage ratio and Froude number and is relatively insensitive to vertical location of LWD in the channel. To my knowledge, this study is the first to analyze the

mechanics of hyporheic exchange due to in-stream flow obstacles suspended within the channel and to show that exchange generally increases with obstacle size and channel Froude number.

Under natural LWD densities, reach-averaged hyporheic exchange rates due to LWD and ripples are similar for typical lowland stream conditions. However, hyporheic exchange due to LWD has longer path lengths and residence times. My findings suggest that in modern streams depleted in LWD, rates of river-groundwater exchange may be severely reduced (especially in straightened channels with relatively simple morphologies). LWD reintroduction is a promising tool for restoring hydrologic connectivity. my model for bed pressure profiles and hyporheic exchange rates in the vicinity of LWD can be used to inform the design of LWD reintroduction and restoration projects.

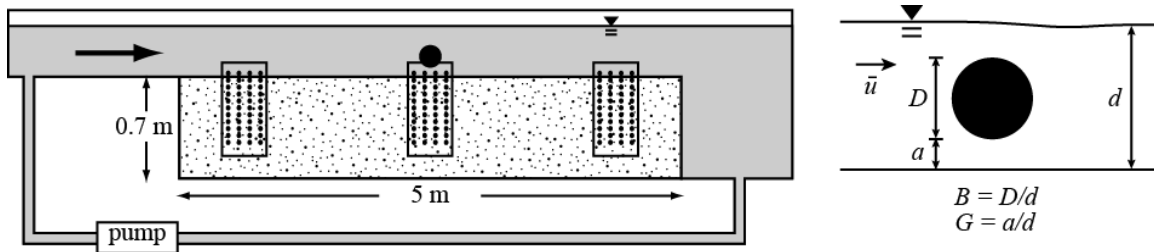


Figure 3.1: Flume (left) and experimental variables (right). Injection port locations, shown schematically, consist of three panels with four columns of ports. Key experimental parameters include blockage ratio (B), gap ratio (G), and channel Froude number.

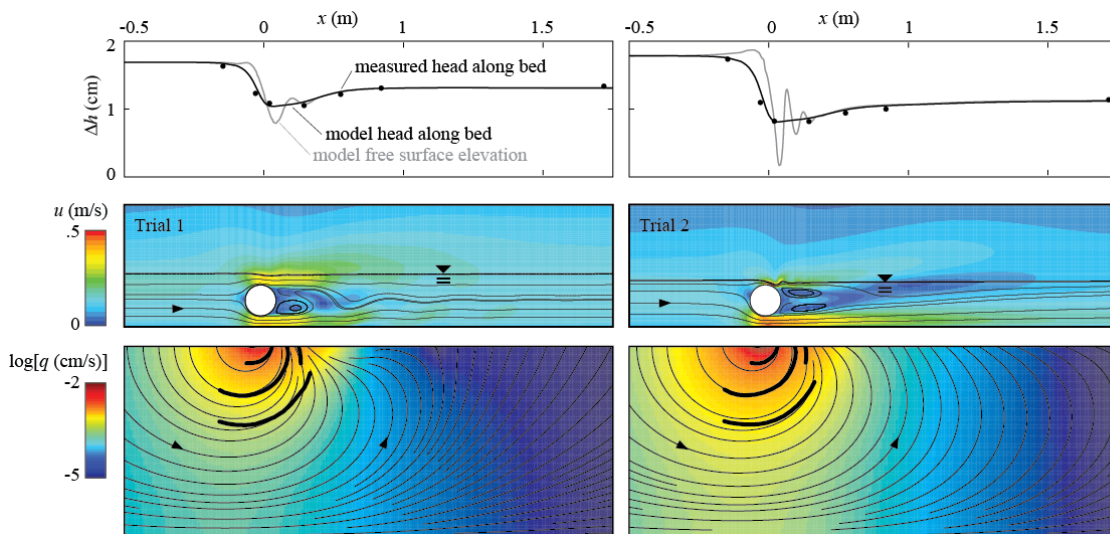


Figure 3.2: Simulated surface water and pore water flow near wood debris in Trial 1 (left) and Trial 2 (right). Channel flow is left to right. Thin black lines indicate streamlines. Thick black lines in sediment indicate mapped dye streaks. Top plot compares measured and simulated head along the bed with simulated elevation of the free surface. Error for pressure measurements is ± 0.26 mm.

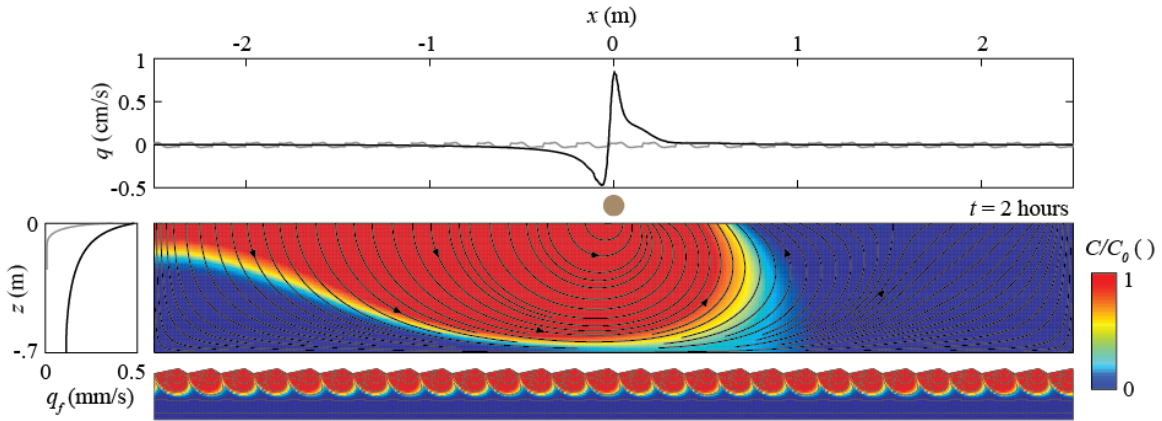


Figure 3.3: Hyporheic exchange fills entire flume and drives patterns of conservative solute tracer concentration within sediment. Flow in surface water (not shown) is left to right. Black streamlines indicate simulated hyporheic exchange for Trial 2. Colors indicate simulated concentration of conservative tracer (C/C_0) two hours after introduction to surface water. Below: comparison of hyporheic exchange and solute concentration for ripples with wavelength of 18 cm and height of 2.7 cm under same channel flow conditions. Top: comparison of specific discharge (q) across the bed for Trial 2 (black line) and bedforms (gray line). Left: comparison of flushing rate (q_f) versus depth for Trial 2 and bedforms.

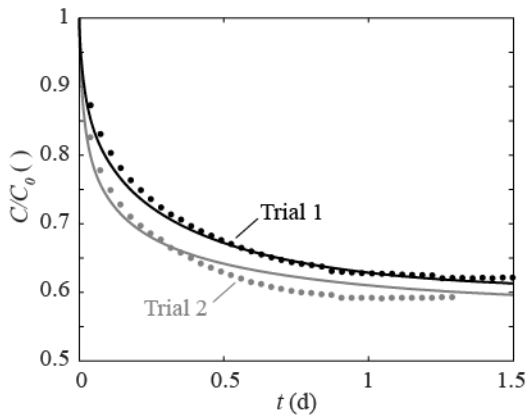


Figure 3.4: Tracer experiments. Measured (dots) and modeled (line) solute concentration in surface water from tracer tests for Trials 1 and 2.

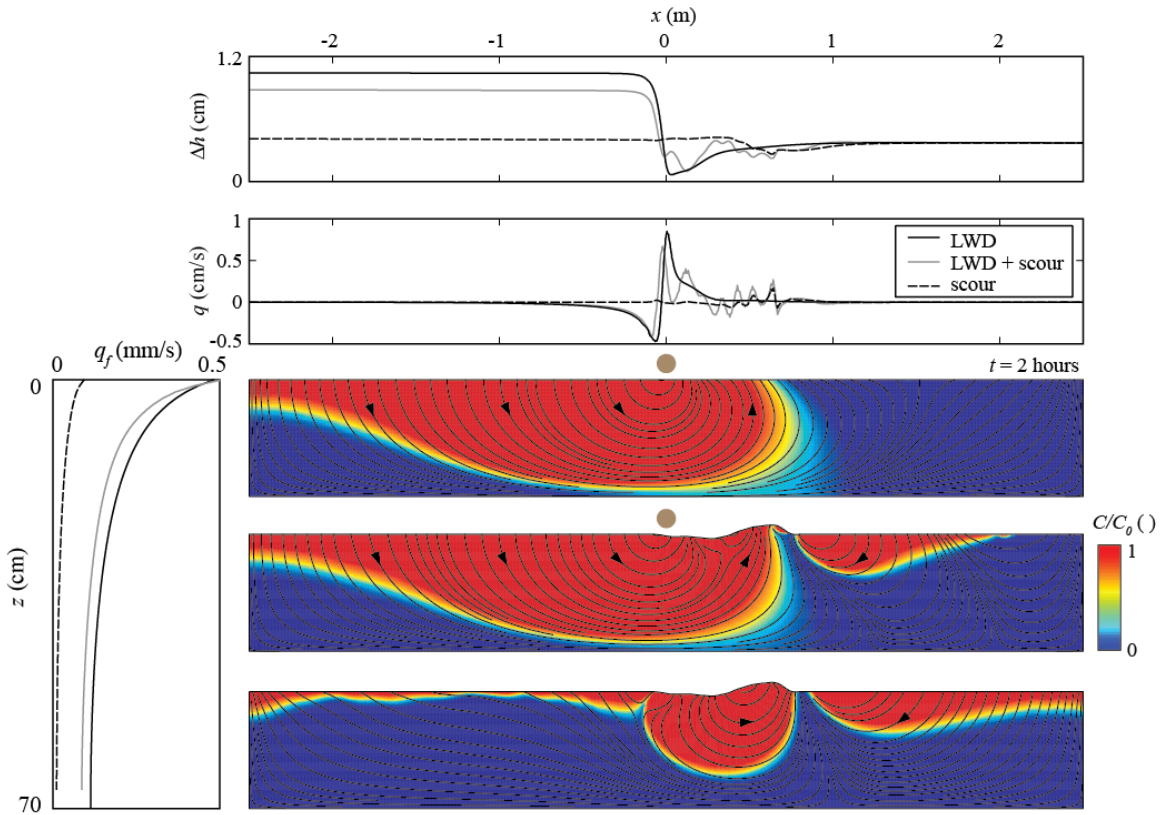


Figure 3.5: Modeled hyporheic exchange and conservative solute transport after 2 hours for LWD with plane bed, LWD with scour topography, and scour topography only. LWD and channel flow parameters are for Trial 2. Top: head (h) and specific discharge (q) across the bed versus distance downstream. Left: flushing rate (q_f) versus depth.

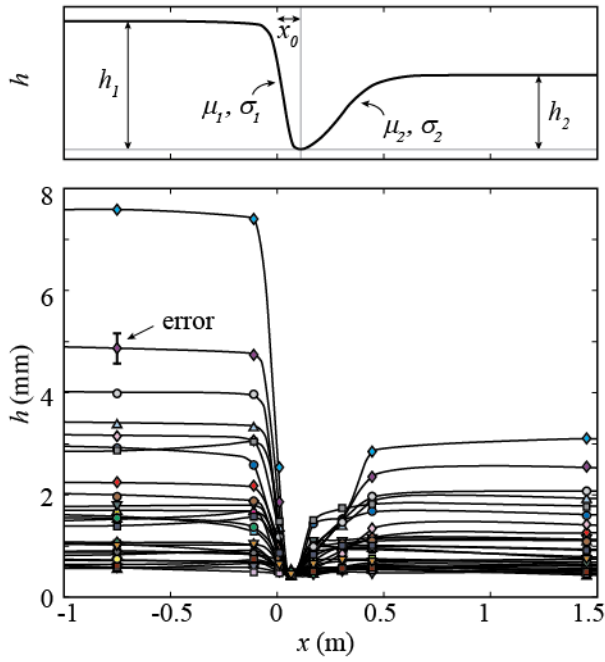


Figure 3.6: Measured head (h) along the sediment-water interface for 27 flume experiments. LWD was centered at $x = 0$. All head profiles are vertically shifted so that minima coincide. Top plot shows functional form (two log-normal distributions) and fitting parameters.

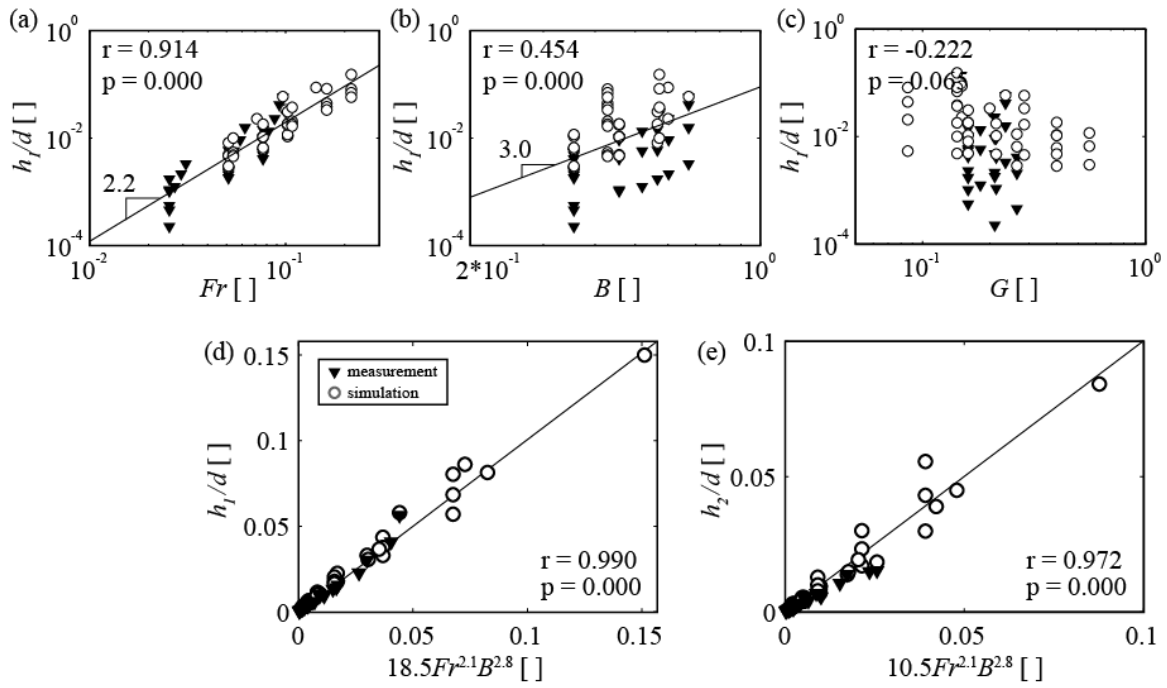


Figure 3.7: Scaling relationships between dimensionless maximum head drop (h_1/d) and (a) Froude number (Fr), (b) blockage ratio (B), and (c) gap ratio (G). Dimensionless maximum head drop scales with Fr and B (d), as does dimensionless head recovery (e).

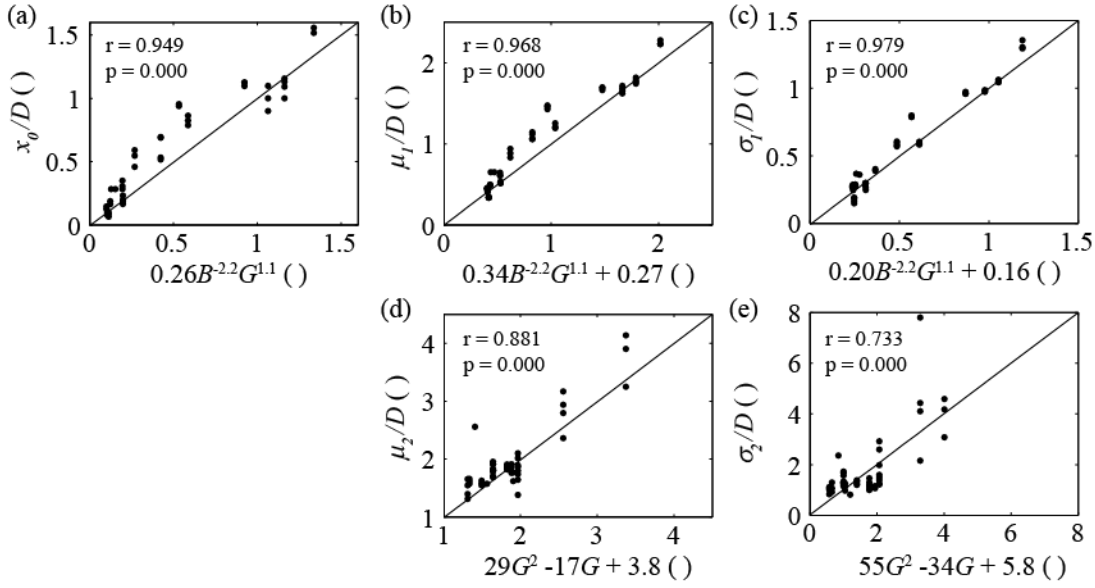


Figure 3.8: Scaling relationships for pressure along bed. (a) Dimensionless location of pressure minimum (x_0/D) correlates with blockage ratio (B) and gap ratio (G). (b) Dimensionless expectation (μ_1) of falling pressure limb (location of 50% decline) correlates with B and G . (c) Dimensionless spread (σ_1) of falling pressure limb correlates with B and G . (d) Dimensionless expectation (μ_2) of rising pressure limb (location of 50% increase) correlates only with G . (e) Dimensionless spread (σ_2) of rising pressure limb correlates only with G .

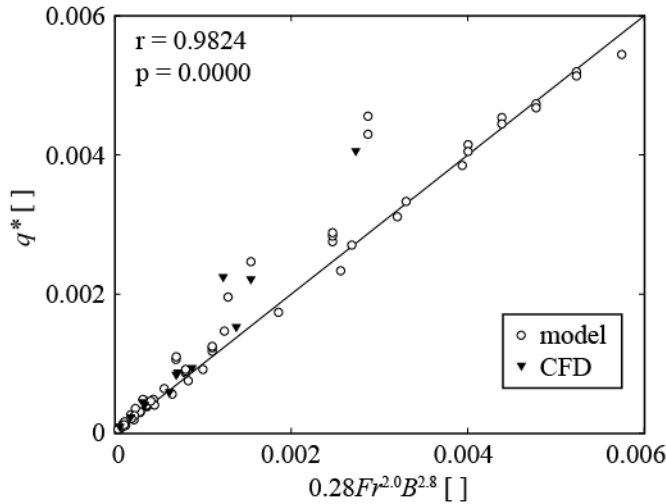


Figure 3.9: Dimensionless mean hyporheic flux (q^*) increases with blockage ratio (B) and Froude number (Fr) but does not depend strongly on gap ratio (G). Mean hyporheic flux was computed using head profiles from Equations 3.10-3.17 (white circles) and CFD simulations (black triangles).

Chapter 4: Thermal dynamics in hyporheic zones formed by large woody debris

4.1. ABSTRACT

The flow of river water around large woody debris (LWD) creates pressure gradients along the bed that drive river-groundwater mixing, or hyporheic exchange, and advective heat transport within the hyporheic zone. I quantify hyporheic exchange and heat transport induced by channel-spanning logs using two approaches: laboratory flume experiments and numerical experiments that link turbulent open-channel and groundwater flow. Flume and numerical experiments show that LWD produces a characteristic diel temperature pattern within sediment. Upstream from LWD, downwelling water transports the river's diel thermal signal deep into the sediment. Downstream, upwelling water forms a wedge of buffered (low-amplitude) temperatures. These temperature patterns shift in response to LWD blockage ratio (fraction of the channel depth blocked by wood debris), channel Froude number, and sediment permeability. However, hyporheic heat exchange associated with LWD does not significantly impact diel surface water temperatures. Diel temperature signals of upwelling water are similar to river temperatures because the majority of hyporheic water emerges from short, fast hyporheic flow paths. Due to historic channel clearing practices, modern rivers have unnaturally low densities of LWD. A key implication is that LWD removal has contributed to thermal homogenization and degradation of benthic and hyporheic habitats. LWD reintroduction is a promising strategy for improving vertical connectivity in rivers and increasing thermal patchiness within the hyporheic zone.

4.2. INTRODUCTION

Large woody debris (LWD) is a key morphologic element in rivers that improves habitat quality for invertebrates and fish, but LWD density is unnaturally low in modern, cleared rivers [Abbe and Montgomery, 1996]. LWD increases biofilm and periphyton production [Johnson *et al.*, 2003] as well as the abundance and diversity of macroinvertebrates [Smock *et al.*, 1989; Wallace, 1997] and fish [Angermeier and Karr, 1984; Roni and Quinn, 2001; Wright and Flecker, 2004]. The biophysical factors that link LWD with ecological processes are numerous. LWD controls substrate type and grain size and forces complex pool morphology [Lisle, 1995; Montgomery *et al.*, 1996]. LWD is also a major source of energy and organic matter in streams [Bilby and Likens, 1980; Smock *et al.*, 1989; Webster and Meyer, 1997]. Finally, LWD promotes hyporheic exchange [Lautz *et al.*, 2006; Mutz *et al.*, 2007; Sawyer *et al.*, in review], which influences patterns of nutrients [Stanford and Ward, 1988; Zarnetske *et al.*, in press], organic carbon [Findlay, 1995], and temperature [Arrigoni *et al.*, 2008; Brunke and Gonser, 1997] within hyporheic, benthic, and epigeic aquatic habitats.

In particular, temperature is a critical ecological parameter [Brown *et al.*, 2004]. Within benthic and hyporheic zones, temperature regulates microbial activity, invertebrate development, and salmonid embryo survival [Brunke and Gonser, 1997]. Within the channel, temperature can control spawning site selection [Baxter and Hauer, 2000] and competitive behavior [Destaso and Rahel, 1994; Magnuson *et al.*, 1979]. Because aquatic fauna have specific temperature ranges, aquatic communities are sensitive to thermal perturbation due to climate change and anthropogenic thermal degradation [Poole and Berman, 2001].

Several field studies have linked thermal patterns in aquatic environments with hyporheic exchange processes. Hyporheic exchange invariably drives thermal patterns

within the riverbed and banks, but implications for surface water temperatures vary widely among studies. Hyporheic exchange beneath riffles [Storey *et al.*, 2003; Swanson and Cardenas, 2010], bedforms [Cardenas and Wilson, 2007b; d], and weirs [Hester *et al.*, 2009] leads to strong thermal heterogeneity within riverbed sediment. Of these studies, only Hester and Doyle [2009] examined whether hyporheic heat advection also influenced surface water temperature. They showed that weir addition caused thermal shifts up to 1.0°C within the hyporheic zone and adjacent stream but that atmospheric heating rather than hyporheic advection caused thermal shifts within the surface water. Additional field studies over larger scales (hundreds of meters) have demonstrated that river-groundwater connectivity can control surface water temperatures in anabranching and braided channels [Arrigoni *et al.*, 2008; Arscott *et al.*, 2001].

Here, I quantify heat advection and thermal dynamics within hyporheic zones formed by LWD for the specific case of submerged, channel-spanning logs. Hyporheic exchange significantly changes diel temperature within the hyporheic zone but not the channel. I first present descriptions of hyporheic thermal patterns from novel flume experiments that span a range of log sizes and channel Froude numbers. I then use numerical models of hyporheic fluid and heat exchange to explain the observed thermal patterns. Numerical models clarify the role of sediment permeability, channel Froude number, and blockage ratio (the fraction of channel depth blocked by LWD) in controlling thermal zonation and advective heat transport within the sediment. Ultimately, modern LWD removal practices contribute to thermal homogenization of benthic and hyporheic habitats. My results suggest that LWD reintroduction increases thermal heterogeneity within the hyporheic zone but does not significantly impact surface water temperatures.

4.3. METHODS

4.3.1. Flume experiments

The tilting, recirculating flume has a test section 5.0 m long, 0.30 m wide, and 0.70 m deep (Figures 4.1 and 4.2). The sediment section contains well-sorted quartz-feldspar granules ($d_{10} = 1.9$ mm, $d_{50} = 2.4$ mm, $d_{90} = 3.0$ mm), with an approximate porosity of 0.40. Permeability is $\sim 3.4 \times 10^{-9}$ m², based on permeameter measurements for a sample of repacked flume sediment. To represent a single channel-spanning log, PVC pipe was cut to flume width and mounted within the channel. Two sizes of pipe were used with outer diameters of 11.4 and 14.1 cm. Channel slope was 0.12° (0.002 m/m), appropriate for a forested lowland stream. One control experiment was conducted without a channel-spanning log, and six experiments were conducted for various pairs of log size and height above the bed, channel flow depth, and channel velocity (Table 4.1). These parameters reduce to three dimensionless groupings: blockage ratio (fraction of flow depth blocked by the log), gap ratio (fractional log height above the bed), and channel Froude number (calculated with channel depth as the length scale) (Figure 4.1).

Temperature in the flume channel is controlled by a heating/cooling system attached to an additional water recirculation loop. Water from this side-loop mixes with the main recirculating loop (Figure 4.1). In all experiments, surface water temperature is sinusoidal with period of one day and ranges from 19 to 23°C. A temperature sensor was installed at the flume inlet to monitor the surface water. Vertical thermistor arrays were constructed by mounting four HOBO TMC20-HD sensors on thirteen steel rods, which were inserted along the channel centerline below the sediment-water interface to sensor depths of 8, 18, 33, and 48 cm. Horizontal spacing between arrays was 55 cm far from the log and approximately 15 cm near the log. Wires between buried temperature sensors and data loggers were fixed to flume walls to minimize flow interference (Figure 4.2a).

Flume sides were insulated around the sediment section to minimize conduction across the flume walls (Figure 4.2b). Sediment and surface water temperatures were recorded every 5 minutes using HOBO U12 (outdoor) data loggers with accuracy of 0.25°C and resolution of 0.03°C. Amplitude and phase of temperature signals within the sediment and channel were determined from fitting a sinusoidal function with period of one day using a nonlinear least squares inversion approach.

4.3.2. Numerical modeling

Coupled channel and hyporheic flow was simulated following the computational fluid dynamics (CFD) approach of *Sawyer et al.* [in review]: turbulent flow in the channel was linked to porous media flow in the sediment through the pressure distribution at the sediment-water interface. Two-dimensional porous flow in sediment was solved using the steady-state groundwater flow equation:

$$\nabla \cdot \left(-\frac{k\rho_w g}{\mu} \nabla h \right) = 0, \quad (4.1)$$

where k is sediment permeability, μ is fluid viscosity, ρ_w is pore water density, g is gravity, and h is head ($P/\rho_w g + z$, where P is gage pressure). Darcy velocity or groundwater flux, q , equals the term in brackets. Fluid viscosity and density were assumed constant. Pressure at the sediment-water interface was specified from turbulent open-channel flow simulation. The base and sides of the porous flow domain (flume walls) were assigned no-flow boundaries. In all simulations, the sediment was homogeneous and isotropic. Porosity was 0.40 and permeability was $3.4 \times 10^{-9} \text{ m}^2$.

Heat flow within the sediment was linked with fluid flow using the advection-conduction equation:

$$\rho c \frac{\partial T}{\partial t} = -\rho_w c_w \nabla \cdot qT + \nabla \cdot \kappa \nabla T, \quad (4.2)$$

where T is temperature, t is time, ρ is bulk density, c is bulk heat capacity, c_w is pore water heat capacity, κ is bulk thermal conductivity, and q is specific discharge from pore water flow simulations. Thermal dispersion is assumed negligible. Bulk heat capacity (c) was calculated based on arithmetic mean mixing ($c = nc_w + (1-n)c_g$, where c_g is grain conductivity). Bulk thermal conductivity was calculated based on geometric mean mixing ($\kappa = \kappa_w^n \kappa_g^{1-n}$, where κ_g is grain conductivity and κ_w is pore water conductivity). In all simulations, c was 2.93×10^6 J/m³-K, and κ was 1.31 W/m-K. I divided the top boundary (sediment-water interface) into two zones based on a specific discharge threshold (Figure 4.3): neutral/downwelling regions were assigned a diel temperature signal, and rapid upwelling zones were treated as convective flux boundaries. Specifically, convective flux boundaries were assigned to upwelling regions with thermal Peclet number (Pe) greater than 2:

$$Pe = q \sqrt{\frac{\tau}{\pi D}} . \quad (4.3)$$

τ is the diel timescale (1 d), and D is bulk thermal diffusivity ($\kappa/\rho c$). Flume walls were treated as insulation boundaries. Initial temperature in the sediment was assigned the mean river temperature (21°C). To remove the impact of model initialization on simulated periodic temperature signals, I did not include the first four days of simulation in any analysis. As in flume experiments, amplitude and phase of temperature signals from numerical experiments were determined from fitting a sinusoidal function with period of one day using a nonlinear least squares inversion approach. In low-amplitude regions where phase lags might be greater than 24 hours, I subtracted one cycle from the phase.

Numerical simulations were used to quantify heat flux across the sediment-water interface. Advective and conductive heat flow across the bed per unit channel width were calculated as:

$$J_a = \int \rho_w c_w q_z T dx, \quad (4.4)$$

and

$$J_c = \int \kappa \frac{\partial T}{\partial z} \Big|_{z=0} dx. \quad (4.5)$$

Positive values indicate upward net heat transport to the surface water. Total heat flux (J_t) is the sum of advective and conductive heat flow components.

We also assessed the impact of upwelling hyporheic water on river temperature. Consider a section of river with discharge Q_{sw} and volumetric rate of upwelling hyporheic water Q_{up} . If river temperature is T_{sw} immediately upstream of the inflow, the change in river temperature due to upwelling pore water (ΔT) is:

$$\Delta T = \frac{Q_{up}}{Q_{sw} + Q_{up}} (T_{up} - T_{sw}). \quad (4.6)$$

T_{up} is the equilibrium temperature of mixed upwelling pore water, calculated as:

$$T_{up} = \frac{\int T q_z(x,0) dx}{\int q_z(x,0) dx}, \quad (4.7)$$

where the integral limits are defined by the upwelling region. Essentially, T_{up} is the flux-weighted temperature of upwelling pore water. Hyporheic exchange only impacts surface water temperature if the exchange rate is high and the temperature of upwelling water is significantly different from the upstream surface water temperature.

Pore water flow and heat transport equations were solved using the finite-element method implemented in COMSOL Multiphysics [COMSOL AB, 2006]. The sediment domain consisted of more than 63,000 triangular elements with node spacing of less than 1 cm at the top and less than 2 cm at the base (Figure 4.3). Further grid refinement did not change the solution.

4.4. RESULTS

4.4.1. Observed temperature dynamics

In Trial 1, temperature patterns are one-dimensional: temperature does not vary in the downstream direction (Figures 4.4 and 4.5). Amplitude decays and phase lag increases with depth. Diel amplitudes at depths of 8, 18, and 33 cm below the sediment surface are 57%, 31%, and 12% of the amplitude in the river, respectively.

In Trials 2 through 7, a channel-spanning log drives hyporheic exchange and thermal convection within the sediment, resulting in multi-dimensional hyporheic temperature patterns (Figure 4.4). Upstream and immediately beneath the log, thermal dynamics resemble that of downwelling river water—diel amplitudes are large, and phase lags are small. Downstream from the log, thermal dynamics within shallow sediment resemble that of deep groundwater—diel amplitudes are negligible, and phase lags are significant (Figures 4.4 and 4.5). As an example in Trial 4, diel amplitudes immediately upstream of the log at depths of 8, 18, and 33 cm below the sediment surface are 100%, 100%, and 96% of the amplitude in the river, respectively. In contrast, amplitudes less than a meter downstream are only 15%, 19%, and 25% at the same depths, and amplitudes are depth-inverted (temperatures are most stable at shallow depths). Note that temperatures oscillate twice daily at shallow sensors in upwelling zones in Trials 4 and 5 (Figure 4.5)—these temperature signals have additional frequency content.

Thermal zonation near the log increases with blockage ratio (compare Trials 2, 3, and 5 in Figure 4.4) and Froude number (compare Trial 3 with 4 and Trial 2 with 5 in Figure 4.4). Trials 2 and 6 suggest that gap ratio does not have a large influence on thermal dynamics, although the difference in gap ratios is small. Trial 7 essentially has a negative gap ratio, since the log is partially buried, and the thermal patterns are again

similar to Trials 2 and 6. However, the blockage ratio is also smaller in Trial 7 because the log is only partially exposed to surface water flow.

4.4.2. Modeled temperature dynamics and inferred heat exchange contributions

Simulated hyporheic thermal dynamics are generally similar to observations (Figure 4.6) but tend to overestimate the amplitude and phase of diel thermal signals at greater depths. In all cases, a zone with large diel temperature fluctuations forms below and upstream from the log. This zone generally coincides with the shortest hyporheic flow paths nearest the log, where flow is also fastest (Figures 4.6 and 4.7b). The region of strong diel fluctuations increases in size with blockage ratio (Trials 3, 4, and 5) and Froude number (Trials 4 and 5). Further downstream from the log, temperatures are stable, even at shallow depths. The region of stable temperature occurs where deeper hyporheic water emerges, typically within 25 to 75 cm of the log center (Figures 4.6 and 4.7c).

In general, the location of maximum upwelling is located immediately beneath and adjacent to the log, and the rapidly upwelling water has a large diel temperature range (Figure 4.7). Further downstream where upwelling rates are significantly reduced, upwelling water taps deeper flow paths, and temperatures are stable. Because most upwelling water originates from short, fast hyporheic flow paths with strong temperature fluctuations, the temperature of upwelling water is not significantly different from the surface water temperature (Figure 4.7c). In Trials 4 and 5 with greatest hyporheic exchange rates, upwelling temperatures are nearly identical to surface water temperatures. In Trial 7 where the log is partially buried, the temperature of upwelling water is moderately buffered, but the rate of exchange with surface water is relatively slow.

For all experiments, net total heat flow is generally into the hyporheic zone when surface water temperature is rising and out of the hyporheic zone when surface water temperature is falling (Figure 4.8). In Trial 1, heat flow across the bed is due to conduction—the log is absent, and hyporheic exchange is negligible. In all other trials with a log, advection contributes substantially to heat flow across the bed (Figure 4.8). Advective and conductive heat flow contributions are comparable in Trials 2, 6, and 7 where blockage ratios are smallest. Advective heat flow dominates total heat exchange in Trials 3, 4, and 5 where blockage ratios are greatest.

4.4.3. Role of permeability in hyporheic temperature dynamics

Hyporheic fluid and heat flow were simulated for Trial 5 with a 10-fold and 100-fold reduction in permeability. The change in permeability does not alter hyporheic fluid flow patterns but decreases seepage rates proportionately. As a result, advective heat transport and thermal zonation within the hyporheic zone decline (Figure 4.9). For a 10-fold reduction in permeability, the region of large diel temperature fluctuations near the log decreases in size. The wedge of upwelling water with stable temperatures also decreases in size and shifts slightly upstream. For a 100-fold reduction in permeability, diel temperature profiles are nearly constant with distance along the channel. The log has a negligible impact on hyporheic thermal patterns. The permeability in this case is typical of silty sand [*Freeze and Cherry, 1979*].

The thermal Peclet number (Equation 4.3) reflects regions within the hyporheic zone where advection dominates conduction over the timescale of interest (diel in this case). Therefore, regions with greater Pe correspond with more advective heat flow and greater perturbation of conductive diel signals. Significant thermal perturbation occurs in the general region of large seepage rates defined by $Pe > 1$. This zone occurs near the log, where seepage rates are fastest (Figure 4.9). The advection-dominated region

decreases in size as permeability decreases. Notably, Pe is specific to the timescale of thermal oscillations. Longer timescales correlate with larger Pe . Therefore, slower hyporheic flows will have relatively larger Pe for seasonal timescales, which suggests that hyporheic thermal dynamics should be more sensitive to seasonal timescales, even in less permeable sediment.

4.5. DISCUSSION

Hyporheic exchange associated with LWD drives significant thermal heterogeneity at the meter scale within the hyporheic zone. As blockage ratio, Froude number, and permeability increase, advective heat flow increases within the hyporheic zone, producing greater thermal perturbation in upwelling and downwelling regions. For the range of blockage ratios and Froude numbers considered here, thermal heterogeneity is negligible for permeabilities typical of silty sand but substantial for clean sand and gravel. An implication is that streambed clogging near LWD and other in-stream structures drastically reduces hyporheic exchange rates and thermal heterogeneity within the hyporheic zone.

Numerical simulations tended to overestimate the amplitude and phase of diel temperature signals in the sediment, particularly at greater depths where hyporheic exchange is slow. In flume experiments, heat probably conducted through the flume's side walls, which caused additional amplitude attenuation within the sediment, particularly at greater depths where advective heat flow was minimal. Although exterior flume walls were insulated (Figure 4.2), the insulation did not entirely eliminate lateral conduction transverse to the channel. I did not simulate three-dimensional heat flow, which would have drastically increased computation time. Additionally, appropriate boundary conditions for the side walls were unclear, since insulation partially limited conduction. Regardless, two-dimensional numerical models adequately predicted the

general trends in diel thermal patterns across different blockage ratios, Froude numbers, and gap ratios.

The numerical simulations suggest that hyporheic exchange near LWD negligibly impacts diel thermal dynamics in the river. Most upwelling water originates from short, fast hyporheic flow paths, so the diel temperature signal of upwelling water closely follows the river temperature signal. A major implication is that increasing the rate of hyporheic exchange will not increase the perturbation to surface water temperature. In a reach with many logs and rapid hyporheic exchange, the impact on surface water temperature will remain negligible because the upwelling pore water temperature resembles the river temperature (Equation 4.6). *Hester and Doyle* [*Hester et al.*, 2009] similarly found that vertical hyporheic exchange beneath a weir negligibly influenced diel river temperatures. I suggest that the style of hyporheic exchange near any channel obstruction such as a weir or boulder precludes a significant hyporheic effect on surface water temperatures. The flux-weighted majority of hyporheic water in these cases originates from nearby points in the channel along fast flow paths, so the temperature signal of upwelling water approximates the river temperature signal. In contrast, *Arrigoni et al.* [2008] and *Arscott et al.* [2001] found that long hyporheic flow through bars and between tributaries drove patterns in surface water temperature. When long hyporheic flow paths deliver more water to channels than short flow paths, opportunities for significant modification of surface water temperature exist.

We employed a novel flume approach for studying hyporheic fluid and heat exchange in which I manipulated LWD within the channel and isolated the influence on thermal dynamics within the hyporheic zone. Similar experimental manipulations have been conducted in the field for understanding weir-induced hyporheic fluid and heat exchange [*Hester et al.*, 2009]. One benefit of conducting experiments in a flume is the

ability to control surface water temperature, river discharge, and sediment permeability. Additionally, the flume approach eliminates competing forces such as solar heating, riparian shading, and variable groundwater inputs. A drawback of this approach is the cost and technical challenge of equipping flumes for temperature control. Furthermore, flume experiments do not replace the need for field experiments to understand interactions between atmosphere-river-groundwater systems.

4.6. CONCLUSIONS

LWD drives significant thermal heterogeneity within the hyporheic zone at the meter-scale. Thermal zonation increases with LWD blockage ratio, Froude number, and sediment permeability. Of these three factors, permeability varies the most widely in rivers and likely exerts the greatest control on hyporheic fluid and heat exchange. Hyporheic heat advection accounts for a large fraction of the total heat flux across the streambed in all cases examined here. Nevertheless, advective heat exchange negligibly impacts diel thermal dynamics within the surface water. Numerical simulations reveal that the flux-weighted diel temperature signal of upwelling hyporheic water is similar to the diel temperature signal in the surface water. Therefore, even high densities of LWD should not modify surface water temperatures at the reach scale. If LWD has any impact on surface water temperature, the effects are localized within small, relatively slow-flowing or recirculating pools.

LWD removal and channel-clearing practices are examples of human modifications to channels that decrease hyporheic exchange and lead to thermal homogenization of hyporheic and benthic zones. LWD reintroduction is an increasingly popular restoration tool that is often implemented with the aim of improving fish habitat. I have shown that LWD also promotes patchy thermal regimes within benthic and hyporheic environments, which should increase habitat diversity for invertebrates.

<i>Trial</i>	<i>d</i> [cm]	<i>v</i> [cm/s]	<i>D</i> [cm]	<i>a</i> [cm]	<i>Fr</i> []	<i>B</i> []	<i>G</i> []	$Q_{up}/(Q_{up}+Q_{sw})$ [%]
1	25	8	n/a	n/a	0.05	n/a	n/a	~ 0
2	25	8	11.4	4.0	0.05	0.46	0.16	0.22
3	25	8	14.1	4.0	0.05	0.56	0.16	0.39
4	25	12	14.1	4.0	0.08	0.56	0.16	1.2
5	17	8	11.4	4.0	0.06	0.67	0.24	1.2
6	25	8	11.4	5.4	0.05	0.46	0.22	0.20
7	17	8	11.4	-5.7	0.06	0.34	-.34	0.16

TABLE 4.1: PARAMETERS FOR FLUME EXPERIMENTS and numerical simulations (Figure 4.1). Also indicated is the hyporheic exchange rate across the flume bed normalized by discharge ($Q_{up}/(Q_{up}+Q_{sw})$), which influences surface water temperature (Equation 4.6).

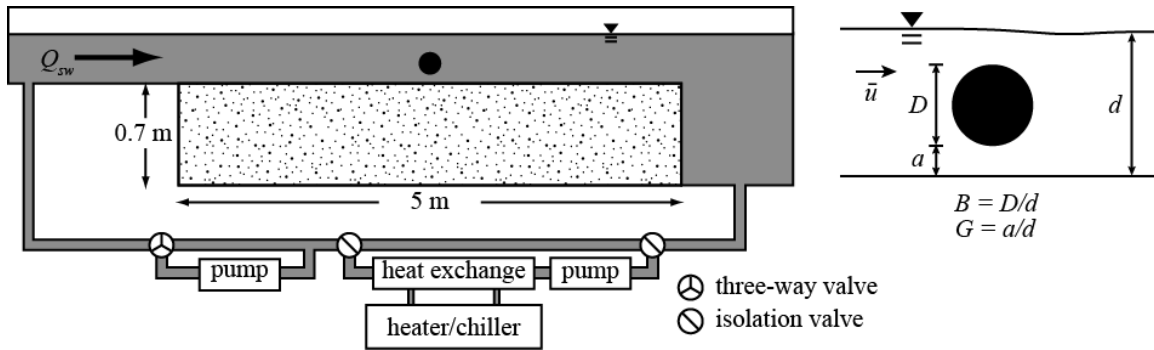


Figure 4.1: Flume (left) and experimental variables (right). Recirculating channel water mixes with water from the heater/chiller to achieve programmed surface water temperatures. Key experimental parameters include blockage ratio (B), gap ratio (G), and channel Froude number (calculated with channel depth as the length scale).



Figure 4.2: Channel-view of flume showing temperature loggers and wires to sensors (a). Side-view of flume showing insulation applied around the sediment section (b). White arrows indicate surface water flow direction.

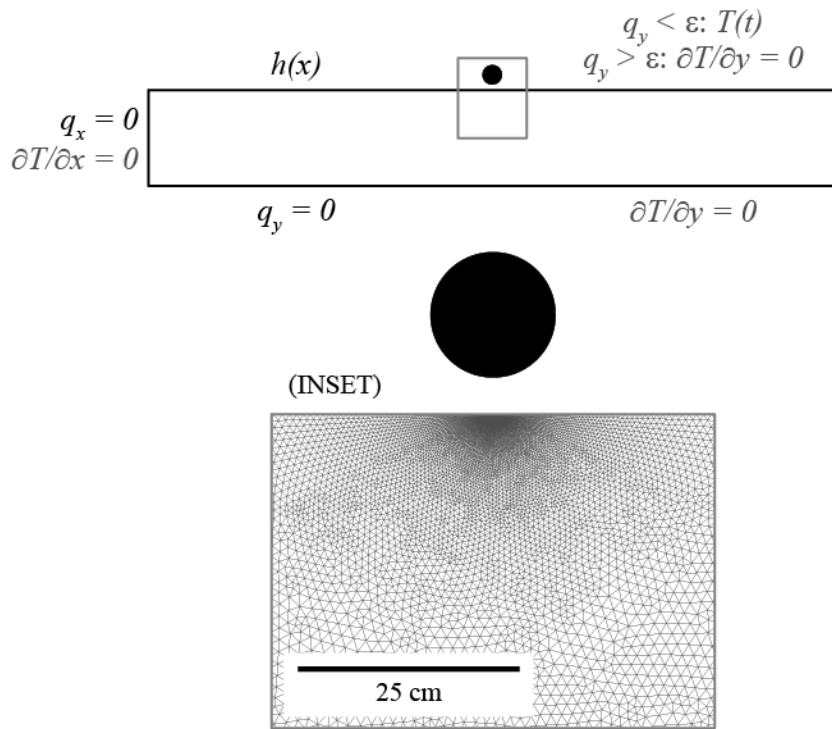


Figure 4.3: Boundary conditions (above) for porous fluid flow (black text) and heat flow (gray text). ε is the positive vertical Darcy velocity where $Pe = 2$ (Equation 4.3). Gray box indicates the region where mesh is shown (below).

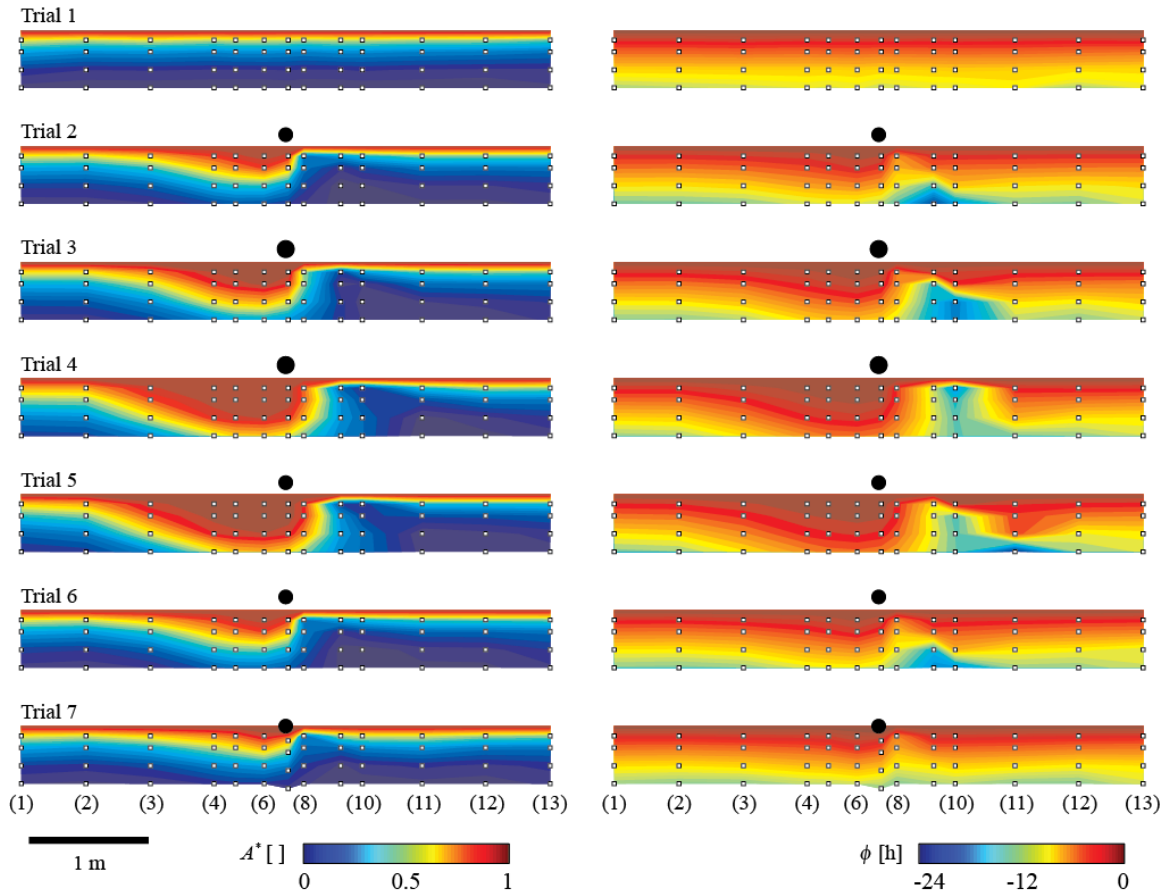


Figure 4.4: Amplitude and phase response of diel temperatures within hyporheic zone for seven flume experiments (Table 4.1). A^* indicates ratio of amplitude of pore water temperature to surface water temperature. Negative ϕ (in hours) indicates a lag of pore water temperature behind surface water temperature. Squares denote thermistor locations, which are numbered longitudinally. Log position is indicated with a black circle drawn to scale. Surface water (not shown) flows from left to right. At the sediment surface, A^* is assumed to equal one and ϕ to equal zero for contouring purposes. Without a log, temperature patterns are one-dimensional. Below and upstream from a log, amplitudes are large and phase lags small. Downstream, amplitudes are small and phase lags large. Thermal zonation increases with blockage ratio and Froude number (Trials 3, 4, 5).

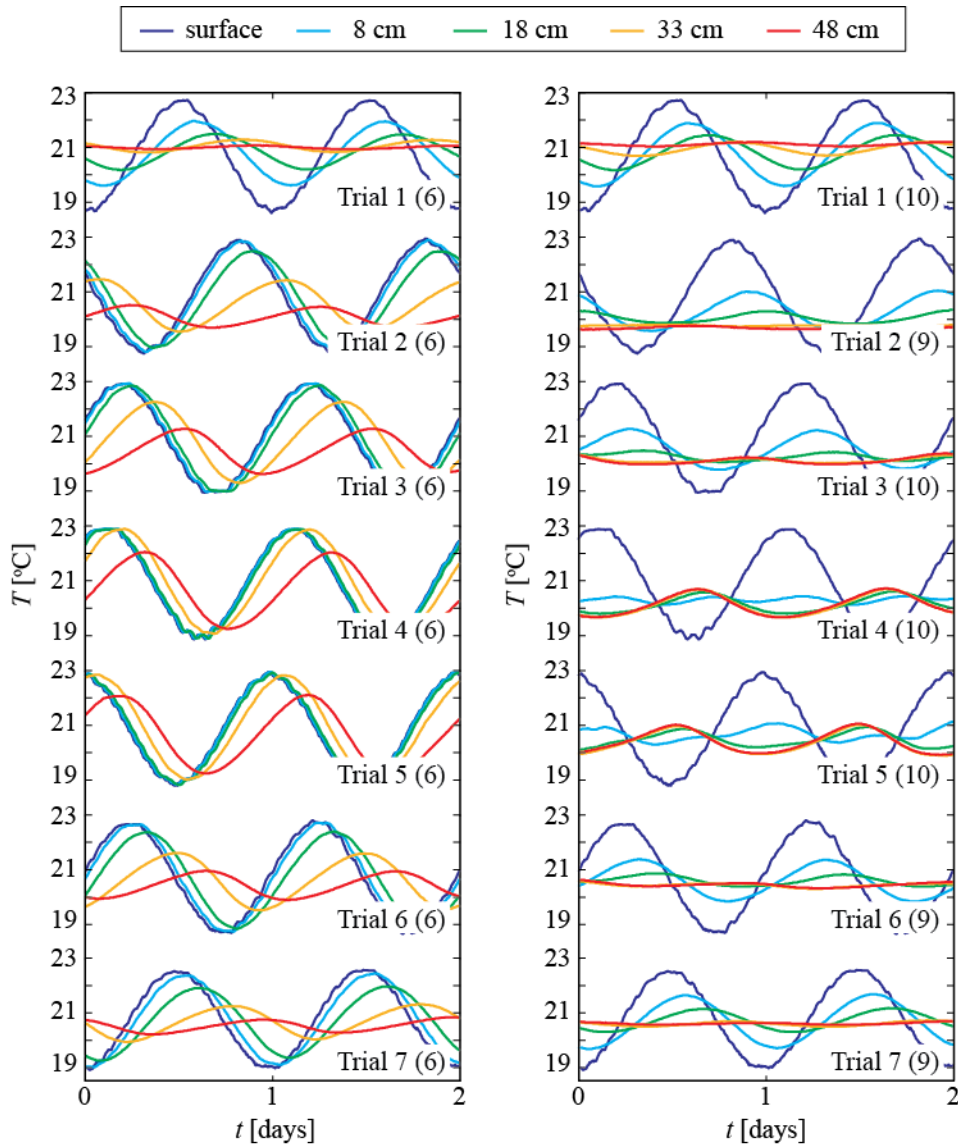


Figure 4.5: Examples of temperature signals from representative vertical arrays in downwelling zones (left column) and upwelling zones (right column). Numbers indicate thermistor locations from Figure 4.4. Note the temperature signals in shallow upwelling zones display additional frequency content in Trials 4 and 5.

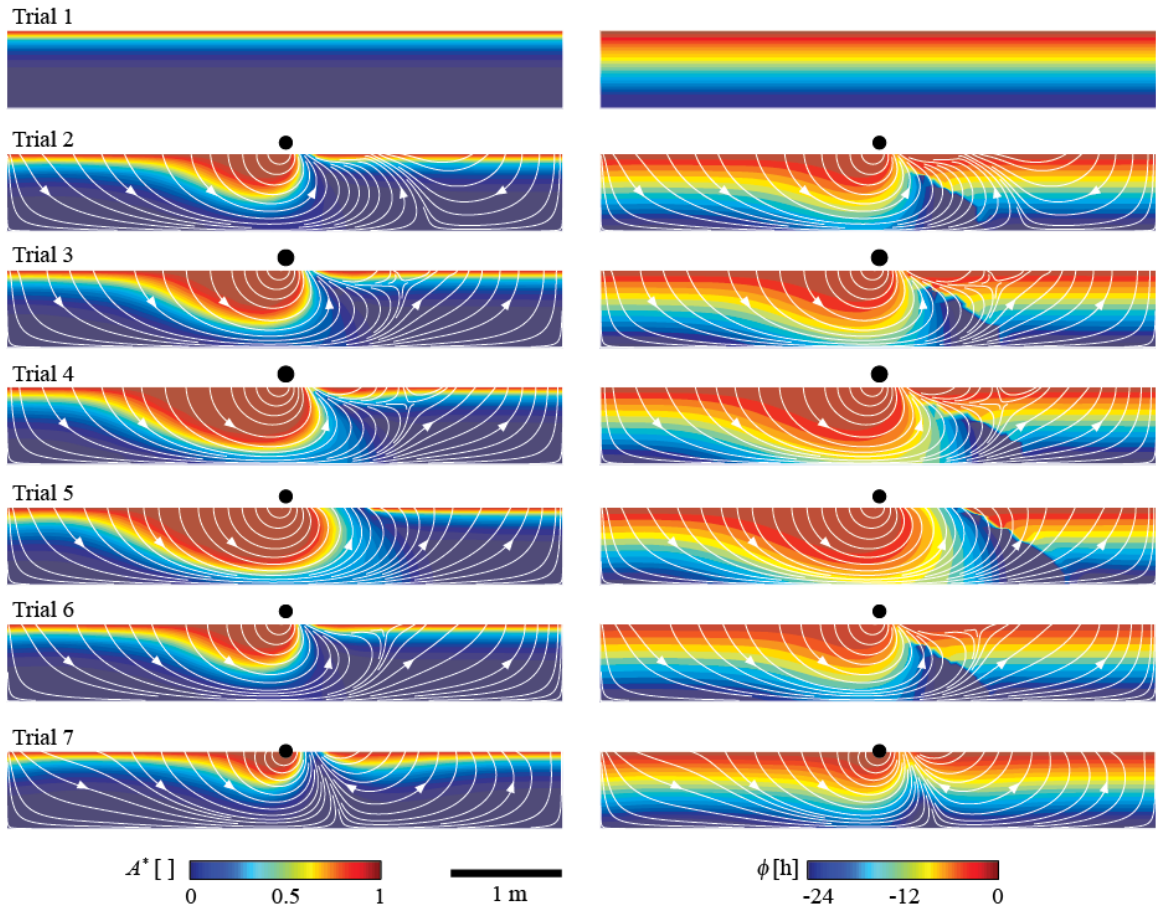


Figure 4.6: Numerically simulated amplitude and phase response of diel temperatures within hyporheic zone for seven experiments (Table 4.1). A^* indicates ratio of pore water amplitude to surface water amplitude. Negative ϕ indicates a lag of pore water temperature behind surface water temperature. Surface water (not shown) flows from left to right. Hyporheic streamlines are shown in white. Hyporheic heat advection due to LWD drives large amplitudes and small phase lags in downwelling zones and along short flow paths. Where water upwells from deeper flow paths, amplitudes are small and phase lags are large. Simulated amplitudes are larger than measured (Figure 4.5), due most likely to lateral conduction through flume side walls.

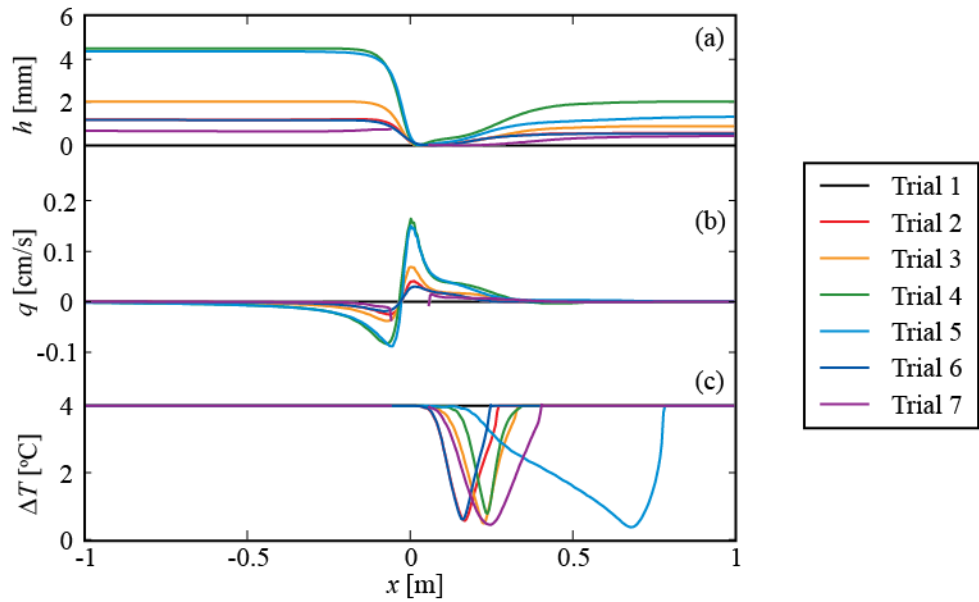


Figure 4.7: Head distribution (a) along the bed surface due to channel flow around a log drives vertical fluid exchange across the bed (b). Positive seepage rates (q) indicate upwelling. Exchange rates are fastest near the log and decay exponentially with distance upstream and downstream. (c) In regions where upwelling is rapid, the diel temperature range (ΔT) of upwelling water is almost as large as the temperature range in the channel (4°C). Immediately downstream where upwelling is slower, the diel temperature range is greatly reduced.

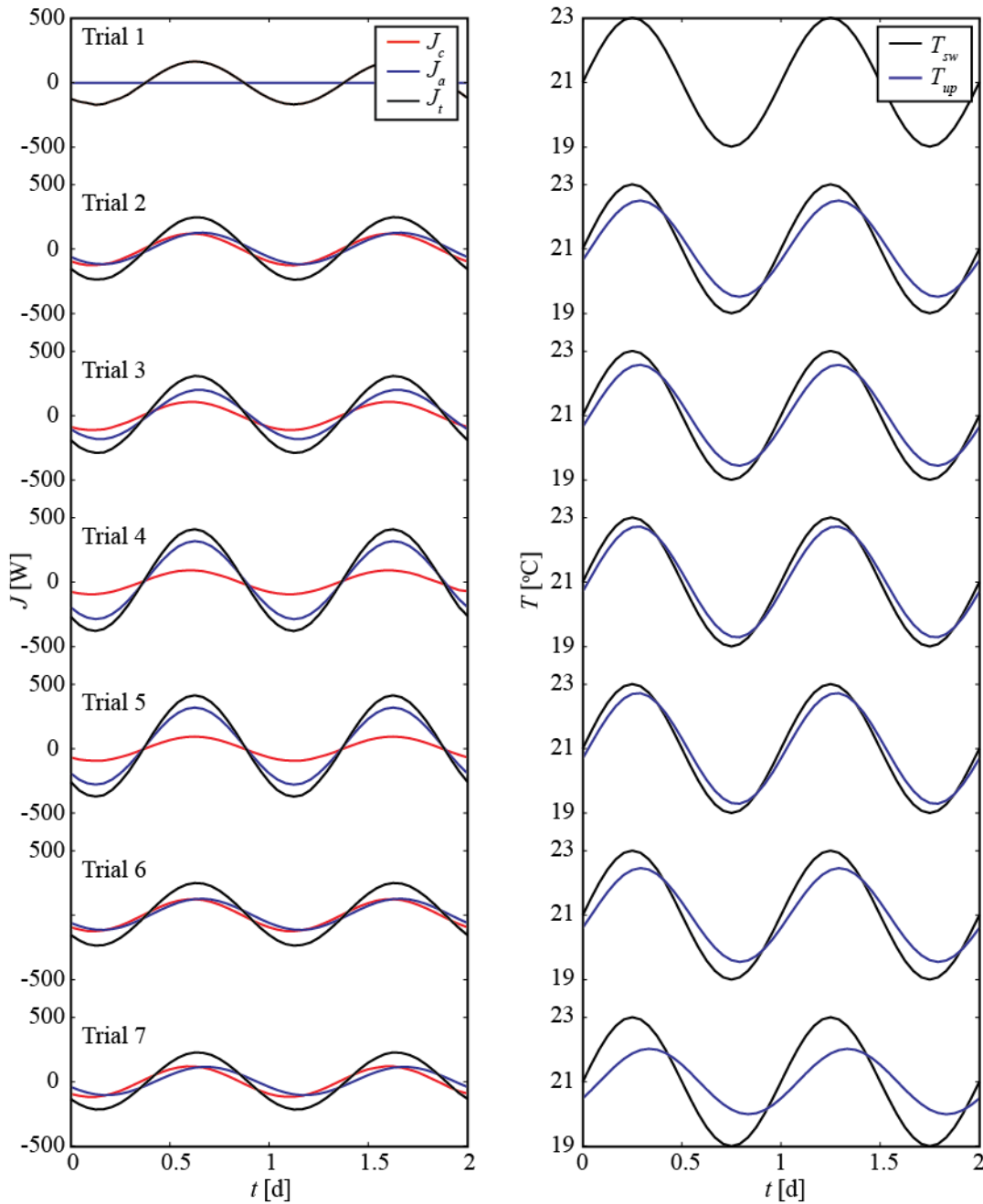


Figure 4.8: Conductive, advective, and total heat fluxes versus time for each trial (left). Conductive heat fluxes are similar for all trials, but the advective contribution to the hyporheic heat budget is substantial for cases with a log. Surface water temperature (T_{sw}) and flux-weighted temperature of upwelling water (T_{up}) (right). Upwelling water is only slightly buffered and lagged relative to surface water temperature in all cases and therefore has minimal capacity to influence surface water temperature.

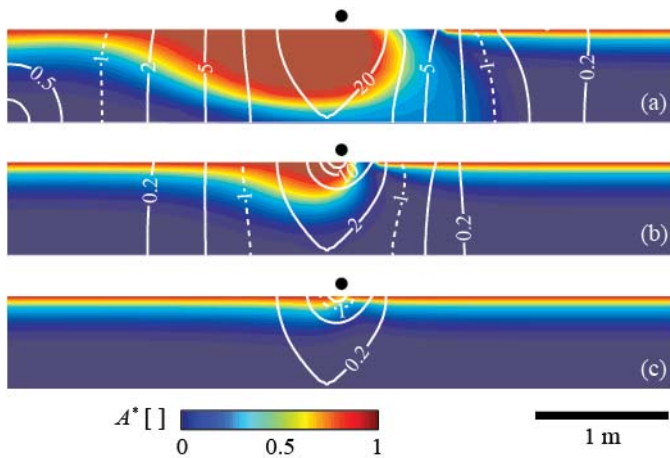


Figure 4.9: Numerically simulated amplitude of diel temperatures within hyporheic zone for Trial 5 (a), a ten-fold reduction in permeability (b), and a hundred-fold reduction (c). A^* indicates ratio of pore water amplitude to surface water amplitude. White lines indicate contoured Peclet numbers for values of 0.2, 0.5, 1, 2, 5, 10, and 20. Surface water (not shown) flows from left to right. For a 10-fold reduction in sediment permeability, thermal heterogeneity within the hyporheic zone declines significantly. For a 100-fold reduction ($k = 3.4 \times 10^{-11} \text{ m}^2$), thermal heterogeneity is negligible. The region with $Pe > 1$ (dashed line) approximately delineates where advection perturbs conductive thermal dynamics.

Chapter 5: Effect of large woody debris additions on hyporheic exchange in a losing stream

5.1. ABSTRACT

Channel restoration structures such as large woody debris (LWD) enhance river-groundwater exchange (hyporheic exchange) and may potentially alter heat and solute transport in restored reaches. I added channel-spanning logs to a second-order mountain meadow stream to test the impacts of restored exchange on streambed temperatures and transient solute storage. Local vertical seepage measurements near individual logs and simulations of hyporheic fluid and heat flow show that log additions created meter-scale hyporheic exchange cells in this losing reach. Upwelling pore water downstream of logs created regions of stable diel temperatures within the streambed. Upon log removal, hyporheic exchange was again replaced by uniform downwelling. Although LWD additions contributed to hydrologic and thermal complexity in the benthic environment, the additions negligibly impacted transient solute storage at the timescale of minutes. A major implication is that in similar streams, LWD reintroduction may benefit the quality of benthic and hyporheic habitat but may not significantly improve solute uptake for biogeochemical transformations with fast reaction timescales.

5.2. INTRODUCTION

Large woody debris (LWD) is a dominant morphologic feature in streams that impacts channel roughness and flow conveyance [Curran and Wohl, 2003; Manga and Kirchner, 2000; Shields and Gippel, 1995], traps sediment [Montgomery et al., 1996], controls pool spacing [Montgomery et al., 1995], and drives river-groundwater (hyporheic) exchange [Lautz et al., 2006; Mutz et al., 2007; Sawyer et al., in review]. Modern LWD densities are unnaturally low due to riparian land use and channel clearing

practices [Montgomery and Piégay, 2003]. LWD reintroduction is a common tool for restoring diversity in hydrologic environments and in-stream habitat [Shields et al., 2006].

One potential benefit of LWD reintroduction is an increase in hyporheic exchange [Boulton, 2007], which connects streams with their surrounding aquifers. In restoration efforts, hyporheic exchange has traditionally received inadequate attention [*Hester and Gooseff*, 2010], despite its importance for the movement of heat, organic matter, nutrients, and contaminants within the stream corridor. Hyporheic exchange exposes surface water to microbial-rich sediment, providing opportunities for nutrient retention. The hyporheic zone is also habitat for invertebrates and fish embryos, which are sensitive to temperature, dissolved oxygen, and other biophysical parameters controlled by fluid flow [Brunke and Gonser, 1997].

Few studies have examined the impact of LWD restoration structures on hyporheic exchange and related biophysical processes, but results vary among studies. Lautz and Fanelli [2008] demonstrated that a log dam restoration structure contributed to heterogeneity in vertical head gradients, temperature, and pore water geochemistry upstream and downstream. In contrast, Kasahara and Hill [2006] observed little impact of a constructed step on oxygen concentrations within the hyporheic zone, presumably due to siltation. Scealy et al. [2007] monitored hyporheic fauna in response to wood reintroduction in pools and riffles and showed that greatest increases in abundance and diversity generally occurred in riffle settings.

I added and removed channel-spanning logs a losing mountain meadow stream to assess whether hyporheic exchange near individual logs could improve thermal heterogeneity in the benthic zone. I also assessed larger reach-scale impacts of LWD on mobile-immobile exchange between the main channel and transient storage zones to test

whether log additions could increase solute retention, which affects nutrient availability. I first present the local effects of LWD addition and removal on hyporheic exchange and then describe reach-scale changes in transient storage parameters under various LWD densities. Finally, I integrate the results across spatial scales (from meter-scale to reach-scale) and discuss ecological implications for hyporheic heat and solute transport due to LWD removal or reintroduction. Locally, LWD additions formed hyporheic zones at the meter-scale in an otherwise losing reach with presumably little pre-existing hyporheic exchange. LWD promoted heterogeneity in hyporheic exchange patterns and temperatures. However, at the reach scale, solute retention did not measurably increase with LWD addition.

5.3. STUDY SITE

Experiments were conducted in San Antonio Creek, a second-order meadow stream in Valles Caldera National Preserve (VCNP) in the Jemez Mountains of New Mexico (Figure 5.1). VCNP was created by an act of US Congress in 2000 for conservation, grazing, hunting, and recreation. The experimental reach is at an elevation of 2606 meters above sea level and lies between two small lava domes with elevations of 2782 and 2814 m (Figure 5.1). Reach length is 204 m (Figure 5.1). The reach was selected for its relatively simple morphology, permeable bed sediment, and lack of pre-existing LWD. Woody riparian species are absent in the meadow valley, due in part to temperature, wildfires, and historically intense grazing. Riparian vegetation is dominantly meadow grasses and forbs. Bed slope is 0.006 m/m, and channel width ranges from 1-3 meters. The reach includes two straight runs upstream and downstream, separated by a meander. Subtle pool-riffle structures occur throughout. The bed is armored with cobbles and gravel. Underlying sediment consists of very poorly sorted, unconsolidated volcanoclastic and colluvial sediment ranging from silt to boulders.

Mean annual temperature and rainfall in the region are 9°C and 476 mm, respectively [Bowen, 1996]. VCNP lies near the northern limit of the North American monsoon. Forty percent of annual precipitation falls primarily as snow between October and April. Fifty percent of annual precipitation falls during the monsoon season in July and August [Bowen, 1996]. This investigation was conducted after the hydrograph peak associated with spring snowmelt but prior to monsoon rains. Discharge ranged from 96 to 127 L/s, and water depth was ~20 cm.

5.4. METHODS

5.4.1. Experimental log configurations

Channel-spanning logs were added and then removed to test their impact on hyporheic fluid and heat exchange and transient solute storage over five sets of experiments: initial control without LWD (IC), three experiments with successively greater log separation distances of 12, 24, and 48 m (L12, L24, and L48), and a final control (FC) to assess the effect of declining water table and discharge over the season. In each case, I measured vertical head gradients, surveyed water surface elevations, and monitored streambed temperatures to characterize hyporheic flow patterns around individual logs within a focus sub-reach. At the reach scale, I conducted conservative solute tracer tests to characterize transient storage parameters. The five sets of experiments (IC, L12, L24, L48, and FC) spanned approximately 6 weeks. Equilibration time for hyporheic exchange due to log addition or removal was ~ 1 day or less, based on diel temperature dynamics within the hyporheic zone. I divide my discussion of experimental methods into characterization of local (meter-scale) hyporheic fluid and heat flow and reach-scale transient storage behavior.

5.4.2. Local hyporheic exchange measurements

Nine in-stream piezometers were installed within a focus sub-reach between the locations of the second and fourth logs to measure vertical head gradient in the streambed (Figures 5.2 and 5.3). Piezometer diameter was less than one tenth of log diameter. In-stream piezometers were constructed from 1.7-cm outside-diameter (o.d.) steel pipe and had 3.0-cm screens, which were positioned 30 cm below the top of sediment. Four additional in-stream piezometers were installed randomly outside the focus sub-reach to ensure the sub-reach was representative of the larger reach.

For each experiment, head at in-stream piezometers was measured relative to the surrounding stream's water surface elevation using chalk wire and was averaged from three readings. Water surface elevation was surveyed along the experimental reach using a Sokkia Total Station. Streambed elevations, bank locations, and piezometers were also surveyed.

In addition to the ten in-stream piezometers, sixteen vertical arrays of temperature sensors were installed within the focus sub-reach (Figure 5.2). Vertical thermistor arrays were constructed by mounting four HOBO TMFC0-HD sensors on steel rods, which were inserted in solid, water-filled, 2.13-cm o.d. steel pipes located along the channel centerline. Temperature sensors were installed to depths of 5, 10, 20, and 30 cm below the sediment-water interface in most cases. Five arrays alternately recorded temperatures at greater depths of 60 and 80 cm. Surface water temperatures were recorded within the focus sub-reach and at the upstream and downstream ends of the reach. Temperatures were logged every 5 minutes using four-channel HOBO U12 outdoor data loggers with specified accuracy of 0.25°C and resolution of 0.03°C. Streambed specific heat and thermal conductivity were measured in-situ using a Decagon Devices KD2 Pro probe.

Vertical seepage velocities were estimated from the two shallowest temperature signals at every location according to the method of Hatch et al. [2006] implemented in a MATLAB program called “Ex-Stream” [Swanson and Cardenas, 2010]. The approach is based on an analytical solution that relates vertical seepage velocity to the ratio of diel amplitudes at two depths within the streambed. The solution assumes one-dimensional advective-conductive transport of a diel thermal signal from the streambed into homogeneous sediment under steady porous flow conditions.

Based on Darcy’s law, vertical seepage velocities from heat tracing (v) and head gradients from in-stream piezometers ($\Delta h/\Delta z$) were used to calculate streambed hydraulic conductivity (K) at five collocated piezometers and thermistors:

$$q = nv = -K \frac{\Delta h}{\Delta z}, \quad (5.1)$$

where q is specific discharge. Porosity (n) was assumed equal to 0.3. The estimates of streambed hydraulic conductivity were interpolated across the focus sub-reach for mapping head gradients at all in-stream piezometers to vertical fluid fluxes (Equation 5.1). To further constrain hydraulic conductivity, pneumatic slug tests were conducted at four locations according to the method of Cardenas and Zlotnik [2003a] and analyzed according to Bouwer and Rice [1976]. The slug test apparatus consisted of a 3.1-cm o.d. steel piezometer with 30 cm screen positioned 30 cm below the sediment-water interface.

Vertical heat tracing and head gradient methods provide a one-dimensional estimate of hyporheic exchange. In order to assess two-dimensional hyporheic exchange patterns near the third log, I numerically modeled fluid and heat flow within the streambed using the approach from Chapter 4. Pressure along the top boundary (sediment-water interface) was predicted from log size, height above bed, and channel Froude number [Sawyer et al., in review]. Thermal boundary conditions were mixed: most of the sediment-water interface was assigned a sinusoidal diel temperature signal

with amplitude of 5°C, similar to measured surface water temperatures, but regions of strong upwelling were treated as convective-flux boundaries. At the model base, I assigned two alternate fluid flow boundary conditions: no-flow (representing a neutral reach) and downward flow (representing a losing reach, as observed). The basal boundary condition for heat flow was convective-flux. Model sides were no-fluid-flow and convective-flux boundaries. Domain size was 15 m long and 2 m deep, which was sufficiently large to minimize the influence on fluid and heat flow near the log. Thermal and hydraulic properties of the sediment were chosen based on field measurements (Tables 5.1 and 5.2).

5.4.4. Reach-scale transient storage experiments and simulations

A concentrated solution of NaCl was injected at an approximately constant rate (~35 ml/s) for six hours. Injection rate was verified multiple times throughout the injection period. In-stream conductivity was measured as a proxy for salt concentration every minute using calibrated Aqua Troll 200 probes positioned at 29, 119, and 204 m downstream from the injection point. Water samples were also collected to relate specific conductivity to Cl⁻ concentrations. Samples were filtered to 0.45 µm and refrigerated until analyzed using ion chromatography. Few samples were collected during rapid changes in Cl⁻ concentrations at the beginning and end of injection. However, the samples taken at high and low Cl⁻ concentrations show a consistent relationship with specific conductivity, which is known to be linear in other stream tracer studies [Gooseff and McGlynn, 2005; Wondzell, 2006].

OTIS, a one-dimensional transient storage simulation code, was used to forward-model the specific conductivity breakthrough data [Runkel, 1998]. The governing equation for conservative tracer concentration (or specific conductivity) in the water column is:

$$\frac{\partial C}{\partial t} = -\frac{Q}{A} \frac{\partial C}{\partial x} + \frac{I}{A} \frac{\partial}{\partial x} \left(AD \frac{\partial C}{\partial x} \right) + \alpha (C_s - C) + q_L (C_L - C), \quad (5.2)$$

where C is concentration, t is time, x is downstream distance, A is cross-sectional area, Q is stream discharge, D is dispersivity in the channel, α is the exchange coefficient between storage zone and main channel, and q_L is lateral groundwater inflow rate. The subscript s denotes a parameter of the storage zone, L denotes inflowing groundwater, and lack of subscript denotes the main channel.

The lateral groundwater inflow rate for all experiments was assumed negligible, since plateau Cl⁻ concentrations did not change appreciably with distance downstream and head gradients indicated losing conditions throughout the reach. I did not include loss of stream water to the aquifer in the transient storage model (which affects discharge) because estimated downwelling rates extrapolated over the reach were less than 0.1% of stream discharge. Cross-sectional channel area and discharge were estimated from velocity gaging, plateau Cl⁻ concentrations, and measurements of channel cross-sections.

Transient storage estimates were used to calculate turnover length (L_s) of stream water through transient storage zones:

$$L_s = \frac{Q}{A\alpha}. \quad (5.3)$$

The ratio of reach length to turnover length indicates the proportion of stream water that passes through transient storage along the reach. Turnover is a primary control on solute uptake in streams, since most biologically mediated reactions occur mainly within transient storage (particularly the hyporheic zone where surface water is exposed to microbially active sediment).

In order to compare transient storage metrics with local measurements of hyporheic exchange near individual logs, I calculated the volumetric exchange rate

between the main channel and storage zone per unit length of stream (q_s), average residence time of water in storage (τ_s), and equivalent transient storage depth below the main channel (d_s):

$$q_s = \alpha A, \quad (5.4)$$

$$\tau_s = \frac{A_s}{A\alpha}, \text{ and} \quad (5.5)$$

$$d_s = \frac{A_s}{wn}, \quad (5.6)$$

where w is channel width and n is porosity. In all calculations, I assumed a channel width of 1.5 m and porosity of 0.3 m. Notably, estimates of q_s , τ_s , and d_s may not be representative of the hyporheic zone in a reach with significant immobile storage within the channel. Additionally, stream tracer approaches can fail to detect hyporheic exchange with relatively long residence times such as exchange at the meter-scale through alluvium [Harvey et al., 1996]. In general, tracer experiments only detect a subset of transient storage flow paths typically weighted toward fast, short flow paths.

The design of the tracer experiment impacts the sensitivity of solute breakthrough curves to storage exchange parameters [Harvey and Wagner, 2000]. Optimal sensitivity occurs when downstream transport processes balance storage processes, as expressed in the experimental Damkohler number, DaI :

$$DaI = \frac{\alpha(1 + A/A_s)L}{u}, \quad (5.7)$$

where L is experimental reach length, and u is main channel velocity (Q/A). Minimal uncertainty in transient storage parameters occurs for DaI near unity. DaI range from 1.6 to 3.6 for the first reach (terminating at M2) and from 3.1 to 7.0 for the entire reach (terminating at M3).

5.5. RESULTS

5.5.1. Local hyporheic exchange and streambed temperatures

Without LWD (IC and FC), vertical fluid exchange across the bed was downward throughout the focus sub-reach (Figure 5.3). Average downwelling rates were -3.0 cm/day at the beginning of the season (IC) and -1.8 cm/day at the end of the season (FC). Outside the focus sub-reach, the few scattered vertical head measurements also indicated downward flow, suggesting that the entire reach was potentially losing river water to the surrounding aquifer. Hydraulic conductivity estimates from vertical head gradients and heat tracing were ~1 m/d, while estimates from slug tests were 2-6 times greater (Table 5.1).

With initial log addition (L12), downwelling rates increased immediately upstream from the second and third logs (Figure 5.3). Immediately downstream from the second, third, and fourth logs, regions that were previously downwelling became upwelling. In L24 and L48, the second and fourth logs were removed. Uniform downwelling resumed where the second log had been located. In contrast, local upwelling rates increased where the fourth log had been located. The zone of downwelling broadened near the third log.

Diel streambed thermal dynamics varied strongly in response to log addition and removal. Without logs, diel temperature patterns were essentially one-dimensional—diel amplitudes decayed with depth (Figure 5.4). For example, at four thermistor arrays (T7 through T10), average diel amplitudes were 57, 39, 19, and 8.6% of river amplitudes at depths of 5, 10, 20, and 30 cm, respectively. With a log present, diel amplitudes were greater upstream (Figure 5.4, T7 and T8) and lesser downstream (T9 and T10). At T8 where downwelling was greatest, diel amplitudes were 91, 75, 36, and 15% of river amplitudes at depths of 5, 10, 20, and 30 cm. At T9 where upwelling was greatest, diel

amplitudes were 34, 20, 12, and 6.6% of river amplitudes at the same depths. The streambed thermal response to log addition or removal occurred over less than a day (Figure 5.5).

Simulations of two-dimensional fluid and heat flow predict similar diel temperature patterns in the streambed. Amplitudes are larger immediately upstream of the log where downwelling occurs (Figure 5.6). Downstream of the log, upwelling water stabilizes streambed temperatures. The zone of stable temperature is broader in measurements than simulations, suggesting that simulations predict a more focused upwelling region.

Thermal dynamics are nearly identical in simulations of neutral and losing stream conditions (Figure 5.6). However, flow patterns are significantly different. More than a meter downstream from the log, surface water downwells in the losing case but continues to upwell due to pressure gradients induced by the log in the neutral case. Losing conditions spatially restrict the zone of hyporheic exchange near the log, limiting longer exchange paths and residence times.

5.5.2. Reach-scale transient storage

For all experiments, transient storage parameters were typical of a mountain meadow stream [Harvey and Wagner, 2000] (Figure 5.7, Table 5.3). The exchange coefficient (α) was $8.0 \times 10^{-4} \text{ s}^{-1}$, and the ratio of storage area to main channel area (A_s/A) ranged from 0.071 to 0.15. For comparison, predicted A_s/A based on Darcy-Weisbach friction factor was 0.091 [O'Connor et al., 2010]. Turnover lengths were ~ 400 m, suggesting that approximately 40% of all stream water was exchanged through transient storage zones along the experimental reach. Dispersivity was fairly constant among experiments (Table 5.3). Predicted dispersivity based on hydraulic parameters was $0.12 \text{ m}^3/\text{s}$ [Fischer, 1975; O'Connor et al., 2010], and fitted dispersivity was $0.2 \text{ m}^3/\text{s}$.

However, dispersivity only imprints the solute breakthrough behavior in the early portions of the rising and falling concentration limbs, and the limited sampling in these intervals produced large uncertainty in dispersivity.

The exchange coefficient between the main channel and transient storage zones was approximately constant among experiments (Table 5.3). Storage zone area (both absolute and relative to main channel area) generally declined over the series of experiments as stream discharge declined. Log addition and removal had no coherent impact on storage zone area (if anything, storage area was relatively greater before log addition and after final log removal). Turnover lengths approximately declined with discharge. Log addition and removal had no significant impact on turnover length.

5.6. COMPARISON OF LOCAL HYPORHEIC EXCHANGE WITH REACH-SCALE TRANSIENT STORAGE

The relationship between transient storage and hyporheic zone processes is unclear. The predicted hyporheic zone area per unit channel width under the third log is approximately 1.5 m^2 . If this area is approximately constant for each log, a log spacing of 12 m can be equated with an average hyporheic zone depth of 12.5 cm for L12. Equivalent storage zone depths from tracer studies were comparatively smaller and ranged from 4.4 cm to 10 cm. In fact, equivalent depth is likely even smaller because these estimates assume all exchange area resides directly beneath the channel rather than along banks. One potential explanation is that the tracer experiments only sampled faster (and therefore more shallow) hyporheic flow paths. Storage residence times ranged from only 89 to 190 s. However, if tracer experiments only sampled the fastest hyporheic flow paths, I would still expect an increase in transient storage area and exchange rates with LWD addition. In fact, transient storage metrics do not respond to LWD removal or addition in the direction predicted for hyporheic exchange. Equivalent storage depth

decreases upon initial log addition, when hyporheic depth should increase (compare IC with L12), and equivalent storage depth increases slightly upon log removal, when hyporheic depth should decrease (compare L48 with FC).

If tracer experiments had primarily sampled within-channel transient storage rather than hyporheic storage, equivalent storage area should similarly have increased in response to wood debris. Presumably, LWD addition creates secondary recirculation zones that increase storage. Ensign and Doyle [2005] showed that wood debris removal decreased storage depth and increased residence times in agricultural and blackwater streams, as expected. They attributed much of the behavior to transient storage within the channel rather than hyporheic zone.

5.7. DISCUSSION

Addition of channel-spanning logs created localized upwelling zones within a losing stream. Presumably, hyporheic exchange was negligible prior to log addition. The formation of localized hyporheic exchange cells increased thermal heterogeneity within the streambed. Upon log removal, downwelling resumed and thermal dynamics became longitudinally uniform again. LWD reintroduction is a promising strategy to increase hydrologic connectivity, riverbed thermal zonation, and habitat complexity in streams with simple morphology.

Losing conditions spatially restrict the extent of hyporheic exchange near LWD. Like bedforms and meanders, LWD should drive smaller hyporheic exchange cells with slower exchange rates as losing rates increase [Cardenas, 2009; Cardenas and Wilson, 2007c]. An important implication is that LWD reintroduction maximizes hydrologic connectivity in neutral streams and has no impact on hydrologic connectivity in strongly losing (or gaining) streams. Ecological benefits of restored hyporheic flow paths may be greatest in weakly losing streams, since thermal and chemical diversity within the benthic

environments may initially be low due to the pervasive influence of downwelling surface water. The weakly losing conditions at San Antonio Creek did not temper the impact of channel-spanning logs on diel thermal dynamics—simulated streambed temperatures were similar under neutral and losing conditions. The modest streambed permeability of San Antonio Creek explains the limited impact of ambient downwelling rates on thermal dynamics [*Cardenas and Wilson, 2007d*].

In San Antonio Creek, changes in hyporheic exchange with LWD addition and removal did not significantly impact conservative solute transport within the channel. Although turnover moderately increased with LWD addition between IC and L12 experiments, turnover did not decrease predictably with subsequent log removals. I therefore attribute the increase in turnover between IC and L12 experiments to the decline in discharge. Notably, this turnover behavior is specific to short timescales of transient storage (on the order of minutes). LWD may have a greater influence on turnover through deeper hyporheic zones with longer residence times. However, sampling these flow paths with the same tracer approach would have required a kilometer-scale reach, and wood debris manipulations at this spatial scale would have been prohibitive.

Ultimately, reactive solute uptake in streams depends on the balance between the turnover of streamflow through the hyporheic zone, residence time in the hyporheic zone, and timescale for chemical reaction [*Harvey and Fuller, 1998*]. My experiments suggest that LWD reintroduction may not stimulate more rapid solute uptake for biogeochemical transformations with short reaction timescales (on the order of minutes). However, my findings do not bear on transformations with longer reaction timescales and may not be transferable to reaches with different channel hydraulics and morphology.

5.8. CONCLUSIONS

The addition of channel-spanning logs to a losing stream created hyporheic exchange cells at the meter-scale where hyporheic exchange was previously minimal or absent. Changes in hyporheic exchange due to LWD addition and removal did not lead to resolvable changes in solute turnover lengths. However, hyporheic exchange near logs drove heterogeneity in diel thermal dynamics within the streambed. In particular, diel temperature ranges were reduced in upwelling zones downstream of logs. These upwelling zones could provide refuge for invertebrates during thermal extremes.

LWD reintroduction is a promising tool for increasing patchiness in biophysical characteristics within benthic and hyporheic habitats. However, the impact of LWD reintroduction on hyporheic exchange and hyporheic habitat depends on ambient river-groundwater exchange. LWD reintroduction maximizes the spatial extent and rates of hyporheic exchange in neutral reaches but may have the most significant impact on the quality of hyporheic habitat in weakly losing reaches, since new locations of focused upwelling create distinct thermal and chemical environments that would not have existed elsewhere in the reach. Because LWD addition and removal did not significantly impact turnover lengths over short timescales in this fast-flowing mountain meadow stream, LWD reintroduction may not be a reliable tool for increasing solute uptake in similar streams. Over longer timescales of years or decades, changes in channel morphology and sediment type due to LWD reintroduction could produce significant changes in solute uptake. More long-term studies are needed to address how historic LWD removal and current restoration practices may impact solute retention in watersheds.

<i>Variable</i>	<i>Value</i>	<i>Unit</i>
K , hydraulic conductivity	4.0	m/d
n , porosity	0.3	-
κ , bulk thermal conductivity	1.675	W/K-m
ρc , bulk volumetric heat capacity	3.90×10^6	J/m ³ -K
$\rho_w c_w$, fluid volumetric heat capacity	4.19×10^6	J/m ³ -K

TABLE 5.1: HYDRAULIC AND THERMAL PARAMETERS for two-dimensional fluid and heat flow models.

x [m]	K_{pt} [m/d]	K_{slug} [m/d]
47.02	3.5	16
53.02	1.3	7.9
59.62	2.0	4.4
61.42	0.47	-
68.43	0.30	-

TABLE 5.2: HYDRAULIC CONDUCTIVITY ESTIMATES from piezometer-thermistor data (K_{pt}) and slug tests (K_{slug}).

<i>Trial</i>	Q [L/s]	A [m ²]	D [m ² /s]	A_s [m ²]	α [1/s]	A_s/A []	d_s [m]	τ_s [s]	q_s [m ² /s]	L_s [m]
IC	103	0.30	0.2	0.045	8.0×10^{-4}	0.15	0.10	190	2.4×10^{-4}	430
L12	91	0.30	0.2	0.028	8.0×10^{-4}	0.093	0.062	120	2.4×10^{-4}	380
L24	85	0.28	0.2	0.020	8.0×10^{-4}	0.071	0.044	89	2.2×10^{-4}	380
L48	80	0.27	0.2	0.021	8.0×10^{-4}	0.078	0.047	97	2.2×10^{-4}	370
FC	78	0.26	0.2	0.022	8.0×10^{-4}	0.085	0.049	106	2.1×10^{-4}	380

TABLE 5.3: TRANSIENT STORAGE PARAMETERS for each experiment.

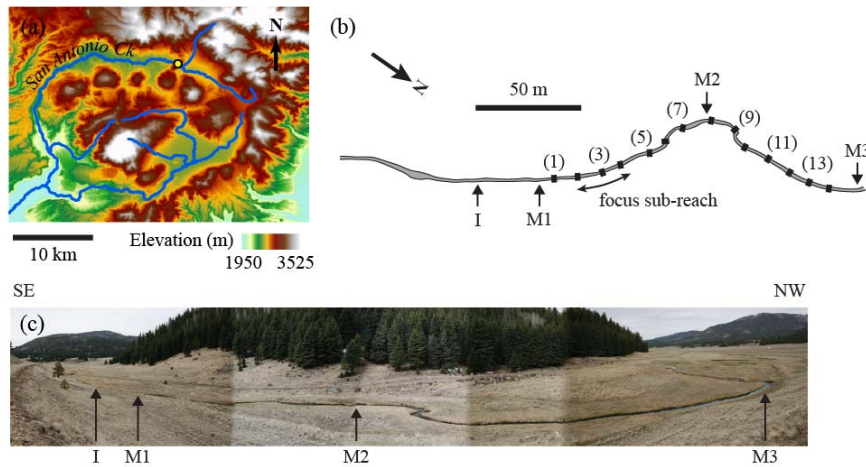


Figure 5.1: Location of experimental reach on San Antonio Creek (New Mexico), indicated with yellow circle (a). The region is geothermally active, and warm springs feed San Antonio Creek downstream from the site. Map of experimental reach (b). Locations of channel-spanning logs are numbered from upstream to downstream. Tracer injection (I) and monitoring locations (M1, M2, M3) are also labeled. Panoramic photograph of reach (c).

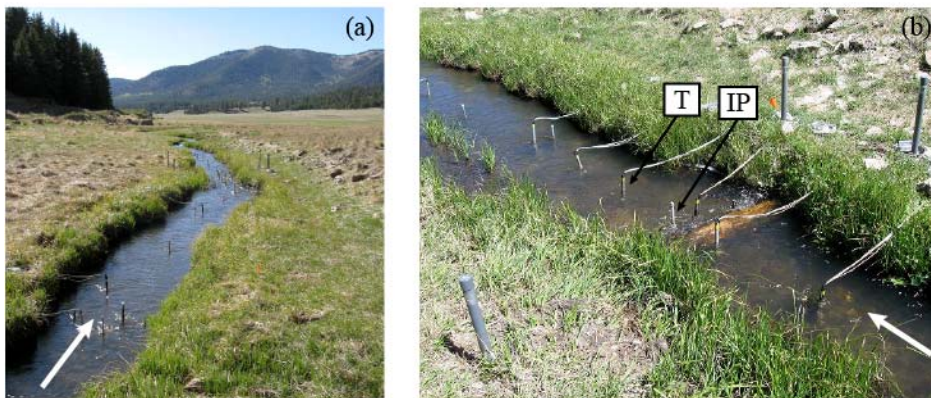


Figure 5.2: Photographs of focus sub-reach without logs (a) and near the third log (b). Stream flow directions are indicated with white arrows. Examples of thermistors (T) and in-stream piezometers (IP) are labeled.

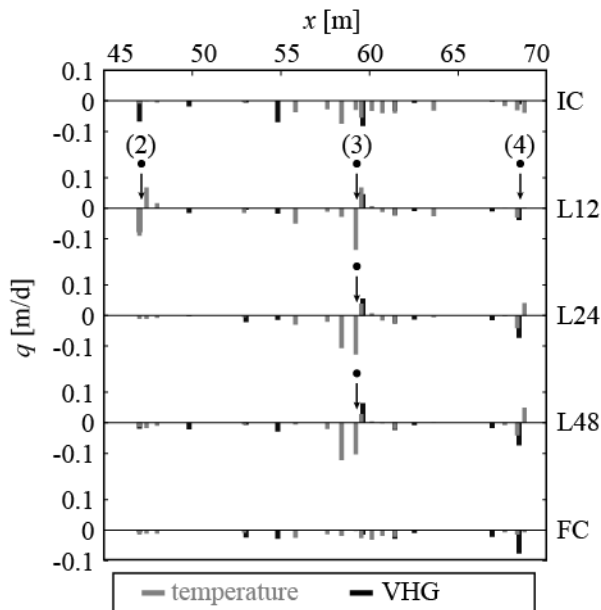


Figure 5.3: Vertical specific discharge estimates along the focus sub-reach for five experiments from heat tracing (gray bars) and vertical head gradients, or VHG (black bars). Log positions are numbered corresponding to Figure 5.1b. The sub-reach is naturally losing (IC and FC), but logs create zones of localized upwelling (L12, L24, and L48).

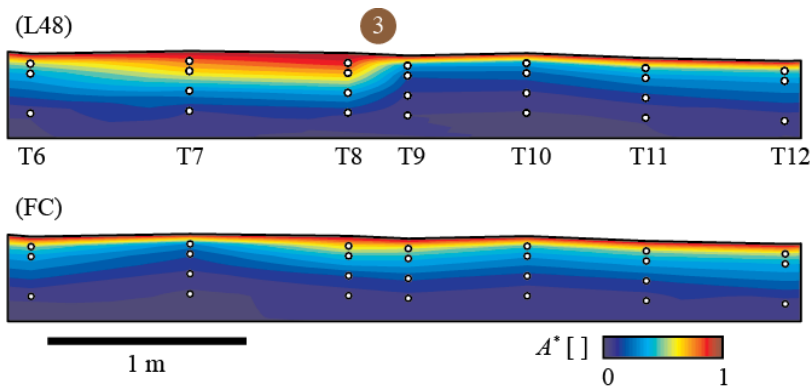


Figure 5.4: Cross-sections of diel pore water temperature amplitudes within the streambed normalized by surface water temperature amplitudes (A^*) before and after removal of the third log (experiments L48 and FC). Stream flow in surface water (not shown) is left to right. Thermistor positions are indicated with circles, and vertical arrays are labeled.

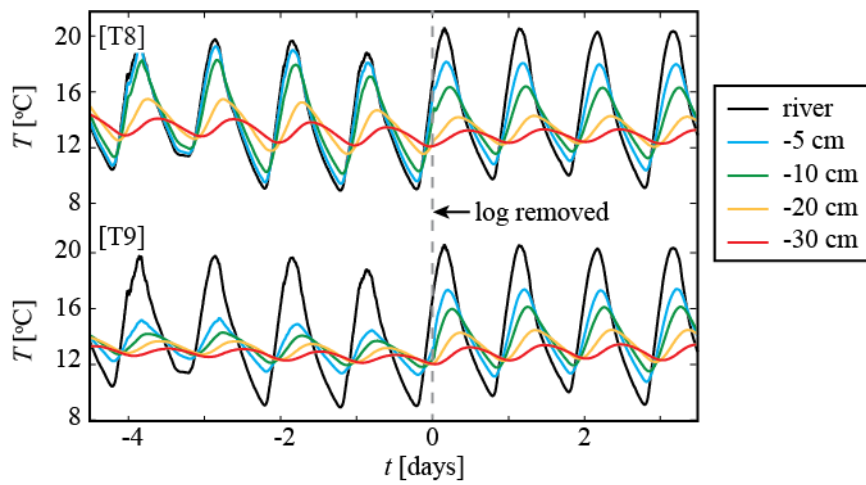


Figure 5.5: Time-series of diel temperatures recorded immediately upstream and downstream of the third log (T8 and T9) during the time of log removal, indicated with dashed line (between experiments L48 and FC). Positions of T8 and T9 are indicated in Figure 5.4.

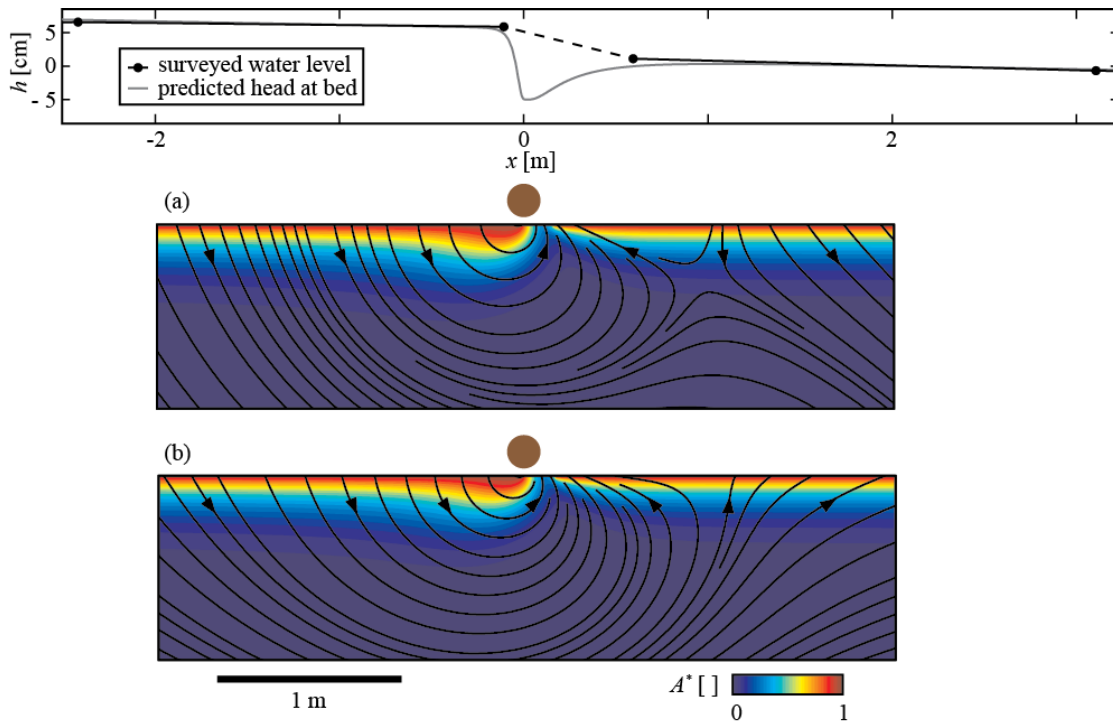


Figure 5.6: Simulated diel pore water temperature amplitudes normalized by surface water temperature amplitudes (A^*) under losing stream conditions (a) and neutral conditions (b) near the third log. Simulated amplitudes are in fair agreement with measurements (Figure 5.4) for both cases. Black lines are simulated streamlines. Predicted variation in head along the bed (upper boundary condition for porous fluid flow simulation) is shown for comparison with surveyed water surface elevation. Head prediction depends on log diameter (18 cm), height above bed (~ 4 cm), channel flow depth (25 cm), and channel Froude number (0.26) [Sawyer *et al.*, in review]. Hydrologic and thermal properties of the simulated porous medium are provided in Table 5.1.

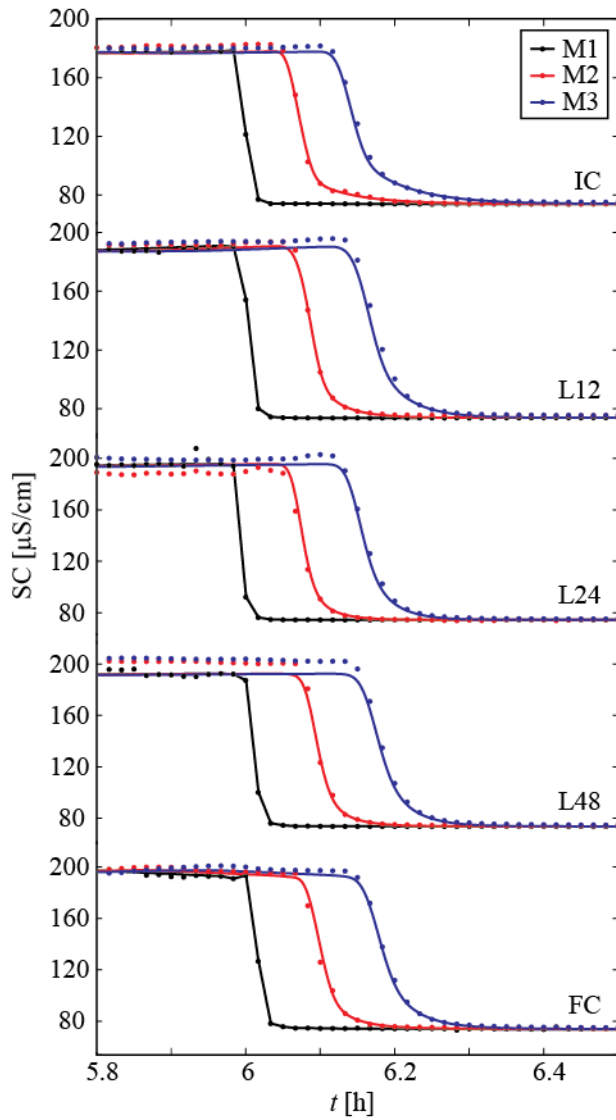


Figure 5.7: Specific conductivity time series during the falling limb of tracer experiments. Specific conductivity (SC) was measured and simulated at M1 (29 m from injection location), M2 (90 m from M1), and M3 (175 m from M1). Locations of injection, M1, M2, and M3 are shown in Figure 5.1. Visually fitted transient storage parameters are provided in Table 5.3.

Chapter 6: Impact of dam operations on hyporheic exchange in the riparian zone of a regulated river

6.1. ABSTRACT

Dam operations commonly cause large, frequent fluctuations in river stage that persist for long distances downstream. The stage fluctuations force river water into and out of the banks, defining lateral hyporheic exchange paths. To evaluate the penetration distance and rates of dam-induced hyporheic exchange, I monitored water table elevation, temperature, and specific conductivity along a transect perpendicular to the Colorado River (Austin, Texas, USA), 15 km downstream of the Longhorn Dam. Stage fluctuates daily by almost a meter. The daily hyporheic exchange volume per meter of bank is 1.0 m³. Dam-induced hyporheic exchange penetrates several meters into the riparian aquifer, while water table fluctuations propagate 30 m into the riparian aquifer. Water chemistry and temperature fluctuate near the channel in response to the flow oscillations. In the absence of dam operations, groundwater would flow steadily through the riparian aquifer toward the river, laterally limiting hyporheic exchange and stabilizing temperatures and water chemistry near the channel. Therefore, dam operations fundamentally change the hydrological, thermal, and geochemical dynamics of riparian aquifers and their hyporheic zones.

6.2. INTRODUCTION

Rivers and groundwater are intimately connected across multiple scales. River water infiltrates into the surrounding bed and banks, travels along short groundwater flow paths, and returns to the channel. These flow paths define the hyporheic zone, a critical ecological transition area between fluvial and groundwater ecosystems that mediates the exchange of water, nutrients, contaminants, and heat [*Brunke and Gonser, 1997; Stanford*

and Ward, 1988]. The hyporheic zone functions as a reservoir for solutes and energy in rivers and facilitates important biogeochemical reactions. Hyporheic exchange therefore affects water quality at the watershed scale [Battin *et al.*, 2008; Ensign and Doyle, 2006; Harvey and Fuller, 1998; Harvey and Wagner, 2000].

Rivers can receive groundwater contributions or lose water to the surrounding aquifer, and these large-scale flow patterns impact the finer patterns of hyporheic exchange. For example, groundwater discharge to a gaining reach limits the size of the hyporheic zone [Boano *et al.*, 2008; Cardenas and Wilson, 2007c]. Since reaches transition between gaining and losing conditions over seasons and flood events [Krause *et al.*, 2007; Lewandowski *et al.*, 2009], hyporheic exchange also varies [Storey *et al.*, 2003; Wondzell and Swanson, 1996]. Some reaches transition between gaining and losing conditions daily in response to stage fluctuations. Daily stage fluctuations can result from natural processes such as evapotranspiration and snowmelt, as well as human activities such as the release of water from hydroelectric dams. In these cases, the daily reversals in gaining and losing conditions represent a unique form of hyporheic exchange. The penetration distance of river water into the surrounding aquifer prior to flow path reversal determines the size of the hyporheic zone. The frequency of flow path oscillations determines hyporheic residence times.

Several authors have claimed that dam-induced river stage fluctuations impact hyporheic exchange [Hancock, 2002; Nilsson and Berggren, 2000; Winter *et al.*, 1998], but few have presented measurements. Curry *et al.* [1994] monitored pressure and water chemistry within the riverbed at brook trout spawning sites in Ontario, Canada during a period of fluctuating dam releases. River stage fluctuations altered vertical hydraulic gradients and water chemistry. Arntzen *et al.* [2006] monitored riverbed pressure, temperature, and water chemistry in a reach of the Columbia River (Washington, USA),

where hydroelectric dam operations induced daily stage fluctuations of up to two meters. They found that vertical head gradients, temperature, and water chemistry oscillated with river stage. They later estimated the rate of vertical hyporheic exchange in response to stage fluctuations [Fritz and Arntzen, 2007]. Hanrahan [2008] monitored pressure and temperature in the bed of the Snake River downstream from Hells Canyon Dam (Pacific Northwest, USA). They found that dam operations only induced vertical flux reversals in a few localized areas and hypothesized that pool-riffle morphology and steep channel gradients predominantly drove hyporheic exchange. Of these studies, only Fritz and Arntzen [2007] estimated a hyporheic exchange rate due to dam operations, and none of these studies estimated the size of the hyporheic exchange zone.

The goal of this study is to estimate the spatial extent and volumetric rate of dam-induced hyporheic exchange using high-resolution temporal data. I monitored pressure, temperature, and specific conductivity along a transect perpendicular to the Colorado River near Austin, Texas, USA. I show that dam-induced river stage fluctuations drive hyporheic exchange meters into the river bank and modulate temperatures and conductivity near the channel. Water table fluctuations and groundwater flow reversals propagate tens of meters into the riparian aquifer. In the absence of dam operations, groundwater would predominantly flow toward the river [Larkin and Sharp, 1992] and limit the hyporheic zone laterally [Boano *et al.*, 2008; Cardenas and Wilson, 2007c]. Therefore, dam operations fundamentally change the hydrodynamics of the hyporheic zone and riparian aquifer.

6.3. STUDY SITE

The study area is located 10 km from downtown Austin, Texas within the 5-km² Hornsby Bend Center for Environmental Research, which borders the Colorado River (Figure 6.1). At Hornsby Bend, the Colorado River is a regulated fourth-order river.

Upstream from Hornsby Bend, the Tom Miller dam releases water daily to generate hydroelectric power for the city of Austin. Between Hornsby Bend and the Tom Miller dam is the Longhorn dam, which forms a recreational lake as well as a cooling reservoir for an adjacent power plant. Two km downstream from the Longhorn Dam, river stage fluctuates by over 2.5 m due to dam operations. Fifteen km downstream at the study site, river stage fluctuates by almost a meter.

Regional groundwater flow is toward the Colorado River at the study site (see Figure 4d in Larkin and Sharp [1992]). The aquifer is composed of modern alluvial deposits, and the average aquifer conductivity is 10^{-4} m/s [Larkin and Sharp, 1992].

6.4. METHODS

6.4.1. Monitoring

Four bank piezometers and one river stage recorder were installed in September 2008 to monitor lateral hyporheic exchange near the channel (Figure 6.2). The distance between the river stage recorder and first bank piezometer is 5.91 m. The distances of bank piezometers from mean shoreline are 2.35 m, 5.08 m, 7.43 m, and 9.48 m. A terrace prevented installation of additional piezometers farther from the river. Bank piezometers were constructed of 5-cm diameter PVC and screened through the water table. Screened intervals range from 1.2 to 2.4 m in length. The river stage recorder was constructed of 1.8 m of screened PVC and anchored in the riverbed with a 1.2-m section of solid PVC. I installed vented In-Situ Aqua Troll 200 probes inside bank piezometers and the river stage recorder to log pressure, temperature, and specific conductivity at 15-minute intervals for seven days. Probes were calibrated for temperature and specific conductivity. Piezometer elevations and bank topography were surveyed using a Sokkia Total Station.

6.4.2. Aquifer characterization

Our primary goal was to estimate hyporheic zone size and exchange rates in response to dam operations, which requires knowledge of aquifer hydraulic properties. I used daily head changes in the river and riparian aquifer to estimate hydraulic diffusivity (D). Analytical solutions for aquifer response to river stage fluctuations are numerous, and the practice of estimating aquifer hydraulic properties from water table fluctuations is common (e.g. Rowe [1960]; Swamee and Singh [2003]; Srivastava [2006]).

Consider a homogeneous, unconfined aquifer adjacent to a river with periodic stage fluctuations. The one-dimensional linearized Boussinesq equation describes transient flow in the aquifer:

$$\frac{\partial h}{\partial t} = D \frac{\partial^2 h}{\partial x^2}, \quad (6.1)$$

where h is hydraulic head, x is distance, and t is time. D is related to hydraulic conductivity (K) by:

$$D = \frac{Kb}{S_y}, \quad (6.2)$$

where S_y is specific yield, and b is saturated aquifer thickness. At the river bank ($x = 0$), the aquifer head equals the river stage:

$$h(x = 0, t) = A \sin(\omega t + \phi), \quad (6.3)$$

where ω is frequency, A is amplitude, and ϕ is phase. At large distance from the river, lateral flow in the aquifer approaches zero:

$$\frac{\partial h}{\partial x} = 0 \quad \text{at} \quad x \rightarrow \infty, \quad 0 \leq t \leq \infty. \quad (6.4)$$

Singh [2004] presented an analytical solution for the head response in the semi-infinite aquifer:

$$h(x, t) = A \exp\left(-x \sqrt{\frac{\omega}{2D}}\right) \sin\left[-x \sqrt{\frac{\omega}{2D}} + \omega t + \phi\right]. \quad (6.5)$$

This solution assumes a straight river and a homogeneous aquifer that is significantly thicker than the amplitude of water table fluctuations. Equation 6.5 also assumes negligible riverbed resistance. By superposition of individual frequency components, Equation 6.5 may represent the aquifer response to more complicated river stage signals.

To evaluate D at the Hornsby Bend site, I determined the amplitudes and phases of the daily (24-hour) river stage and water table oscillations at each piezometer using discrete fast Fourier transforms (FFTs). I then determined D values that minimized the least squares residual error (LSRE) between the measured and predicted heads. Kb was calculated from D (Equation 6.2) by assuming a typical value for S_y [Freeze and Cherry, 1979]. K was calculated by assuming a reasonable estimate of b based on the approximate depth to a regional aquitard.

To independently estimate K , I conducted grain size analyses on sediment samples from the aquifer transect and performed three in-stream pneumatic slug tests near the river stage recorder [Cardenas and Zlotnik, 2003b]. Sediment samples from the aquifer transect were collected during hand-augering and were sieved to determine grain size distributions. Samples were oven-dried and vibrated through a stack of eight sieves. From the grain size distributions, I calculated K according to the methods of Hazen [1911] and Kozeny [1927]. I could only conduct pneumatic slug tests in the riverbed because bank piezometers were screened through the water table. However, the gravel and cobble composition of riverbed sediment visually resembled gravel zones that I encountered in the aquifer while installing bank piezometers.

6.4.3. Estimation of volumetric flow rate

The volumetric flow rate across the bank per unit length of river (Q) is:

$$Q(t) = -Kb \frac{\partial h(x=0, t)}{\partial x}. \quad (6.6)$$

Positive values indicate flow from the river into the aquifer. $Q(t)$ was estimated using the best-fit transmissivity (Kb) and head gradients between the river stage recorder and Bank Piezometer 1. In calculating the head gradient, I projected the head at the river stage recorder to the time-averaged shoreline location.

6.4.4. Estimation of hyporheic zone lateral extent

We estimated the extent of the hyporheic zone using two separate approaches based on the hydraulic and geochemical definitions of the hyporheic zone. In the hydraulic approach, the hyporheic zone comprises all flow paths that start and end in the channel. The advective penetration distance of river water into the surrounding aquifer prior to flow path reversal thus determines the size of the hyporheic zone. I used particle-tracking to estimate this penetration distance. Particle velocities, $v(x,t)$, were calculated from Darcy's Law:

$$v(x,t) = -K \frac{\partial h(x,t)}{\partial x}. \quad (6.7a)$$

Head gradients were estimated from differentiation of Equation 6.5 with respect to x :

$$\frac{\partial h(x,t)}{\partial x} = -A \sqrt{\frac{\omega}{2D}} \exp\left(-x \sqrt{\frac{\omega}{2D}}\right) \times \left[\sin\left(-x \sqrt{\frac{\omega}{2D}} + \omega t + \phi\right) + \cos\left(-x \sqrt{\frac{\omega}{2D}} + \omega t + \phi\right) \right]. \quad (6.7b)$$

In the geochemical approach, the hyporheic zone is the volume of sediment containing at least 10% river water [Triska et al., 1989]. Under this definition, hyporheic exchange includes both advective and dispersive mixing between river water and groundwater. I used mean specific conductivity (\bar{S}) to calculate the proportion of river water in each piezometer (W):

$$W = 100 \frac{\bar{S}_{gw} - \bar{S}}{\bar{S}_{gw} - \bar{S}_{riv}}, \quad (6.8)$$

where \bar{S}_{gw} is the mean specific conductivity of groundwater, and \bar{S}_{riv} is the mean specific conductivity of river water. I assumed \bar{S}_{gw} equals the mean specific conductivity at Bank Piezometer 4, and \bar{S}_{riv} equals the mean specific conductivity at the river stage recorder.

6.5. RESULTS

Water table fluctuations were damped and lagged at every bank piezometer relative to river stage fluctuations (Figures 6.3 and 6.4). Amplitudes of water table fluctuations, in order of increasing piezometer distance from the river, were 71%, 50%, 44%, and 40% of the river stage amplitude. Phases were -5, -11, -14, and -18 degrees, respectively, which correspond to lags of 22, 42, 57, and 70 minutes.

The daily temperature variation in the river was approximately 3 °C (Figure 6.5). River temperature was warmest during the evening and coolest during the morning, consistent with typical diurnal river temperature patterns. In the riparian aquifer, daily temperature fluctuations were subtle in all piezometers except one (Figure 6.6). The piezometer closest to the river (Bank Piezometer 1) recorded daily temperature fluctuations of up to 0.5 °C (Figure 6.6).

Specific conductivity in the river fluctuated daily by approximately 600 $\mu\text{S}/\text{cm}$ (Figures 6.5 and 6.7). Conductivity peaks coincided roughly with river stage minima (Figure 6.5). Within the aquifer, Bank Piezometer 1 recorded the greatest specific conductivity fluctuations ($\sim 500 \mu\text{S}/\text{cm}$) (Figure 6.7). The fluctuations were lagged and attenuated relative to the river conductivity signal. Specific conductivity in Bank Piezometer 3 fluctuated daily by approximately 35 $\mu\text{S}/\text{cm}$, while specific conductivity in Bank Piezometers 2 and 4 varied negligibly over the monitoring period (Figure 6.7). Mean specific conductivities at the bank piezometers increased with distance from the river.

Best-fit D values for individual bank piezometers based on LSRE analysis were 4.0×10^{-3} , 4.2×10^{-3} , 6.2×10^{-3} , and 7.7×10^{-3} m²/s, respectively. To estimate K , I assumed a typical S_y value for sandy gravel of 0.25 [Freeze and Cherry, 1979]. The aquifer thickness (b) is unknown but is likely between 1 and 10 m, based on cuttings from a nearby well that penetrates a regional aquitard. Assuming D equals 5.5×10^{-3} m²/s, K lies between 1.4×10^{-4} m/s and 1.4×10^{-3} m/s (Equation 6.2). For comparison, pneumatic slug tests in the riverbed yielded K values of 6.5×10^{-4} m/s, 7.9×10^{-4} m/s, and 9.7×10^{-4} m/s.

Grain size analyses yielded smaller K estimates. Sediment samples were predominantly composed of poorly-sorted pea-gravel and sand (Figure 6.8). Although cobble-dominated samples were collected from the piezometer transect, they were too coarse for sieving. Of the analyzed samples, mean grain size diameters ranged from 0.5 to 2.5 mm (coarse to very coarse sand). The average K estimate from the grain size distributions is 2.6×10^{-5} m/s.

Assuming a value of 1.4×10^{-3} m²/s for Kb , the instantaneous flow rate across the bank per unit length of river ranged from -11 m²/day to 5.4 m²/day during the monitoring period (Equation 6.6, Figure 6.9). By integration of $|Q(t)|$ through time, the daily exchange volume per unit length of bank averaged 4.5 m³ (3.5 m³ toward the river and 1.0 m³ away from the river). The river was therefore gaining on average, in agreement with Larkin and Sharp [1992]. Of the 3.5 m³ of water that discharged daily from each meter of bank, 2.5 m³ was baseflow, and 1.0 m³ was hyporheic water associated with dam operations. The flow direction was from the river into the riparian aquifer from evening until early morning and from the aquifer to the river from early morning until evening.

Assuming the range of K values from the Boussinesq model, I estimate that the hydraulically-defined hyporheic zone (based on particle tracking) extends 0.18 to 1.8 m

into the riparian aquifer. The geochemically-defined hyporheic zone extends at least 5 m into the riparian aquifer: Bank Piezometer 2 is located 5.08 m from mean shoreline and contains 26% river water (Equation 6.8). Therefore, the size of the hyporheic zone depends on the definition of hyporheic exchange.

While the hyporheic zone extends a few meters into the riparian aquifer, water table fluctuations propagate much farther. The penetration distance of water table fluctuations into the riparian aquifer can be estimated from Equation 6.5, given D . The amplitude of water table fluctuations in the aquifer decays to 10% of the river stage amplitude at a distance x_{10} satisfied by:

$$0.1 = \exp\left(-x_{10}\sqrt{\frac{\omega}{2D}}\right). \quad (6.9)$$

Assuming D equals $5.5 \times 10^{-3} \text{ m}^2/\text{s}$, x_{10} is 28 m at Hornsby Bend (Figure 6.2).

6.6. DISCUSSION

6.6.1. Hyporheic Response to Dam Operations

Dam-induced stage fluctuations at Hornsby Bend force water in and out of the riparian aquifer daily. Flow paths that start and end in the channel constitute a zone of lateral hyporheic exchange. The residence times (hours) and path lengths (centimeters to meters) of dam-induced hyporheic exchange are similar to hyporheic exchange induced by natural processes [*Harvey and Wagner, 2000*]. However, a fundamental difference exists between them. Dam-induced hyporheic exchange is intrinsically transient because unsteady pressures at the sediment-water interface drive the exchange. In contrast, “natural” hyporheic exchange (due, for example, to flow over an undulating riverbed) is comparatively steady because time-averaged pressure gradients at the sediment-water interface drive the exchange.

We can estimate the fraction of river water exchanged through the hyporheic zone between Longhorn Dam and Hornsby Bend using the daily hyporheic exchange volume at Hornsby Bend. One cubic meter of river water enters and exits the hyporheic zone daily per unit length of bank. The daily exchange volume likely increases with proximity to the Longhorn Dam, since river stage fluctuations increase from 85 cm at Hornsby Bend to 2.5 m near the dam (Figure 6.3). Nevertheless, assuming a uniform exchange volume, dam operations pump 30,000 m³ of river water through the hyporheic zone each day along the 15-km reach. The mean discharge recorded at USGS gaging station 08158000 is 30 m³/s (Figure 6.1). Therefore, at least 1% of all river water passes through the hyporheic zone in the 15-km reach. Water table fluctuations also persist downstream of Hornsby Bend, providing new opportunities for hyporheic exchange.

Three potential sources of error may impact my estimate of the daily hyporheic exchange volume, which depends on the Kb estimate from the analytical solution to the linearized Boussinesq equation. First, the analytical solution assumes a no-flow boundary at large distance from the river. A more appropriate boundary condition would be constant flow towards the river. Using a no-flow boundary in place of a constant flow boundary tends to underestimate Kb . The calculated dam-driven hyporheic flux is therefore a minimum estimate. Second, the analytical solution is one-dimensional and assumes a fixed shoreline. In reality, seepage directions in the river banks may include vertical or along-channel components. For example, the anomalously cool mean temperature at Bank Piezometer 1 may be due to multidimensional flow paths (Figure 6.6). Third, the amplitude of river stage fluctuations may represent a significant fraction of the phreatic aquifer thickness. The amplitude of stage fluctuations is 40% of the minimum aquifer thickness estimate. Hornberger [1970] showed for an analogous

problem that the linearized Boussinesq approximation is adequate for amplitudes up to 50% of the mean aquifer thickness.

6.6.2. Chemical and Thermal Implications

Dam operations fundamentally alter hydrologic flow paths within the riparian aquifer up to 30 m from the river at Hornsby Bend (Figure 6.10). In the absence of dam operations, groundwater would flow steadily toward the river through the riparian aquifer like water flowing through gills [*Larkin and Sharp, 1992*]. The steady discharge of groundwater would limit lateral hyporheic exchange [*Boano et al., 2008; Cardenas and Wilson, 2007c*]. In contrast, dam operations induce stage fluctuations that drive river water in and out of the riparian aquifer. The unsteady, reversing flow of water through the riparian aquifer is like the flow of air through lungs (Figure 6.10). Below, I discuss how this fundamental change in riparian aquifer behavior may influence water chemistry and temperature downstream of dams, based on my observations along the Hornsby Bend transect (Table 6.1).

At Hornsby Bend, water chemistry fluctuates in both the river and hyporheic zone (Figure 6.7). The specific conductivity of river water is greatest in between dam releases during baseflow periods and lowest during dam releases when reservoir water dominates the flow (Figure 6.5). Hyporheic exchange transports the specific conductivity signal into the riparian aquifer. As a result, the specific conductivity of pore water near the channel is damped and lagged relative to the specific conductivity of the river (Figure 6.7). In the absence of dam operations, river and riparian aquifer chemistry would fluctuate less (Figure 6.10, Table 6.1). The specific conductivity of river water would consistently resemble values measured during baseflow periods. Since steady groundwater discharge to the river would limit lateral hyporheic exchange, the specific

conductivity of pore water near the channel would consistently resemble the specific conductivity of groundwater.

Along steady groundwater flow paths, a ladder of redox conditions would also regulate nitrogen, sulfur, and organic carbon inputs to the river [Hill, 2000]. I hypothesize that dam operations cause fluctuations in biogeochemical reaction rates within the riparian aquifer. The temporary convergence of chemically distinct waters, such as surface water and groundwater, can increase biogeochemical activity [McClain *et al.*, 2003]. These periods of increased activity, termed “hot moments,” specifically occur when a temporal change in hydrologic flow paths introduces a limiting ingredient that allows the biogeochemical reaction to proceed. The reaction continues as long as a continuous source of reactants persists (typically, as long as the flow paths continue to converge). Examples of processes that trigger hot moments include arroyo floods, storms, and periods of intense snowmelt [McClain *et al.*, 2003]. A goal for future research is to determine whether dam operations frequently induce hot moments.

Dam operations may also impact riparian aquifer temperatures near the channel. At Hornsby Bend, temperatures fluctuated daily up to 0.5 °C at Bank Piezometer 1. Thermal conduction between the atmosphere and land cannot explain the observed temperature oscillations. Given a typical thermal diffusivity of $7 \times 10^{-7} \text{ m}^2/\text{s}$ for saturated sediment, a 24-hour atmospheric temperature signal would only penetrate 0.25 m into the ground. In unsaturated sediment, the penetration depth is even less. All temperature sensors were located more than a meter below land surface. Although coupled fluid flow and heat transport simulations are beyond the scope of this paper, I suggest that thermal advection associated with hyporheic exchange influences the temperature signal near the channel. In the absence of dam operations, the flow of groundwater to the river would stabilize temperatures near the channel.

Finally, dam operations may impact river temperature by periodically interrupting the flow of groundwater to the river. Groundwater discharge locally buffers temperature in the channel, creating thermal refuges for fish [Arrigoni *et al.*, 2008]. At Hornsby Bend, groundwater only discharges to the river in between dam releases. In unregulated, baseflow-dominated rivers, continuous groundwater discharge would potentially provide more persistent thermal refuges in the channel.

6.7. CONCLUSIONS AND RECOMMENDATIONS

At Hornsby Bend, dam operations pump river water in and out of the riparian aquifer daily. Flow paths that begin and end in the river form a hyporheic zone that extends approximately 1 to 5 m into the riparian aquifer. The daily volume of water that passes through the hyporheic zone is 1 m^3 per meter of bank. To my knowledge, this is the first study to estimate these metrics for lateral hyporheic exchange due to dam operations. The same method could be used to characterize hyporheic exchange due to any frequent river stage fluctuation.

Worldwide, over half of all large rivers are regulated by dams [Nilsson *et al.*, 2005]. A clear direction for future research is to characterize how the hyporheic response to dam operations influences thermal budgets, biogeochemistry, and ecology at both the reach scale and watershed scale. For example, how do flow reversals in the riparian aquifer impact redox conditions and biogeochemical zonation? What is the resulting impact on solute transport at the watershed scale? Are steady or oscillating groundwater flows more beneficial to the biogeochemistry and ecology of rivers, and under what conditions? Investigating the answers to these fundamental questions will help assess the impact of dams on watershed health.

<i>Variable</i>	<i>THE GILL MODEL: Baseflow-dominated rivers</i>	<i>THE LUNG MODEL: Rivers influenced by dam operations</i>
Water table variation	Moderate to small	Rapid, large fluctuations
Hydrologic link to river	Continuous groundwater flow toward river Flood events can temporarily perturb flow paths and rates	Flow directions regularly reverse over short timescales
Hyporheic zone characteristics	Laterally limited by groundwater discharge to the river Flows driven by bedform topography, river morphology, and instream structures Flows are generally steady but may vary in response to floods, seasons, and morphodynamics	Large lateral extent Flows driven by river stage fluctuations downstream of dams Flows are unsteady and reverse at timescales of hours to days
Example of effects on river temperature	Hyporheic and groundwater inputs constantly buffer river temperatures	Hyporheic flows may buffer river temperatures, depending on timing of flow reversals relative to river temperature oscillations Hyporheic flows only influence river temperatures when flow direction is toward river
Example of effects on riparian aquifer temperature	Temperatures vary spatially along flow paths as a function of advection and conduction Temperatures vary temporally over a wide range of timescales, from hours to seasons	Near the channel, temperatures fluctuate over short timescales in response to river stage and temperature Fluctuations decrease in amplitude with distance from channel
Example of effects on river chemistry	Retention of NO ₃ and SO ₄ ; source of DOC	Uncertain but likely a function of competition between kinetics, flow rates, and local groundwater chemistry
Example of effects on riparian aquifer chemistry	Variation in redox conditions with distance along groundwater flow paths	Uncertain but likely variable in both time and space

TABLE 6.1: CONCEPTUAL MODEL OF IMPACT OF DAM OPERATIONS on a river-groundwater system dominated by baseflow, modified after *Hill* [2000].

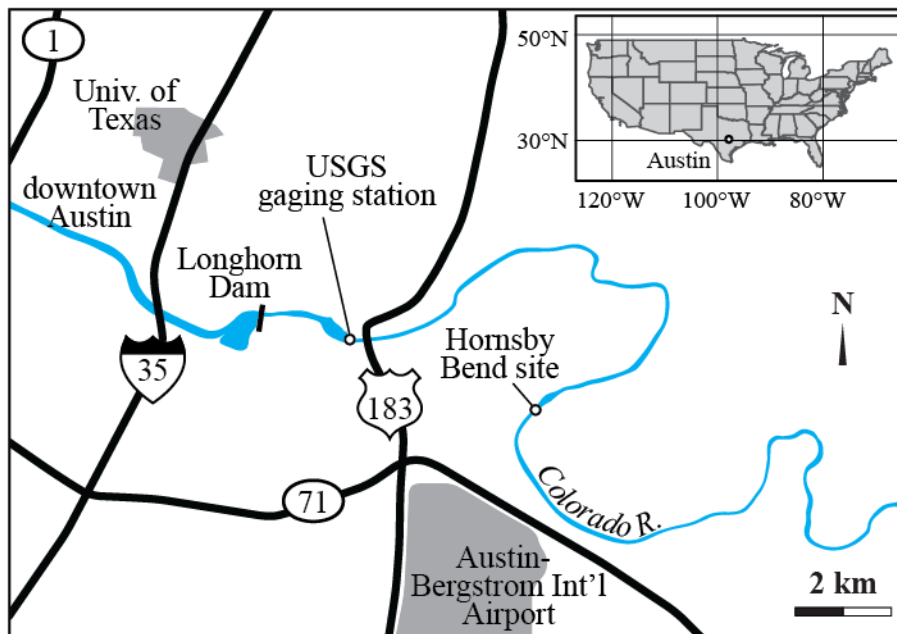


Figure 6.1: Location of study site on the Colorado River in relation to Austin, Texas, USA. USGS gaging station 08158000 is 2 km downstream from Longhorn Dam, and the study site is another 13 km downstream.

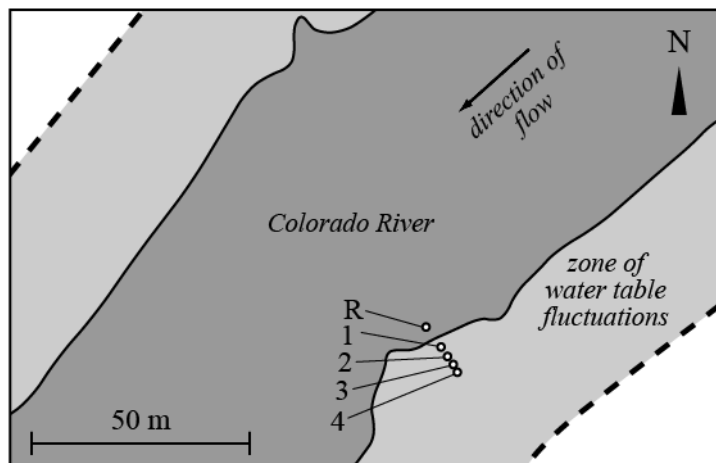


Figure 6.2: Map of Hornsby Bend piezometer transect. Bank piezometers are numbered in order of distance from the river, and the river stage recorder is denoted as (R). Dashed lines indicate the estimated extent of dam influence on the water table.

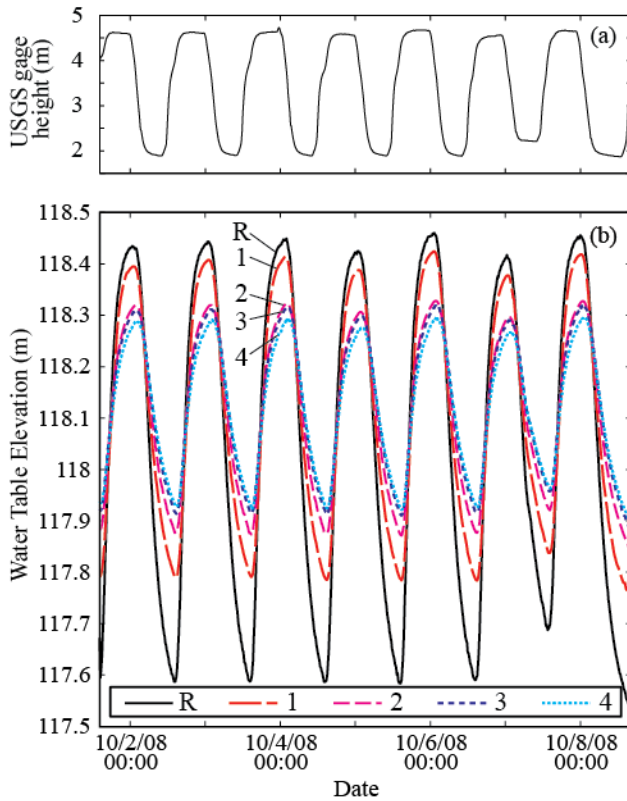


Figure 6.3: Continuous USGS stream gage record from the Colorado River near Austin, Texas from October 1, 2008 at 14:15 to October 8, 2008 at 16:15 (a). The gaging station is located 2 km downstream from Longhorn Dam, and river stage fluctuates 2.5 m daily. Water table elevation time series (b) at the study site. Distances of Bank Piezometers 1 – 4 from mean shoreline are 2.35 m, 5.08 m, 7.43 m, and 9.48 m, respectively. The study site is 15 km downstream from Longhorn Dam, and river stage fluctuates 85 cm daily. Water table fluctuations are attenuated and lagged relative to river stage fluctuations.

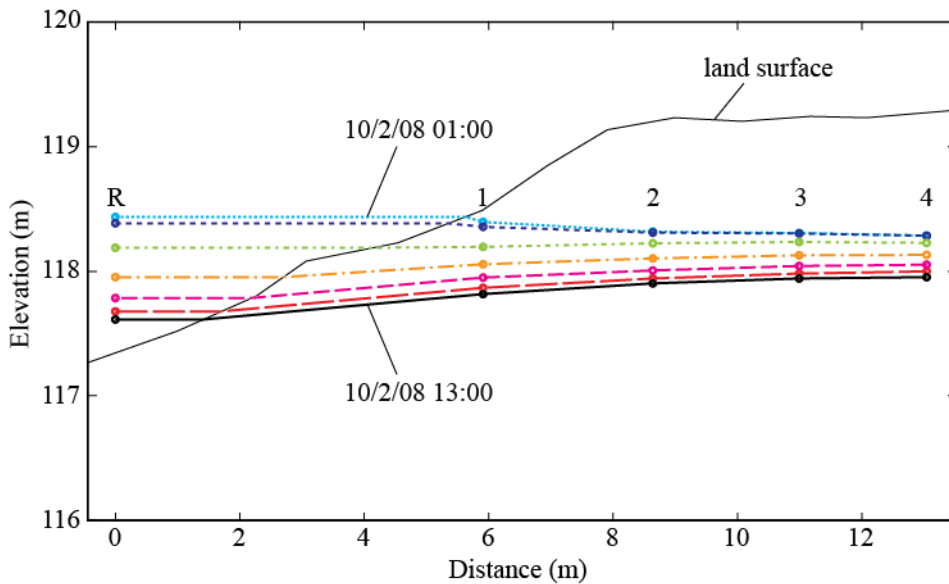


Figure 6.4: Water table elevation profiles at two-hour intervals over a period of twelve hours beginning on October 2, 2008 at 01:00. Land surface profile is also shown. Water table fluctuations dissipate with distance from the river.

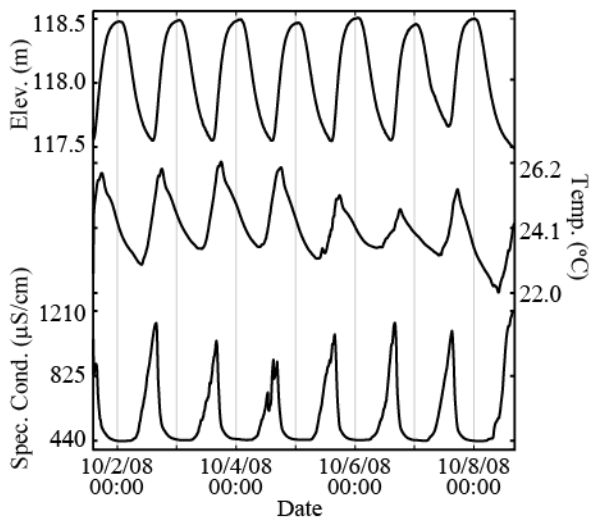


Figure 6.5: River stage, temperature, and specific conductivity time series. Temperature peaks in the early evening. Specific conductivity maxima coincide with river stage minima.

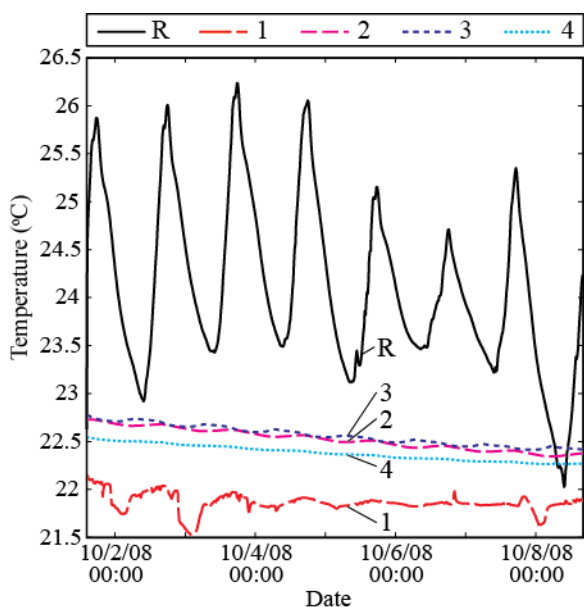


Figure 6.6: Temperature time series in the river stage recorder and four bank piezometers. Distances of Bank Piezometers 1 – 4 from mean shoreline are 2.35 m, 5.08 m, 7.43 m, and 9.48 m, respectively. Temperature fluctuations in Bank Piezometer 1 are attenuated relative to temperature fluctuations in the river. Temperatures at the other bank piezometers are more stable.

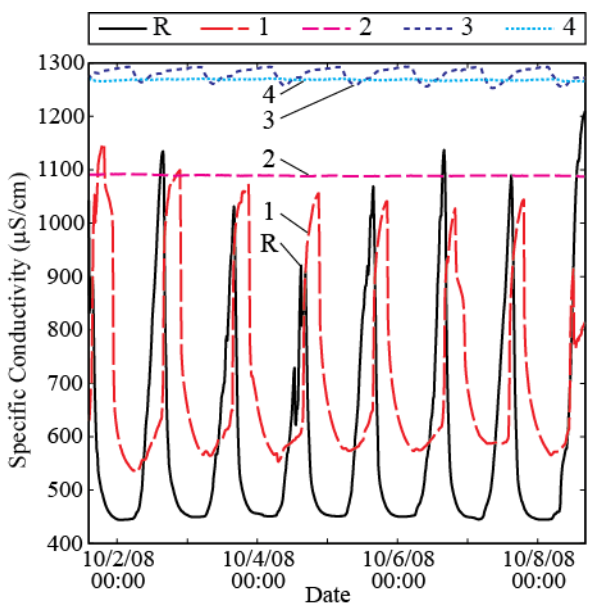


Figure 6.7: Specific conductivity time series in the river stage recorder and four bank piezometers. Distances of Bank Piezometers 1 – 4 from mean shoreline are 2.35 m, 5.08 m, 7.43 m, and 9.48 m, respectively. Fluctuations are greatest at Bank Piezometer 1. Specific conductivity in Bank Piezometer 2 remained stable, likely due to mud on the sensor that we observed during retrieval.

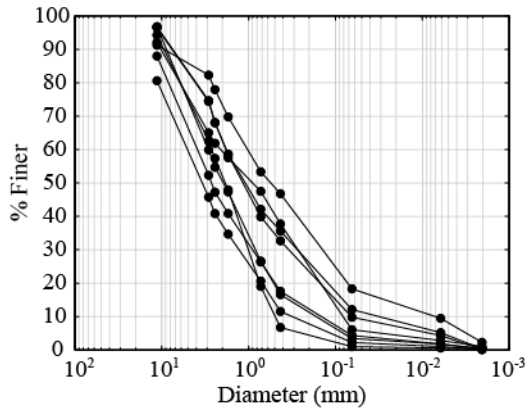


Figure 6.8: Grain size distributions for aquifer sediment samples. The samples are predominantly sandy, although we also collected cobble-dominated samples that were too coarse for dry-sieving.

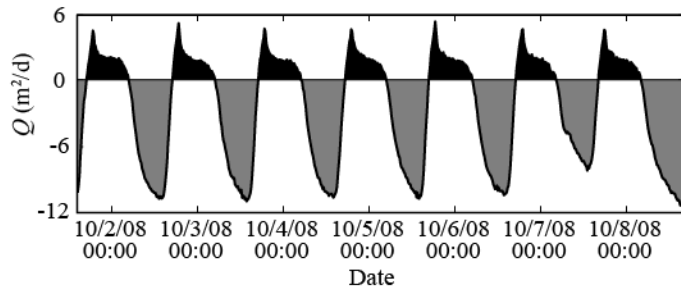


Figure 6.9: Volumetric flow rate between the river and riparian aquifer per meter of bank. Positive values indicate flow from the channel into the bank. The black shaded area represents the volume of water pumped through the hyporheic zone per meter of bank over the duration of the study. The gray shaded area represents the total volume of water discharged into the river (both hyporheic water and baseflow).

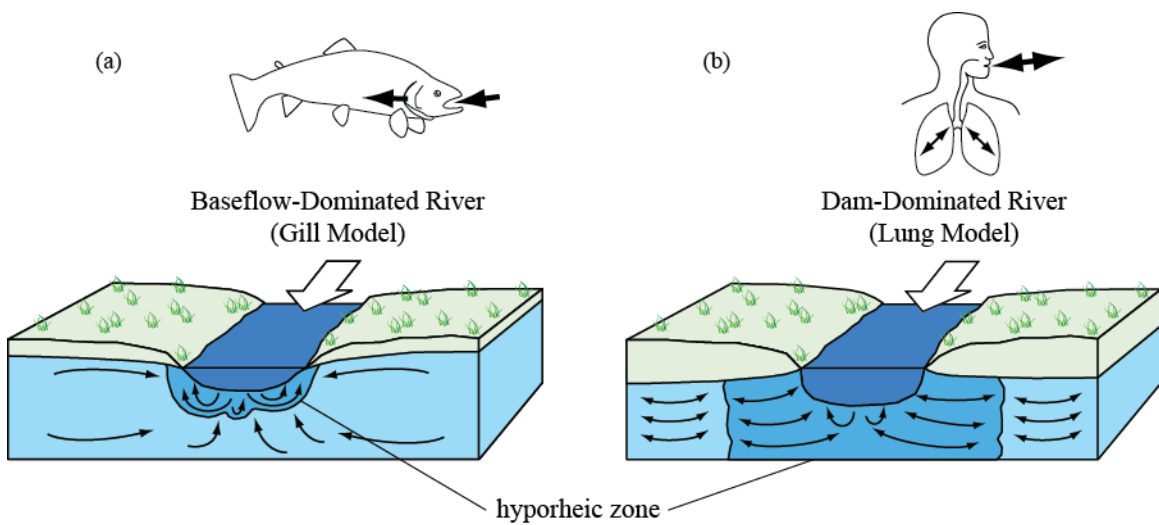


Figure 6.10: Conceptual model of a natural river-groundwater system in a reach dominated by baseflow (a). During most of the year, groundwater flows steadily through the riparian aquifer in one direction like water through a gill. Groundwater discharge to the river limits the size of the hyporheic zone. Conceptual model of a river-groundwater system downstream of a dam (b). Due to frequent stage fluctuations, river water flows in and out of the riparian aquifer like air flowing in and out of lungs. The hyporheic zone includes all flow paths that start and end in the channel.

Chapter 7: Summary

7.1. SYNTHESIS

Hyporheic exchange connects rivers with surrounding aquifers, facilitating the transfer of dissolved solutes and heat between surface water and groundwater. The spatial and temporal complexity of hyporheic exchange is due to the large variability of riverbed sediment permeability and the dynamic, turbulent nature of fluid flow in the adjacent channel. Measurements and models of hyporheic zone processes inevitably fail to capture all length scales and time scales of exchange and the mechanisms that drive them. Nevertheless, the driving forces for hyporheic exchange can be reduced in many river settings to three categories: fluctuations in hydraulic head at the sediment-water interface, spatial variations in hydraulic gradients at the sediment-water interface, and spatial variations in permeability. This thesis addresses all three mechanisms using numerical models, laboratory flume experiments, and field observations in environments ranging from mountain meadow streams to large, regulated rivers.

An underlying theme of this thesis is the vulnerability of hyporheic processes to human interference. Humans have drastically modified stage dynamics in regulated rivers. Where dams regularly release water to generate hydroelectric power, the resulting stage fluctuations increase hyporheic exchange. Where dams retain water and diminish natural stage fluctuations, hyporheic exchange may decrease [*Ward and Stanford, 1995*]. Humans have also influenced hydraulic gradients by removing wood debris and other channel obstructions and straightening channels. The resulting smoothness in modern hydraulic gradients decreases hyporheic exchange. Finally, modern land use practices have led to increased siltation and clogging of riverbed sediment. The resulting decline in average sediment permeability and its spatial variability also reduces hyporheic

exchange [Boulton, 2007]. Modern restoration efforts are attempting to address many of these issues by removing dams, reintroducing wood debris, and controlling fine sediment transport [Hester and Gooseff, 2010], but more research is needed to support restoration design.

7.2. KEY FINDINGS AND FUTURE WORK

I showed that hyporheic exchange increases with LWD blockage, channel Froude number, and sediment permeability for the simple case of channel-spanning logs. Future studies should explore hyporheic exchange due to more complex LWD configurations. For example, an in-stream root would likely drive rapid and multi-dimensional exchange.

I also showed that permeability heterogeneity influences hyporheic exchange through bedforms but did not explore the effects on exchange near LWD. Substrate type and grain size distributions often vary in response to LWD. In lowland rivers, LWD traps fine sediment. The resulting heterogeneity in permeability may complicate hyporheic exchange patterns. If accumulations of fine sediment sufficiently reduce permeability, the net effect of LWD may be to reduce rather than increase river-groundwater connectivity over long timescales. In mountain streams, LWD forces alluvial reaches [Montgomery *et al.*, 1996]. The shift from bedrock to alluvial substrate creates a hyporheic zone, but the net effect on broader patterns of river-groundwater exchange is uncertain. Future research should explore how these long-term trends in substrate type impact hyporheic exchange due to LWD.

At the reach scale, I showed that LWD did not significantly affect transient solute storage in a mountain meadow stream, but tracer tests were not sensitive to local changes in hyporheic exchange. Future studies should continue to explore relationships between transient solute storage metrics and hyporheic processes. Another important area for

research is to assess optimal LWD densities and diameters for maximizing hyporheic exchange at the reach scale.

Because LWD locally increases hyporheic exchange, it presumably increases the delivery of dissolved oxygen, nitrogen species, and organic carbon to microbial communities within the sediment, potentially enhancing nutrient uptake. In light of anthropogenic nitrogen and phosphorus loading in watersheds, future studies should examine how LWD controls nitrogen uptake and phosphorus trapping. A particularly interesting question is whether LWD reintroduction can enhance nitrogen removal in nitrogen-rich streams.

Finally, I showed that rapid river stage fluctuations drive significant hyporheic exchange in the banks of large rivers. Because stage fluctuations create steep but ephemeral hydraulic gradients, they are an important yet understudied mechanism for driving river-groundwater connectivity. Stage fluctuations likely account for most hyporheic exchange in rivers subject to regular dam releases, diel snowmelt, or convective summertime storms. Future studies should quantify exchange rates in these rivers and assess the implications for heat budgets, nutrient and contaminant transport, and best management practices.

Appendices

APPENDIX A1: SCALING ANALYSIS

Here, I show from first principles how the head drop due to flow around a log should scale with blockage ratio and Froude Number. Consider energy at two locations: the log center where the flow constriction is maximized, and far upstream. Energy conservation for an inviscid, incompressible, irrotational fluid subject to gravity at these two locations leads to the Bernoulli equation:

$$\frac{v_{upstrm}^2}{2g} + h_{upstrm} = \frac{v_{log}^2}{2g} + h_{log}, \quad (\text{A1.1})$$

where h is hydraulic head, which is assumed to vary only in the downstream direction, and v is mean flow velocity. Conservation of mass requires:

$$v_{upstrm} d_{upstrm} = v_{log} d_{log}, \quad (\text{A1.2})$$

where d is flow thickness. Noting that $B = d_{log}/d_{upstrm}$ and combining (A1.1) with (A1.2) yields:

$$h_{upstrm} - h_{log} = \frac{1}{2} \frac{v_{upstrm}^2}{g} \left[\left(\frac{1}{1-B} \right)^2 - 1 \right]. \quad (\text{A1.3})$$

Dividing by d_{upstrm} and noting that $Fr^2 = v_{upstrm}^2/gd_{upstrm}$:

$$\frac{h_1}{d} = \frac{1}{2} Fr^2 \left[\left(\frac{1}{1-B} \right)^2 - 1 \right], \quad (\text{A1.4})$$

where h_1 is $h_{upstrm} - h_{log}$ and d is d_{upstrm} . For an inviscid, irrotational flow subject to no drag, h_1/d should increase with the square of the Froude number and approach infinity as blockage ratio approaches unity. Equation A1.4 resembles empirically developed scaling in Equation 3.10.

APPENDIX A2: MANUAL FOR RECIRCULATING FLUME

A2.1. Flume-o-matic panel

The flume-o-matic panel is the gray wall unit that controls power to the flume pumps, heater/chiller, and other power-drawing parts (Figure A2.1). To turn on the power, switch the “panel power” on. Then turn on the red power switch on the right face of the panel.



Figure A2.1: Flume-o-matic panel and power controls.

The other panel switches determine whether the flume receives commands manually through the panel or automatically through the software (Figure A2.2). When running an experiment in the flume, all switches should be set to “auto,” except for the tilt angle, which must always be set to “hand.” When draining the flume, all switches must be set to “0” or “off” (except for the two main power switches). The tilt angle does not have an off position and should remain on the “hand” setting.



Figure A2.2: Control panel settings. In general, all controls should be set to “auto” except the tilt angle. When the flume is draining, these controls must be set to “0” or “off.”

A2.2. Navigating the software

To open the flume software, double click the “RSView 32 Runtime” icon on the desktop. Log on using “ut” as the username and “utpw” as the password.

The “Overview” page is the home page that summarizes flume activity (Figure A2.3). If you don’t see this page, click the Overview tab at the bottom left of the screen and select “Overview.” This page displays the following important information:

- whether the flume is currently running (online or offline),
- whether the flume is in Mode 1 or 2,
- whether the scheduler is enabled,
- flow rate and temperature “setpoints” (programmed values),
- actual flow rate and temperature values,
- status of control and isolation valves, heat exchanger, and pumps.

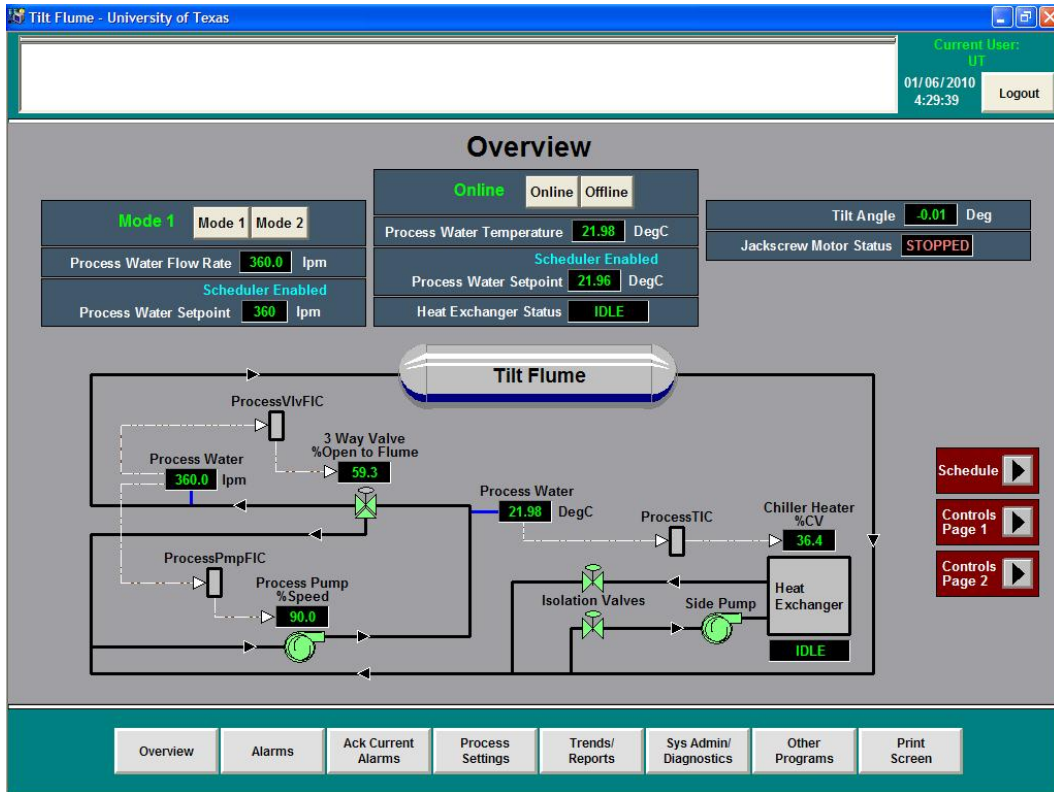


Figure A2.3: The Overview page displays information about current flume settings.

From the tabs on the right of the Overview page, you can also access the Schedule and Controls pages. The Schedule page allows you to program temperatures and flow rates. The Controls pages provide more details about how the flume is operating at any given time.

The bottom row of tabs represents the menu and is accessible from any page in the software. Below is a brief description of important menu items.

- Overview: the home page,
- Alarms: a page for viewing and resetting alarms,
- Ack Current Alarms: a short-cut tab for acknowledging an alarm,
- Process Settings: provides access to Schedule and Controls pages (note that you can also access these from the right side of the Overview page),

- Trends/Reports: provides access to graphs and tables of data and displays the readme file, which decodes alarms and parameter names,
- Sys Admin/Diagnostics: for managing user accounts,
- Other Programs: provides access to other software (note that you can also access other software through Start → All Programs).

A2.3. Modes 1 and 2

The flume has two modes of operation. In Mode 1, temperature control is enabled. The Chiller/Heater will heat or cool water as it recirculates through the side loop to achieve the programmed temperature for the surface water, also called “process water.” In Mode 2, temperature control is not enabled. The isolation valves close to separate the side loop from the main recirculation loop. This design prevents the side loop from acting as a reservoir or transient storage zone during tracer tests when temperature control is not desired.

To toggle between modes, turn the flume offline by navigating to the Overview Page and clicking “Offline.” Next, on the Overview page, select either “Mode 1” or “Mode 2.” Turn the flume online again if desired.

A2.4. Manual and automatic operation

The flume can be controlled manually through the tilt-o-matic panel (“hand” setting on the panel) or automatically through the software (“auto” setting on panel). The tilt angle must always be controlled manually rather than through the software to avoid damaging the jack. Because of communication delays with the software, it is possible to accidentally lower the tilt to negative values using the software, which can destroy the jack. To manually control the tilt angle, use the dial on the flume-o-matic to raise or lower the tilt. Never lower the tilt below zero degrees.

All other parameters should typically be controlled through the software. The software can be used to control the flume automatically in two ways: through the Schedule page, or through the Controls page (if the scheduler is disabled). In either case, all parameters on the Controls pages should be set to “Program.” Automatic control will not work if any of the parameters are set to “Operator.”

When programming the flume, the Schedule is the recommended approach for controlling flow rate and temperature (rather than the Controls). To access the Schedule page, click on “Process Settings” at the bottom of the page and select “Schedule.” If the Schedule is enabled, it will control the flow rate and temperature. If the Schedule is disabled, the Controls pages control the flow rate and temperature.

To use the Schedule in Mode 2 (flow control only), enter the desired flow rate(s) in L/min, the duration of the period(s) in hours, and click on the “disabled” button to enable each period (Figure A2.4). Hit the return key on the keyboard after entering each number in the Schedule, or else the entries will not be accepted. If a constant flow rate is desired, only one flow period is necessary because the flow periods loop continuously. To access more than five periods, click the “next” button. The active period and period timer control the current position within the scheduled flow loop (note that the period timer runs when the Schedule is enabled, even if the flume is offline). When the Schedule is enabled and the flume is turned online, it will begin in the active period (so the active period should be set to “1” if that is the desired starting point). To jump to a new active period, type a number in the window and hit the return key. Note that temperature periods cannot be programmed when the flume is in Mode 2.

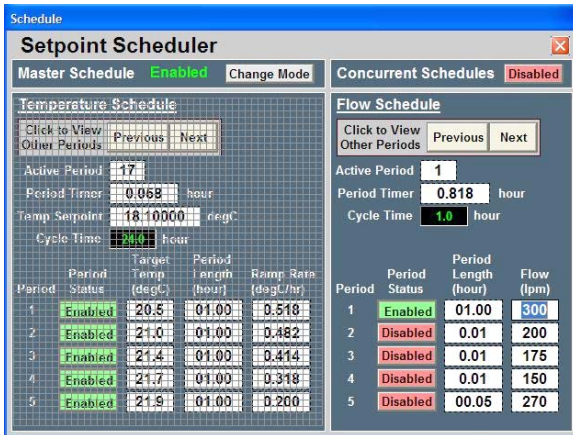


Figure A2.4: Schedule page in Mode 2 (no temperature control).

To use the Schedule in Mode 1 (flow and temperature control), enter the desired flow rate(s) in L/min and temperature(s) in degrees Celsius, the duration of the period(s) in hours, and hit “disabled” to enable them (Figure A2.5). Hit the return key on the keyboard after each entry in the Schedule, or else the entries will not be accepted. The ramp rate allows you to program a (linear) time rate of change to transition from one temperature set point to the next. The software will only accept positive values. The temperature will increase or decrease linearly depending on whether the next set point is greater than or less than the current set point. To access more than five periods, hit the “next” button.

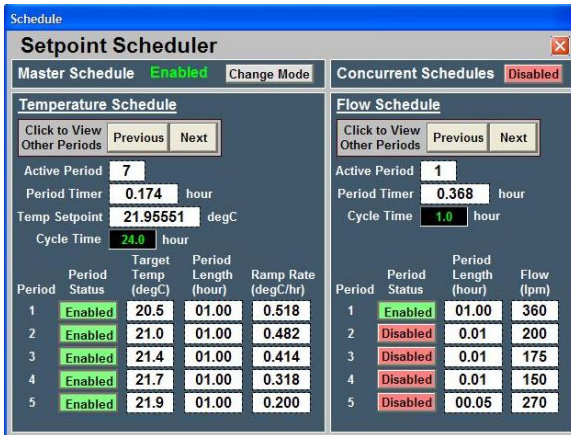


Figure A2.5: Schedule page in Mode 1 (temperature control) without concurrent schedules.

If “Concurrent Schedules” is disabled, the temperature and flow periods loop independently (as in Figure A2.5). If “Concurrent Schedules” is enabled, temperature and flow periods step concurrently (Figure A2.6). In that case, the number and duration of temperature and flow periods must coincide. For information on the active period and period timer, see the previous paragraph.

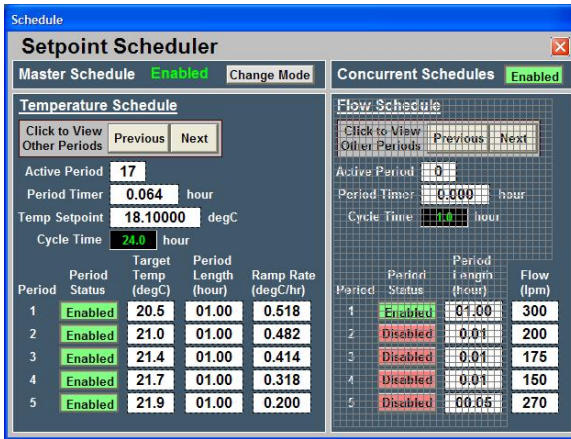


Figure A2.6: Schedule page in Mode 1 (temperature control) with concurrent schedules. Flow rate and temperature periods are synchronized.

A2.5. Viewing and Saving Data

Data can be viewed in table or graph form. To plot a graph, select “Trends” from the bottom menu and click “Historical Trending.” Click on “Flow Loop PID Tune” to view flow rate versus time or “Temp Loop PID Tune” to view temperature versus time. Select the range of times on the x-axis by clicking “24 hr span,” for example. The y-axis displays values for the parameter(s) highlighted in the legend. To display y-axis values for a different parameter, click on that parameter’s symbol within the legend. “Auto scale” automatically scales the y axis. To rescale manually, click “Min / Max Scale” and hold the mouse over an axis. Then click and drag to resize. You can change the symbols for each parameter under “Pen selection and properties.”

To view data in table form, go to Trends → Process Data. Similarly, you can view the alarms that have occurred in table form by selecting “Alarm History” under “Trends.” Alternatively, you can view a journal of events (operations) by selecting “Event History.”

All information that can be plotted or viewed as tables is also saved in log files in the F: directory. New log files can be created any time a new schedule is started. The alternative is to continue appending data to the current log files. To create new log files, click “Change Mode” in the top left section of the Schedule page. Select “Enable schedule and create new logging file” (Figure A2.7).

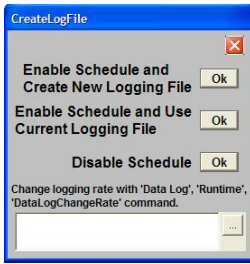


Figure A2.7: Create new log files for flume settings, operations, and alarms under the Schedule page.

A2.6. Alarms

Alarms commonly occur in normal flume operation (for example, when the flume is turned off or drained). When some alarms occur, the flume will not start until the alarms are acknowledged and unlatched. To acknowledge alarms, click on “Ack current alarms” on the bottom tab of the screen, or go to the “Alarms” page and acknowledge alarms there. Next, go to the Controls page. If any red flags exist, click “Unlatch” (Figure A2.8). Look for flags in both Controls Page 1 and 2. The flume should now be ready to start. If not, see the trouble-shooting section of this manual.

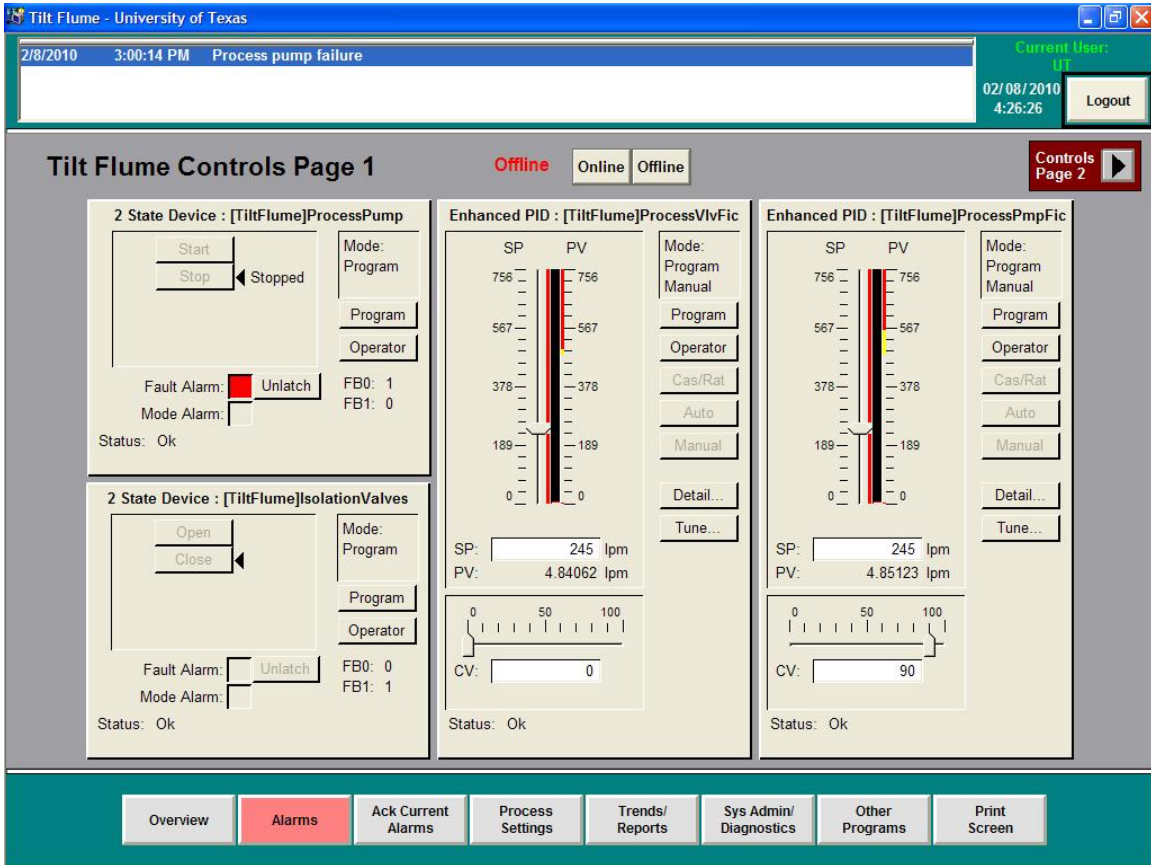


Figure A2.8: View of Controls Page 1 after alarm. To clear alarm, first acknowledge (“Ack Current Alarms” and then click “Unlatch” next to any red flags on Controls Pages. Once all alarms are acknowledged and unlatched, the “Alarms” button will return to the normal gray color, indicating that all alarms have successfully been cleared. Note the Controls Pages can also be used to set options such as flow rates by manually entering SP values if the following three things are true: 1) flume-o-matic panel is on automatic, 2) Modes in Controls Pages are set to Program, and 3) the Scheduler is disabled.

A2.7. Example Procedures

This section provides general steps for filling the flume, starting a flume program, shutting down the flume, and draining it. For more detailed descriptions of each step, see previous sections.

Filling flume: Make sure both drainage valves are closed. Drainage valves are red and are located on the side loop and sediment section near the downstream end of the flume (Figure A2.9). In the software, turn the flume offline. If switches on flume-o-matic panel are set to zero, manual, or off, turn them to auto or on. Fill the flume by placing hose in the downstream reservoir.

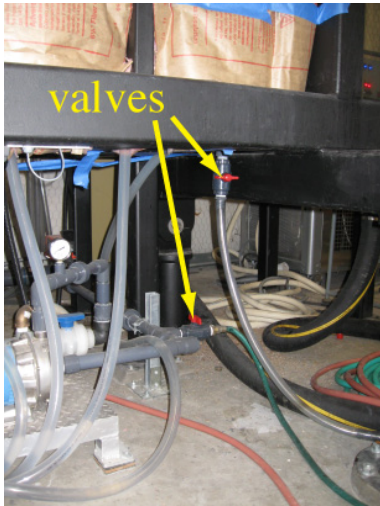


Figure A2.9: Location of drainage valves.

Starting flume program: If necessary, clear alarms in software. On the Overview page, select Mode 1 or 2, depending on whether temperature control is desired. Go to the Schedule page to program the flow rate and/or temperature. If desired, create a new log file upon enabling the schedule. Turn the flume online.

Shutting down flume: Turn the flume offline. If desired, copy log files from the F: directory.

Draining flume: Turn all controls on flume-o-matic to zero or manual. Choose Mode 1 and turn flume online. This prevents the pump from running but opens isolation valves so that the flume can drain. Open red valve on side loop and red valve below

sediment section on downstream end (Figure A2.9). Both valves connect to tubes that extend to the floor drain.

A2.8. Maintenance

Water level: Evaporation causes the water level in the flume to drop slowly during experiments. A good rule of practice is to add water to the flume at least once a day to maintain a constant water level during experiments.

Heater/Chiller: The antifreeze level should be checked regularly when running experiments in Mode 1. If the liquid level falls more than an inch below the black line on the tube of the heater/chiller, refill with 60% ethylene glycol and 40% water by volume. Ethyl Glycol Type 1 can be purchase through Capital Scientific in Austin.

Draining flume: To drain flume, turn all controls on flume-o-matic to zero or manual. Choose Mode 1 and turn flume online. This prevents the pump from running but opens the isolation valves so that the flume can drain. Open red valve on side loop and red valve below sediment section on downstream end. Both valves connect to tubes that extend to the floor drain.

Screens and marble cage: Maintain screens and marble cage at flume inlet and outlet. These prevent large sediment from recirculating and destroying the pump. Use silicone glue if screen needs replacing.

Algal growth: About ¼ to ½ cup bleach can be added to the flume while water is recirculating to kill algae and stop odors (after bleach use, drain flume, refill with fresh water, and drain again before conducting experiments with rhodamine or other tracers).

A2.9. Trouble-shooting

1. The pump on the flume does not start.

The pump may take a long time to start if air is in the plumbing. Keep the flume online until air is purged from the plumbing. Consider turning the flume off for a few seconds and then back on again if air doesn't purge after a few minutes.

2. The alarms do not unlatch.

Go to the Alarms page and acknowledge all alarms. Then go to the Controls pages and verify that all modes are set to program rather than operator. Unlatch all red flags in both Controls Page 1 and Controls Page 2. You should now be able to start the flume.

3. The flume does not achieve the desired flow rate.

The maximum flow rate for this pump is about 640-650 L/min. Occasionally, the flume won't achieve a new flow rate. If this occurs, go to Controls Page 1 and check the ProcessVlvFic and ProcessPmpFic readings (in particular, the PV and CV readings). Then click on "Detail" under both ProcessVlvFic and ProcessPmpFic and check the maximum and minimum settings (LoLo and HiHi Limits). If the PV or CV on the Controls page is currently pegged at the maximum or minimum limit in the Details window, adjust the limits in the Details window so that the flume can achieve a wider range of valve openings or flow rates. At the end of the experiment, return these settings to their original (recommended) values.

References

- Abbe, T. B., and D. R. Montgomery (1996), Large woody debris jams, channel hydraulics and habitat formation in large rivers, *Regulated Rivers-Research & Management*, 12, 2-3, 201-221.
- Allen, J. R. (1971), A theoretical and experimental study of climbing-ripple cross-lamination, with a field application to the Uppsala Esker, *Geografiska Annaler. Series A, Physical Geography*, 53, 3/4, 157-187.
- Angermeier, P. L., and J. R. Karr (1984), Relationships between woody debris and fish habitat in a small warmwater stream, *Trans. Am. Fish. Soc.*, 113, 716-726.
- Arntzen, E. V., D. R. Geist, and P. E. Dresel (2006), Effects of fluctuating river flow on groundwater/surface water mixing in the hyporheic zone of a regulated, large cobble bed river, *River Research and Applications*, 22, doi: 10.1002/rra.947.
- Arrigoni, A. S., G. C. Poole, L. A. K. Mertes, S. J. O'Daniel, W. W. Woessner, and S. A. Thomas (2008), Buffered, lagged, or cooled? Disentangling hyporheic influences on temperature cycles in stream channels, *Water Resour. Res.*, 44, W09418, doi: 10.1029/2007WR006480.
- Arscott, D. B., K. Tockner, and J. V. Ward (2001), Thermal heterogeneity along a braided floodplain river (Tagliamento River, northeastern Italy), *Can. J. Fish. Aquat. Sci.*, 58, doi: 10.1139/cjfas-58-12-2359.
- Battin, T. J., L. A. Kaplan, S. Findlay, C. S. Hopkinson, E. Marti, A. I. Packman, J. D. Newbold, and F. Sabater (2008), Biophysical controls on organic carbon fluxes in fluvial networks, *Nature Geoscience*, 1, 2, doi: 10.1038/ngeo101.
- Baxter, C. V., and F. R. Hauer (2000), Geomorphology, hyporheic exchange, and selection of spawning habitat by bull trout (*Salvelinus confluentus*), *Can. J. Fish. Aquat. Sci.*, 57, 1470-1481.
- Bearman, P. W., and M. M. Zdravkovich (1978), Flow around a circular cylinder near a plane boundary, *Journal of Fluid Mechanics*, 89, 1, 33-47.
- Bilby, R. E. (1981), Role of organic debris dams in regulating the export of dissolved and particulate matter from a forested watershed, *Ecology*, 62, 5, 1234-1243.
- Bilby, R. E., and G. E. Likens (1980), Importance of organic debris dams in the structure and function of stream ecosystems, *Ecology*, 61, 5, 1107-1113.

- Boano, F., C. Camporeale, R. Revelli, and L. Ridolfi (2006), Sinuosity-driven hyporheic exchange in meandering rivers, *Geophys. Res. Lett.*, *33*, L18406, doi: 10.1029/2006GL027630.
- Boano, F., A. I. Packman, A. Cortis, R. Revelli, and L. Ridolfi (2007), A continuous time random walk approach to the stream transport of solutes, *Water Resour. Res.*, *43*, W10425, doi: 10.1029/2007WR006062.
- Boano, F., D. Poggi, R. Revelli, and L. Ridolfi (2009), Gravity-driven water exchange between streams and hyporheic zones, *Geophys. Res. Lett.*, *36*, L20402, doi: 10.1029/2009GL040147.
- Boano, F., R. Revelli, and L. Ridolfi (2008), Reduction of the hyporheic zone volume due to the stream-aquifer interaction, *Geophys. Res. Lett.*, *35*, doi: 10.1029/2008GL033554.
- Boulton, A. J. (2007), Hyporheic rehabilitation in rivers: Restoring vertical connectivity, *Freshwater Biology*, *52*, 632-350.
- Bouwer, H., and R. C. Rice (1976), A slug test method for determining hydraulic conductivity of unconfined aquifers with completely or partially penetrating wells, *Water Resour. Res.*, *12*, 3, 423-428.
- Bowen, B. M. (1996), Rainfall and climate variation over a sloping New Mexico plateau during the North American monsoon, *Journal of Climate*, *9*, 12, 3432-3442.
- Braudrick, C. A., and G. E. Grant (2000), When do logs move in rivers?, *Water Resour. Res.*, *36*, 2, 571-583.
- Brown, J. H., J. F. Gillooly, A. P. Allen, V. M. Savage, and G. B. West (2004), Toward a metabolic theory of ecology, *Ecology*, *85*, 7, 1771-1789.
- Brunke, M., and T. Gonser (1997), The ecological significance of exchange processes between rivers and groundwater, *Freshwater Biology*, *37*, 1-33.
- Cardenas, M. B. (2007), Potential contribution of topography-driven regional groundwater flow to fractal stream chemistry: Residence time distribution analysis of Tóth flow, *Geophys. Res. Lett.*, *34*, doi: 10.1029/2006GL029126.
- Cardenas, M. B. (2009), Stream-aquifer interactions and hyporheic exchange in gaining and losing sinuous streams, *Water Resour. Res.*, *45*, W06429, doi: 10.1029/2008wr007651.
- Cardenas, M. B., and J. L. Wilson (2007a), Dunes, turbulent eddies, and interfacial exchange with permeable sediments, *Water Resour. Res.*, *43*, W08412, doi: 10.1029/2006WR005787.

- Cardenas, M. B., and J. L. Wilson (2007b), Effects of current-bed form induced fluid flow on the thermal regime of sediments, *Water Resour. Res.*, *43*, W08431, doi: 10.1029/2006wr005343.
- Cardenas, M. B., and J. L. Wilson (2007c), Exchange across a sediment-water interface with ambient groundwater discharge, *J. Hydrol.*, *346*, 3-4, doi: 10.1016/j.jhydrol.2007.08.019.
- Cardenas, M. B., and J. L. Wilson (2007d), Thermal regime of dune-covered sediments under gaining and losing water bodies, *Journal of Geophysical Research-Biogeosciences*, *112*, G4, G04013, doi: 10.1029/2007jg000485.
- Cardenas, M. B., J. L. Wilson, and R. Haggerty (2008), Residence time of bedform-driven hyporheic exchange, *Advances in Water Resources*, *31*, doi: 10.1016/j.advwatres.2008.07.006.
- Cardenas, M. B., J. L. Wilson, and V. A. Zlotnik (2004), Impact of heterogeneity, bed forms, and stream curvature on subchannel hyporheic exchange, *Water Resour. Res.*, *40*, W08307, doi: 10.1029/2004WR003008.
- Cardenas, M. B., and V. A. Zlotnik (2003a), A simple constant-head injection test for streambed hydraulic conductivity estimation, *Ground Water*, *41*, 6, 867-871.
- Cardenas, M. B., and V. A. Zlotnik (2003b), Three-dimensional model of modern channel bend deposits, *Water Resour. Res.*, *39*, 6, doi: 10.1029/WR001383.
- COMSOL AB (2006), COMSOL Multiphysics User's Guide, COMSOL AB, Burlington, M.A.
- Curran, J. H., and E. E. Wohl (2003), Large woody debris and flow resistance in step-pool channels, Cascade Range, Washington, *Geomorphology*, *51*, 1-3, 141-157.
- Curry, R. A., J. Gehrels, D. L. G. Noakes, and R. Swainson (1994), Effects of river flow fluctuations on groundwater discharge through brook trout, *Salvelinus fontinalis*, spawning and incubation habitats, *Hydrobiologia*, *277*, 121-134.
- Destaso, J., and F. J. Rahel (1994), Influence of water temperature on interactions between juvenile Colorado River cutthroat trout and brook trout in a laboratory stream, *Trans. Am. Fish. Soc.*, *123*, 3, 289-297.
- Deutsch, C. V., and A. G. Journel (1998), *GSLIB: Geostatistical Software Library and User's Guide*, 2 ed., 369 pp., Oxford University Press, New York.
- Durlafsky, L. J. (1991), Numerical calculation of equivalent grid block permeability tensors for heterogeneous porous media, *Water Resour. Res.*, *27*, 5, 699-708.

- Elliott, A. H., and N. H. Brooks (1997a), Transfer of nonsorbing solutes to a streambed with bed forms: Laboratory experiments, *Water Resour. Res.*, 33, 1, 137-151.
- Elliott, A. H., and N. H. Brooks (1997b), Transfer of nonsorbing solutes to a streambed with bed forms: Theory, *Water Resour. Res.*, 33, 1, 123-136.
- Ensign, S. H., and M. W. Doyle (2005), In-channel transient storage and associated nutrient retention: Evidence from experimental manipulations, *Limnology and Oceanography*, 50, 6, 1740-1751.
- Ensign, S. H., and M. W. Doyle (2006), Nutrient spiraling in streams and river networks, *Journal of Geophysical Research-Biogeosciences*, 111, G4, doi: 10.1029/2005jg000114.
- Findlay, S. (1995), Importance of surface-subsurface exchange in stream ecosystems: The hyporheic zone, *Limnology & Oceanography*, 40, 1, 159-164.
- Fischer, H. B. (1975), Simple method for predicting dispersion in streams, *Journal of the Environmental Engineering Division-ASCE*, 101, 3, 453-455.
- Fluent Inc. (2006), FLUENT 6.3 User's Guide, Fluent Incorporated, Lebanon, N.H.
- Freeze, R. A., and J. A. Cherry (1979), *Groundwater*, 604 pp., Prentice-Hall, Englewood Cliffs, NJ.
- Fritz, B. G., and E. V. Arntzen (2007), Effect of rapidly changing river stage on uranium flux through the hyporheic zone, *Ground Water*, 45, 6, doi: 10.1111/j.1745-6584.2007.00365.x.
- Gippel, C. J. (1995), Environmental hydraulics of large woody debris in streams and rivers, *Journal of Environmental Engineering*, 121, 5, 388-395.
- Gooseff, M. N., and B. L. McGlynn (2005), A stream tracer technique employing ionic tracers and specific conductance data applied to the Maimai catchment, New Zealand, *Hydrol. Process.*, 19, 13, doi: 10.1002/hyp.5685.
- Gray, H. H. (1956), Petrology of the Massillon Sandstone at the Type Locality, *Ohio Journal of Science*, 56, 3, 138.
- Greig, S. M., D. A. Sear, and P. A. Carling (2007), A review of factors influencing the availability of dissolved oxygen to incubating salmonid embryos, *Hydrol. Process.*, 21, doi: 10.1002/hyp.6188.
- Gurnell, A. M., H. Piegay, F. J. Swanson, and S. V. Gregory (2002), Large wood and fluvial processes, *Freshwater Biology*, 47, 601-619.

- Haggerty, R., S. M. Wondzell, and M. A. Johnson (2002), Power-law residence time distribution in the hyporheic zone of a 2nd-order mountain stream, *Geophys. Res. Lett.*, 29, 13, doi: 10.1029/2002gl014743.
- Hakenkamp, C. C., A. Morin, and D. L. Strayer (2002), The functional importance of freshwater meiofauna, in *Freshwater Meiofauna: Biology and Ecology*, edited by A. L. R. S.D. Rundle, and J.M. Schmid-Araya, pp. 321-335, Backhuys, Leiden, The Netherlands.
- Hancock, P. J. (2002), Human impacts on the stream-groundwater exchange zone, *Environmental Management*, 29, 6, doi: 10.1007/s00267-001-0064-5.
- Hanrahan, T. P. (2008), Effects of river discharge on hyporheic exchange flows in salmon spawning areas of a large gravel-bed river, *Hydrol. Process.*, 22, doi: 10.1002/hyp.6605.
- Harvey, J. W., and K. E. Bencala (1993), The effect of streambed topography on surface-subsurface water exchange in mountain catchments, *Water Resour. Res.*, 29, 1, 89-98.
- Harvey, J. W., and C. C. Fuller (1998), Effect of enhanced manganese oxidation in the hyporheic zone on basin-scale geochemical mass balance, *Water Resour. Res.*, 34, 4, 623-636.
- Harvey, J. W., and B. J. Wagner (2000), Quantifying hydrologic interactions between streams and their subsurface hyporheic zones, in *Streams and Ground Waters*, edited by J. B. Jones, P.J. Mulholland, pp. 1-43, Academic Press, San Diego, CA.
- Harvey, J. W., B. J. Wagner, and K. E. Bencala (1996), Evaluating the reliability of the stream tracer approach to characterize stream-subsurface water exchange, *Water Resour. Res.*, 32, 8, 2441-2451.
- Hatch, C. E., A. T. Fisher, J. S. Revenaugh, J. Constantz, and C. Ruehl (2006), Quantifying surface water-groundwater interactions using time series analysis of streambed thermal records: Method development, *Water Resour. Res.*, 42, W10410, doi: 10.1029/2005wr004787.
- Hazen, A. (1911), Discussion: Dams on sand foundations: Transactions, *American Society of Civil Engineers*, 73, 199.
- Hering, D., J. Kail, S. Eckert, M. Gerhard, E. Meyer, M. Mutz, M. Reich, and I. Weiss (2000), Coarse woody debris quantity and distribution in Central European streams, *International Review of Hydrobiology*, 85, 1, 5-23.

- Hester, E. T., and M. W. Doyle (2008), In-stream geomorphic structures as drivers of hyporheic exchange, *Water Resour. Res.*, 44, W03417, doi: 10.1029/2006WR005810.
- Hester, E. T., M. W. Doyle, and G. C. Poole (2009), The influence of in-stream structures on summer water temperatures via induced hyporheic exchange, *Limnology and Oceanography*, 54, 1, 355-367.
- Hester, E. T., and M. N. Gooseff (2010), Moving beyond the banks: Hyporheic restoration is fundamental to restoring ecological services and functions of streams, *Environ. Sci. Technol.*, 44, 5, doi: 10.1021/es902988n.
- Hill, A. R. (2000), Stream chemistry and riparian zones, in *Streams and Ground Waters*, edited by J. B. Jones, P.J. Mulholland, pp. 83-110, Academic Press, San Diego.
- Hirt, C. W., and B. D. Nichols (1981), Volume of fluid VOF method for the dynamics of free boundaries, *Journal of Computational Physics*, 39, 201-225.
- Hornberger, G. M., J. Ebert, and I. Remson (1970), Numerical solution of the Boussinesq equation for aquifer-stream interaction, *Water Resour. Res.*, 6, 2, 601-608.
- Huysmans, M., L. Peeters, G. Moermans, and A. Dassargues (2008), Relating small-scale sedimentary structures and permeability in a cross-bedded aquifer, *J. Hydrol.*, 361, doi: 10.1016/j.jhydrol.2008.07.047.
- Johnson, L. B., D. H. Breneman, and C. Richards (2003), Macroinvertebrate community structure and function associated with large wood in low gradient streams, *River Research and Applications*, 19, 3, 199-218.
- Kasahara, T., and A. R. Hill (2006), Effects of riffle-step restoration on hyporheic zone chemistry in N-rich lowland streams, *Can. J. Fish. Aquat. Sci.*, 63, 1, doi: 10.1139/f05-199.
- Kozeny, J. (1927), Uber kapillare leitung des wassers im boden [On capillary flow of water in soil], *Wien, Akad. Wiss.*, 136, 271-306.
- Krause, S., A. Bronstert, and E. Zehe (2007), Groundwater-surface water interactions in a North German lowland floodplain--Implications for the river discharge dynamics and riparian water balance, *J. Hydrol.*, 347, doi: 10.1016/j.jhydrol.2007.09.028.
- Larkin, R. G., and J. M. Sharp (1992), On the relationship between river-basin geomorphology, aquifer hydraulics, and ground-water flow direction in alluvial aquifers, *Geol. Soc. Am. Bull.*, 104, 1608-1620.

- Lautz, L. K., and R. M. Fanelli (2008), Seasonal biogeochemical hotspots in the streambeds around restoration structures, *Biogeochemistry*, doi: 10.1007/s10533-008-9235-2.
- Lautz, L. K., D. I. Siegel, and R. L. Bauer (2006), Impact of debris dams on hyporheic interaction along a semi-arid stream, *Hydrol. Process.*, 20, 183-196.
- Lewandowski, J., G. Lischeid, and G. Nützmann (2009), Drivers of water level fluctuations and hydrological exchange between groundwater and surface water at the lowland River Spree (Germany): Field study and statistical analyses, *Hydrol. Process.*, 23, doi: 10.1002/hyp.7277.
- Liang, D., and L. Cheng (2005), Numerical modeling of flow and scour below a pipeline in currents: Part I. Flow simulation, *Coastal Engineering*, 52, doi: 10.1016/j.coastaleng.2004.09.002.
- Lisle, T. E. (1995), Effects of coarse woody debris and its removal on a channel affected by the 1980 eruption of Mount St. Helens, Washington, *Water Resour. Res.*, 31, 7, 1797-1808.
- Magnuson, J. J., L. B. Crowder, and P. A. Medvick (1979), Temperature as an ecological resource, *Am. Zool.*, 19, 1, 331-343.
- Manga, M., and J. W. Kirchner (2000), Stress partitioning in streams by large woody debris, *Water Resour. Res.*, 36, 8, 2373-2379.
- Marion, A., A. I. Packman, M. Zaramella, and A. Bottacin-Busolin (2008), Hyporheic flows in stratified beds, *Water Resour. Res.*, 44, W09433, doi: 10.1029/2007wr006079.
- McClain, M. E., E. W. Boyer, C. L. Dent, S. E. Gergel, N. B. Grimm, P. M. Groffman, S. C. Hart, J. W. Harvey, C. A. Johnston, E. Mayorga, W. H. McDowell, and G. Pinay (2003), Biogeochemical hot spots and hot moments at the interface of terrestrial and aquatic ecosystems, *Ecosystems*, 6, 4, doi: 10.1007/s10021-003-0161-9.
- Montgomery, D. R., T. B. Abbe, J. M. Buffington, N. P. Peterson, K. M. Schmidt, and J. D. Stock (1996), Distribution of bedrock and alluvial channels in forested mountain drainage basins, *Nature*, 381, 587-589.
- Montgomery, D. R., J. M. Buffington, R. D. Smith, K. M. Schmidt, and G. Pess (1995), Pool spacing in forest channels, *Water Resour. Res.*, 31, 4, 1097-1105.
- Montgomery, D. R., and H. Piégay (2003), Wood in rivers: interactions with channel morphology and processes, *Geomorphology*, 51, 1-3, 1-5.

- Mutz, M., E. Kalbus, and S. Meinecke (2007), Effect of instream wood on vertical water flux in low-energy sand bed flume experiments, *Water Resour. Res.*, *43*, W10424, doi: 10.1029/2006WR005676.
- Nilsson, C., and K. Berggren (2000), Alterations of riparian ecosystems caused by river regulation, *Bioscience*, *50*, 9, 783-792.
- Nilsson, C., C. A. Reidy, M. Dynesius, and C. Revenga (2005), Fragmentation and flow regulation of the world's largest river systems, *Science*, *308*, 5720, doi: 10.1126/science.1107887.
- O'Connor, B. L., and J. W. Harvey (2008), Scaling hyporheic exchange and its influence on biogeochemical reactions in aquatic ecosystems, *Water Resour. Res.*, *44*, W12423, doi: 10.1029/2008wr007160.
- O'Connor, B. L., M. Hondzo, and J. W. Harvey (2010), Predictive modeling of transient storage and nutrient uptake: Implications for stream restoration, *J. Hydraul. Eng.-ASCE*, *136*, 12, doi: 10.1061/(asce)hy.1943-7900.0000180.
- Peterson, E. W., and T. B. Sickbert (2006), Stream water bypass through a meander neck, laterally extending the hyporheic zone, *Hydrogeol. J.*, *14*, 8, 1443-1451.
- Poole, G. C., and C. H. Berman (2001), An ecological perspective on in-stream temperature: Natural heat dynamics and mechanisms of human-caused thermal degradation, *Environmental Management*, *27*, 6, 787-802.
- Ranga Raju, K. F., O. P. S. Rana, G. L. Asawa, and A. S. N. Pillai (1983), Rational assessment of blockage effect in channel flow past smooth circular cylinders, *Journal of Hydraulic Research*, *21*, 289-302.
- Ren, J., and A. I. Packman (2004), Stream-subsurface exchange of zinc in the presence of silica and kaolinite colloids, *Environ. Sci. Technol.*, *38*, 24, doi: 10.1021/es035090x.
- Renard, P., and G. de Marsily (1997), Calculating equivalent permeability: a review, *Advances in Water Resources*, *50*, 5-6, 253-278.
- Ritzi, R. W., Z. Dai, D. F. Dominic, and Y. N. Rubin (2004), Spatial correlation of permeability in cross-stratified sediment with hierarchical architecture, *Water Resour. Res.*, *40*, doi: 10.1029/2003WR002420.
- Roni, P., and T. P. Quinn (2001), Density and size of juvenile salmonids in response to placement of large woody debris in western Oregon and Washington streams, *Can. J. Fish. Aquat. Sci.*, *58*, 282-292.

- Rowe, P. P. (1960), An equation for estimating transmissibility and coefficient of storage from river-level fluctuations, *Journal of Geophysical Research*, 65, 10, 3419-3424.
- Runkel, R. L. (1998), One-dimensional transport with inflow and storage (OTIS): a solute transport model for streams and rivers, *US Geological Survey Water Resources Investigations Report*, 98-4018.
- Salehin, M., A. I. Packman, and M. Paradis (2004), Hyporheic exchange with heterogeneous streambeds: Laboratory experiments and modeling, *Water Resour. Res.*, 40, W11504, doi: 10.1029/2003WR002567.
- Sawyer, A. H., M. B. Cardenas, and J. Buttles (in review), River-groundwater exchange due to large woody debris, *Water Resour. Res.*
- Scealy, J. A., S. J. Mika, and A. J. Boulton (2007), Aquatic macroinvertebrate communities on wood in an Australian lowland river: experimental assessment of the interactions of habitat, substrate complexity and retained organic matter, *Mar. Freshw. Res.*, 58, 2, doi: 10.1071/mf06105.
- Scheibe, T. D., and D. L. Freyberg (1995), Use of sedimentological information for geometric simulation of natural porous media structure, *Water Resour. Res.*, 31, 12, 3259-3270.
- Schmidley, E. B. (1987), The sedimentology, paleogeography and tectonic setting of the Pennsylvanian Massillon Sandstone in East-Central Ohio, Univ. of Akron, Akron, Ohio.
- Shields, F. D., and C. J. Gippel (1995), Prediction of effects of woody debris removal on flow resistance, *Journal of Hydraulic Engineering*, 121, 4, 341-354.
- Shields, F. D., S. S. Knight, and J. M. Stofleth (2006), Large wood addition for aquatic habitat rehabilitation in an incised, sand-bed stream, Little Topashaw Creek, Mississippi, *River Research and Applications*, 22, 7, 803-817.
- Singh, S. K. (2004), Aquifer response to sinusoidal or arbitrary stage of semipervious stream, *Journal of Hydraulic Engineering*, 130, 11, doi: 10.1061/(ASCE)0733-9429(2004)130:11(1108).
- Smock, L. A., G. M. Metzler, and J. E. Gladden (1989), Role of debris dams in the structure and functioning of low-gradient headwater streams, *Ecology*, 70, 3, 764-775.
- Srivastava, R. (2006), Aquifer diffusivity estimation from response to stream stage variation, *Journal of Hydrologic Engineering*, 11, 3, doi: 10.1061/(ASCE)1084-0699(2006)11:3(273).

- Stanford, J. A., and J. V. Ward (1988), The hyporheic habitat of river ecosystems, *Nature*, 335, 64-66.
- Stanford, J. A., and J. V. Ward (1993), An ecosystem perspective of alluvial rivers - Connectivity and the hyporheic corridor, *J. N. Am. Benthol. Soc.*, 12, 1, 48-60.
- Storey, R. G., K. W. F. Howard, and D. D. Williams (2003), Factors controlling riffle-scale hyporheic exchange flows and their seasonal changes in a gaining stream: A three-dimensional groundwater flow model, *Water Resour. Res.*, 39, 2, doi: 10.1029/2002WR001367.
- Swamee, P. K., and S. K. Singh (2003), Estimation of aquifer diffusivity from stream stage variation, *Journal of Hydrologic Engineering*, 8, 1, doi: 10.1061/(ASCE)1084-0699(2003)8:1(20).
- Swanson, T. E., and M. B. Cardenas (2010), Diel heat and transport within the hyporheic zone of a pool-riffle-pool sequence of a losing stream and evaluation of models for fluid flux estimation using heat, *Limnology and Oceanography*, 55, 4, doi: 10.4319/lo.2010.55.4.1741.
- Thibodeaux, L. J., and J. D. Boyle (1987), Bedform-generated convective transport in bottom sediment, *Nature*, 325, 341-343.
- Tidwell, V. C., and J. L. Wilson (2000), Heterogeneity, permeability patterns, and permeability upscaling: Physical characterization of a block of Massillon Sandstone exhibiting nested scales of heterogeneity, *SPE Reservoir Evaluation and Engineering*, 3, 4, 283-291.
- Tidwell, V. C., and J. L. Wilson (2002), Visual attributes of a rock and their relationship to permeability: A comparison of digital image and minipermeameter data, *Water Resour. Res.*, 38, 11, doi: 10.1029/2001WR000932.
- Tóth, J. A. (1963), A theoretical analysis of ground-water flow in small drainage basins, *Journal of Geophysical Research*, 68, 16, 4795-4811.
- Triska, F. J., V. C. Kennedy, R. J. Avanzio, G. W. Zellweger, and K. E. Bencala (1989), Retention and transport of nutrients in a third-order stream in northwestern California: Hyporheic processes, *Ecology*, 70, 1893-1905.
- Vaux, W. G. (1968), Intragravel flow and interchange of water in a streambed, *Fishery Bulletin*, 66, 479-489.
- Wagner, F. H., and G. Bretschko (2002), Interstitial flow through preferential flow paths in the hyporheic zone of the Oberer Seebach, Austria, *Aquatic Sciences*, 64, 3, 307-316.

- Wallace, J. B., S.L. Eggert, J.L. Meyer, J.R. Webster (1997), Multiple trophic levels of a forest stream linked to terrestrial litter inputs, *Science*, 277, 5322, 102-104.
- Wallace, J. B., J. R. Webster, and J. L. Meyer (1995), Influence of log additions on physical and biotic characteristics of a mountain stream, *Can. J. Fish. Aquat. Sci.*, 52, 2120-2137.
- Ward, J. V., and J. A. Stanford (1995), The serial discontinuity concept: extending the model to floodplain rivers, *Regulated Rivers: Research and Management*, 10, 159-168.
- Weber, K. J. (1982), Influence of common sedimentary structures on fluid flow in reservoir models, *Journal of Petroleum Technology*, 34, 665-672.
- Webster, J. R., J.L. Tank, J.B. Wallace, J.L. Meyer, S.L. Eggert, T.P. Ehrman, B.R. Ward, B.L. Bennett, P.F. Wagner, M.E. McTammany (2000), Effects of litter exclusion and wood removal on phosphorus and nitrogen retention in a forest stream, *Verh. Internat. Verein. Limnol.*, 27, 1337-1340.
- Webster, J. R., and J. L. Meyer (1997), Organic matter budgets for streams: A synthesis, *J. N. Am. Benthol. Soc.*, 16, 1, 141-161.
- Wilcox, A. C., J.M. Nelson, E.E. Wohl (2006), Flow resistance dynamics in step-pool channels: 2. Partitioning between grain, spill, and woody debris resistance, *Water Resour. Res.*, 42, W05419, doi: 10.1029/2005WR004278.
- Wilcox, A. C., and E. E. Wohl (2006), Flow resistance dynamics in step-pool stream channels: 1. Large woody debris and controls on total resistance, *Water Resour. Res.*, 42, W05418, doi: 10.1029/2005WR004277.
- Wilcox, D. C. (1998), *Turbulence modeling for CFD*, DCW Industries, Inc., La Canada, California.
- Winter, T. C. (1999), Relation of streams, lakes, and wetlands to groundwater flow systems, *Hydrogeol. J.*, 7, 28-45.
- Winter, T. C., J. W. Harvey, O. L. Franke, and W. A. Alley (1998), Groundwater and surface water: A single resource, *U.S. Geological Survey Circular*, 1139, 1-79.
- Woessner, W. W. (2000), Stream and fluvial plain ground water interactions: Rescaling hydrogeologic thought, *Ground Water*, 38, 3, 423-429.
- Wondzell, S. M. (2006), Effect of morphology and discharge on hyporheic exchange flows in two small streams in the Cascade Mountains of Oregon, USA, *Hydrol. Process.*, 20, 2, doi: 10.1002/hyp.5902.

- Wondzell, S. M., J. LaNier, R. Haggerty, R. D. Woodsmith, and R. T. Edwards (2009), Changes in hyporheic exchange flow following experimental wood removal in a small, low-gradient stream, *Water Resour. Res.*, 45, W05406, doi: 10.1029/2008WR007214.
- Wondzell, S. M., and F. J. Swanson (1996), Seasonal and storm dynamics of the hyporheic zone of a 4th-order mountain stream. I: Hydrologic processes, *J. N. Am. Benthol. Soc.*, 15, 3-19.
- Worman, A., A. I. Packman, L. Marklund, J. W. Harvey, and S. H. Stone (2006), Exact three-dimensional spectral solution to surface-groundwater interactions with arbitrary surface topography, *Geophys. Res. Lett.*, 33, L07402, doi: 10.1029/2006GL025747.
- Wright, J. P., and A. S. Flecker (2004), Deforesting the riverscape: the effects of wood on fish diversity in a Venezuelan piedmont stream, *Biological Conservation*, 120, 3, 439-447.
- Zarnetske, J., R. Haggerty, S. Wondzell, and M. Baker (in press), *Journal of Geophysical Research-Biogeosciences*.
- Zlotnik, V. A., M. B. Cardenas, and D. Toundykov (2011), Effects of multiscale anisotropy on basin and hyporheic groundwater flow, *Ground Water*, doi: 10.1111/j.1745-6584.2010.00775.x.